Keisuke Murata

Crystallization Processes of Circumstellar Silicate Dust

A dissertation for the degree of Doctor of Philosophy

Department of Earth and Space Science

Graduate School of Science

Osaka University

1-1 Machikaneyama, Toyonaka, Osaka, JAPAN.

February, 2009

Abstract

Observations with the Infrared Space Observatory (ISO, 1995-1998) have revealed that silicate dust is partially crystallized in circumstellar environments of young and evolved stars, and allowed us to discuss detailed dust mineralogy and processing. Mineralogical information from astronomical observations reflects physical and chemical conditions of formation and processing of circumstellar dust. Since then, a new scientific field called "astromineralogy" has been opened. This thesis is related to this young scientific field. In this thesis, we focus on crystallization process of amorphous silicate materials in circumstellar environments, since the crystallization is a fundamental process in formation of the important and major component of dust: crystalline silicates. The crystallization reflects physical and chemical conditions, especially at high temperature around 1000 K, where dust particles have been formed and processed. Using amorphous silicate materials synthesized by a sol-gel method, we carried out laboratory simulations of crystallization process in circumstellar environments of young and evolved stars.

This thesis composes of four parts (chapter 2-5). In chapter 2, we evaluated quantitatively the time constant of enstatite crystallization in the Johnson-Mehl-Avrami equation, and determined the activation energy of crystallization. The result suggests that enstatite can be crystallized only

in the inner disk region around young stars and in the vicinity of the condensation zone around evolved stars. In stellar winds of evolved stars, the final degree of crystallization of silicate dust has very large dependence on the condensation temperatures.

A detailed IR spectroscopy of enstatite sample produced in chapter 2 was carried in chapter 3. There was a discrepancy between the IR feature of enstatite obtained in this experiment and that obtained in the previously reported experiments using the single crystals, due to stacking faults. We discovered that astronomical observed dust emission of enstatite is similar to the IR feature measured in this experiment.

In chapter 4, crystallization kinetics of olivine from an Fe-bearing amorphous silicate was discussed. We suggested that crystallization processes in circumstellar regions should depend on the properties of amorphous silicates, such as the existence of crystallites and/or the Fe content.

We also showed in chapter 5 the first experimental evidence that Fe-depleted olivine can be formed by crystallization processes via thermal heating of FeO-bearing amorphous silicates. In the past, there has been an inconsistency in compositions between coexisting crystalline and amorphous phases. Our discovery that the crystallization process is involved in Mg/Fe fractionation can answer the composition paradox of the coexistence of Mg-rich crystalline silicates and Fe-bearing amorphous silicates around stars.

Acknowledgment

I am very grateful to many people who have contributed directly and indirectly to this thesis.

I would like to thank my supervisor, Professor Dr. Akira Tsuchiyama, for always giving me advices and opportunity to make this kind of study. His great knowledge on mineralogy and critical comments always improved my study. I would like to acknowledge Dr. Hiroki Chihara, for leading me to this field of science and giving me instructive advices and constant supports. Without His help and blessings, I believed that I could not finish this thesis perfectly. I would also like to thank Professor Dr. Chiyoe Koike who taught me infrared spectroscopy of solid materials and provided fruitful suggestions. I am grateful to Mr. Takashi Takakura and Mr. Yuta Imai, for providing a lot of useful advices. I was very happy to work with them.

I would like to acknowledge Dr. Tomoki Nakamura and his collaborators, especially Dr. Takeshi Akaki, Ms. Kanako Sakamoto, Mr. Tatsunori Yokoyama, and Dr. Yukio Yamamoto, for the X-ray diffraction experiments at synchrotron radiation facilities. I would also like to acknowledge Dr. Takaaki Noguchi, for the transmission electron microscopy experiments. I would like to thank Dr. Norimasa Shimobayashi, for the sol-gel synthesis. I would like to acknowledge Dr. Frank Molster, for providing me his observational data.

I would express my special gratitude to Dr. Atsushi Tani who provided guidance and support of so many things I cannot possibly list them all here during the six years of my graduated and undergraduate studies at Osaka University.

I have to thank everyone in Tsuchiyama laboratory and Ikeya laboratory at Osaka University. Special scientific and non-scientific thanks go to Dr. Hiroshi Arima, and Dr. Toshihiro Somekawa. I was financially supported by the Japan Society for the Promotion of Science.

I thank my parents and my brother. They always supported me and encouraged me.

Finally, I would like to acknowledge the late Professor Emeritus Dr. Motoji Ikeya, who introduced me to scientific research when I was undergraduate. Without him, my graduate study would not have been started.

Contents

Chapter 1

General Introduction

1.1 Dust - A Ubiquitous Material in Space

Interstellar space is not empty, but filled with gas and solid particles of submicron scale, referred to as dust. Dust is only about 1% of the mass of the interstellar medium (ISM). However, much attention has been paid to the optical property of dust particles. When one looks at the clear night sky, for example, one can see dark patches in the bright band of the Milky Way. This is due to the combined effects of interstellar absorption and scattering of light by dust particles (referred to as interstellar extinction).

Dust is a ubiquitous material in space (Fig. 1.1), and dominates the energy balance through absorption and emission of radiation. The study of dust particles in astronomical environments is a major important field not only in astronomy and astrophysics as significant constituents of the Universe, but also in physics and chemistry for understanding their fundamental properties. They are necessary to form molecular ices on their surfaces in cold and dense molecular cloud. They can drive the mass loss of a star that is approaching the end of its life. Furthermore, they are starting materials

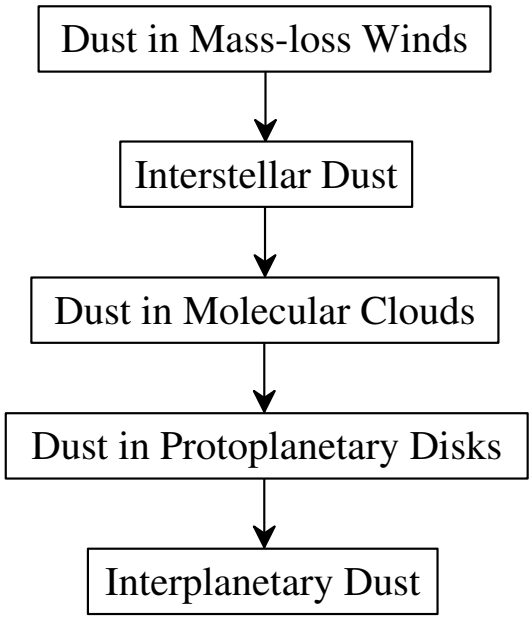

Figure 1.1: An evolutionary sequence of cosmic dust.

to form planet(esimal)s around young stars like the Sun.

1.2 Astromineralogy

Observations with the Short Wavelength Spectrometer (SWS) and the Long Wavelength Spectrometer (LWS) on board of the Infrared Space Observatory (ISO, 1995-1998) have provided high quality astronomical data over wide wavelength range (2.4 - 200 μm) with a high resolution, and allowed us to discuss detailed dust mineralogy and processing. Before the ISO was launched, it was generally supposed that, although the crystalline lattice structure is energetically the most favorable state for silicates, cosmic dust silicates have amorphous structure. However, the ISO has revealed that silicate dust is partially crystallized as olivine $[(\mathrm{Mg,Fe})_2\mathrm{SiO}_4]$ and pyroxene $[(\mathrm{Mg,Fe})\mathrm{SiO}_3]$ in circumstellar environments around oxygen-rich young and

evolved stars and comets (e.g., Waelkens et al., 1996; Waters et al., 1996; Crovisier et al., 1997). Mineralogical information from the astronomical observations reflects physical and chemical conditions of formation and processing of circumstellar dust. Since then, a new scientific field called "astromineralogy" has been opened (e.g., Henning, 2003).

1.2.1 Dust Formation in Evolved Stars

Most dust forms in the outflowing gas from mass-losing evolved stars, or in supernovae. Estimation of mass-loss rates for dust sources suggests that more than 85% of interstellar dust is expected to come from evolved stars (Whittet, 2003). However, since there is still little information about the dust production rate in supernovae, the estimation contains considerable uncertainty. Our knowledge of dust production is also based on the analyses of "presolar grains", which are found in primitive meteorites or interplanetary dust particles. The stellar origin of the grains is indicated by enormous isotopic ratio variations compared with Solar System materials, explainable only by nuclear reactions occurring in stars. Most of the grains are expected to be formed in stellar winds from evolved stars (Nittler et al., 1997; Alexander, 1997; Morgan & Edmunds, 2003). Overall, it is true that evolved stars are the dominant sources of dust formation.

Stars whose main-sequence mass is low-to-intermediate (0.8 - 8 $M_{\odot}$) are believed to evolve at the end of their life into a phase known as the Asymptotic Giant Branch (AGB). AGB stars have low effective temperatures ($\lesssim$ 3000 K) and high luminosity ($\gtrsim$ 3000 $L_{\odot}$). An AGB star is known to lose a significant fraction of their mass through slow, massive winds. In stellar outflows of oxygen-rich AGB stars, silicate dust condensation starts in the circumstellar envelope. The high mass stars evolve into a red supergiant

phase with a stellar wind with properties similar to those of the AGB stars.

The basic scenario for this mass-loss process is that of pulsation-enhanced dust-driven winds. Shock waves created by stellar pulsation lead to a cool and extended stellar atmosphere. Efficient dust formation is allowed under this condition. The grains absorb light from the central star and are accelerated away from the star by radiation pressure. They also drag gas along together. The dust-driven stellar wind scenario provides a realistic framework for understanding mass loss from carbon-rich AGB stars (e.g., Höfner, 2003). However, recent detailed models demonstrate that radiation pressure on silicate grains is not sufficient to drive the observed mass-loss winds of oxygen-rich AGB stars, contrary to previous expectations (Woitke, 2006). The complex physics of a dust-driven wind and the dust-formation process around oxygen-rich AGB stars is still an unsolved puzzle.

The dust particles around an AGB star absorb light from the central star and re-emit this light in the infrared (IR) region. There are many vibrational modes of solid matters in the IR regions. Therefore, detection of the IR emission can allow us for detailed investigation of dust properties around stars (Fig. 1.2). The most abundant dust species in the stellar winds of oxygen-rich stars are amorphous silicates. In addition to those, about 5% of silicate dust is in crystalline form (Tielens et al., 1998). Olivine and pyroxene are the major crystalline phases. Molster et al. (2002) suggested that enstatite is more abundant than forsterite by a factor of 3-4.

Silicate condensation in stellar winds may start at a temperature of about 1000 K (e.g., Gail & Sedlmayr, 1999; Sogawa & Kozasa, 1999). Silicates should be amorphous at the initial stage of condensation because of much shorter cooling timescale (e.g., Seki & Hasegawa, 1981; Gail & Sedlmayr, 1999; Rietmeijer et al., 1999) and the existence of a lot of amorphous silicates.

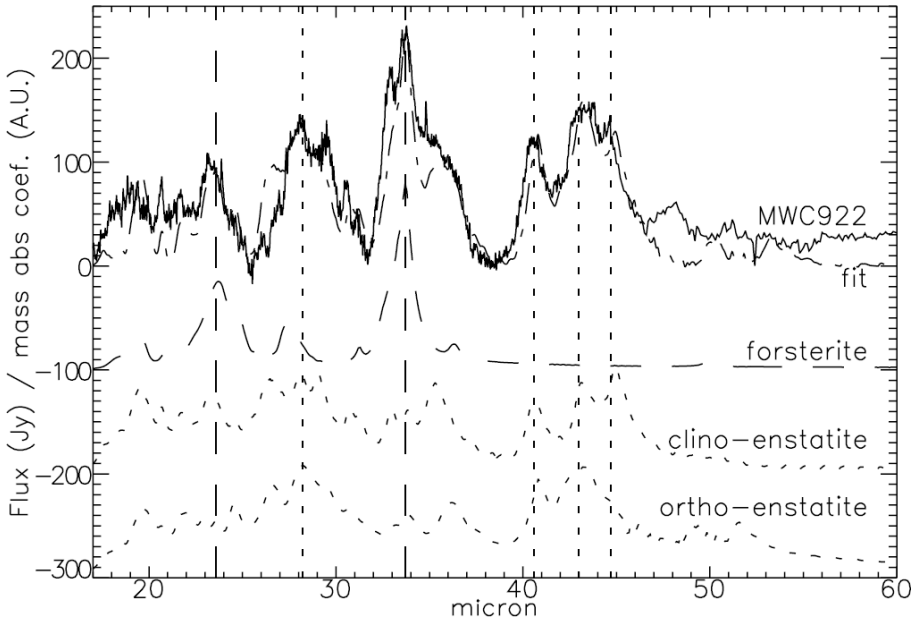

Figure 1.2: The continuum subtracted spectrum of an evolved star (MWC922; solid line), compared with the laboratory spectrum of forsterite (at 90 K; dashed line), and clino and ortho-enstatite (at 100 K; dotted line). The fit is shown as the dashed-dotted line. The vertical lines denote the diagnostic features of forsterite (dashed lines) and enstatite (dotted lines). Figure taken from Molster & Kemper (2005).

During the annealing process of a temperature decrease, amorphous silicate dust can crystallize to olivine and pyroxene. The chemical composition of the crystalline silicates could be constrained to be very Mg-rich and Fe-poor (Mg# = atomic Mg/(Mg+Fe) ratio > 0.9 (Tielens et al., 1998)), while amorphous ones contain Fe (Mg# ~ 0.5 (e.g., Molster et al., 1999; Kemper et al., 2004; van Boekel et al., 2005)).

After the formation and annealing, the dust particles are injected away towards space of lower density and temperature. Thus, if we consider that AGB stars are expected as the main contributors of dust to the ISM, the

crystalline silicate dust formed in these stars should be observed in the ISM. On the contrary, analysis of observed spectra indicated that the interstellar silicates are sub-micron sized amorphous particles. Only very small amounts of crystalline silicates are present in the ISM (an upper limit of crystalline fraction of 5% by Li & Drain (2001); 2.2% by Kemper et al. (2004, 2005)). The lack of crystalline silicates makes it plausible that amorphization occurs in the ISM. Various mechanisms are suggested (e.g., ion bombardments or interstellar dust dilution), but are still under discussion.

1.2.2 Dust Processing in Young Stars

Some of the interstellar dust is incorporated into circumstellar disks around newly formed stars and move slowly inwards, where they initiate the growth of larger dust grains into planetesimals and eventually planets. Spectroscopic observations of IR emission toward intermediate-mass (2 - 8 $M_{\odot}$) and low-mass (< 2 $M_{\odot}$) pre-main-sequence stars (e.g., Waelkens et al., 1996; van Boekel et al., 2005; Honda et al., 2006) show that silicate dust that prevails in circumstellar environments is partially crystalline, such as olivine and pyroxene (Fig. 1.3). The crystalline silicates have highly Mg-rich and Fe-poor compositions, as well as those in the stellar winds of evolved stars. As mentioned above, the interstellar silicates are almost completely amorphous. Thus, the crystalline silicates found around young stars are formed in situ. When stellar radiation makes the dust temperature high enough to be converted from a disordered structure into an ordered one, crystallization processes can start. Shock wave heating is also proposed as the heating mechanism of silicate dust (Harker & Desch, 2002).

Another possible source of circumstellar crystalline silicates is the direct condensation from the gas phase. This takes place near the central star

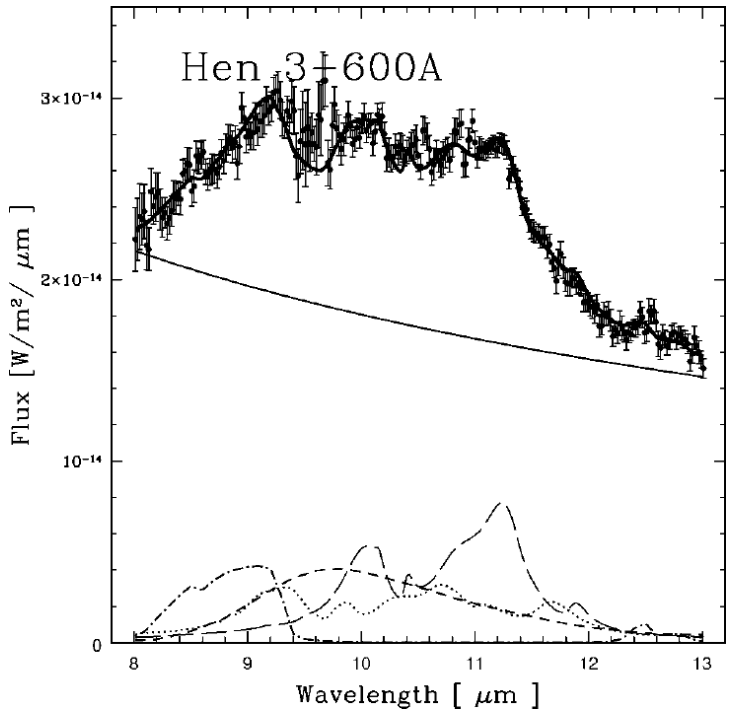

Figure 1.3: The spectrum of a T Tauri star Hen 3-600A. The thick solid line is the best-fit model spectrum, which is the sum of power-law continuum (thin solid line), glassy olivine (dashed line), orthoenstatite (dotted line), forsterite (long-dashed line), and silica (dot-dashed line). Figure taken from Honda et al. (2003).

when the gas cools down. Since the mass of material located within the sublimation region of the disk is much small (e.g., Hersant et al., 2001), the thermal heating process of dust is supposed to play more important role for formation of crystalline silicates. Therefore, we discuss only the thermal heating crystallization process in this thesis, with the remainder from the direct condensation processes. Experimental studies of gas-to-solid condensation have also been made (e.g., Tsuchiyama, 1998; Toppani et al., 2006).

1.3 Crystallization of Circumstellar Silicate by Thermal Heating

Laboratory experiments using cosmic dust analogues are an important tool to test the proposed physical-chemical processes for understanding of the dusty Universe. The ISO discovery of the crystalline silicates triggered many laboratory studies on silicate formation and processing. In this thesis, we focused on crystallization experiments of synthesized amorphous silicate materials, since the crystallization is a fundamental process in formation of the important and major component of dust: crystalline silicates. The crystallization reflects physical and chemical conditions, especially at high temperature around 1000 K, where dust particles have been formed and processed.

In an astronomical context, amorphous silicates, as cosmic dust analogues and starting materials of crystallization, were synthesized in laboratories by various methods, including quenching of melt, vapor condensation, and a sol-gel method (e.g., Dorschner et al., 1995; Hallenbeck et al., 1998; Fabian et al., 2000; Scott & Duley, 1996; Jäger et al., 2003). Using the melt-quenching method, it is difficult to synthesize completely amorphous materials with MgO- and FeO-rich and SiO_2-poor compositions, such as olivine and pyroxene ones. The vapor condensation method has the advantage of synthesizing amorphous condensates under conditions similar to astrophysical ones. However, control of the chemical composition and a verification of the experimental parameters are very difficult. The sol-gel method has an advantage of synthesizing a low-density amorphous silicate with well-controlled chemical compositions at relatively lower temperature without evaporation of volatile elements, such as sodium. However, the formation of amorphous silicates in

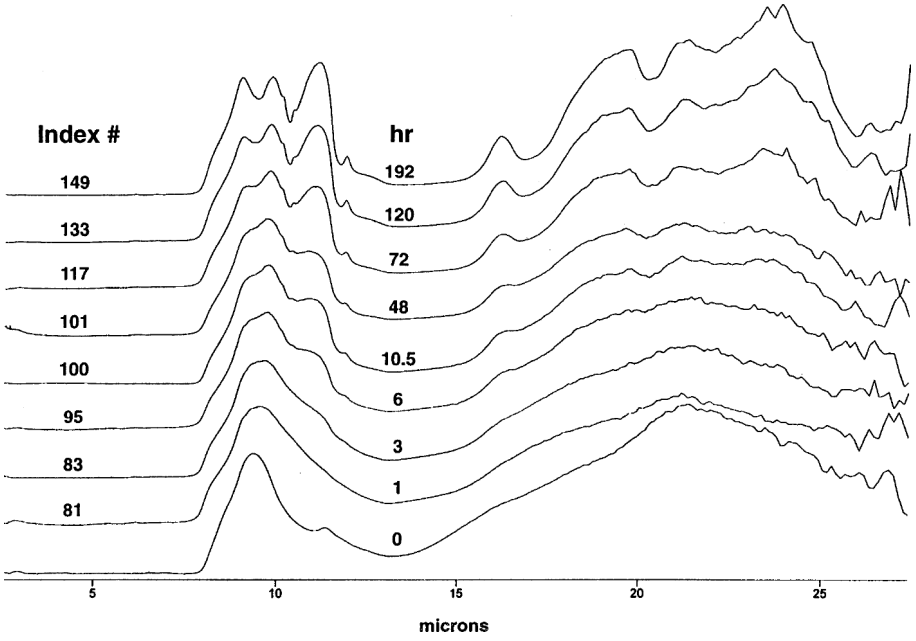

Figure 1.4: IR spectral evolution by annealing of magnesium silicate smoke in vacuum at 1027 K. Forsterite and tridymite were crystallized (sharp features) from amorphous silicate (broad feature at around 10 and 20 μm, that are attributed, respectively, to Si-O stretching and O-Si-O vending vibrational mode). Figure taken from Hallenbeck et al. (1998).

astrophysical environments is far from the wet chemical processing. In any case, the synthesizing methods have both advantage and disadvantage. It is appropriate to choose the best one depending on purposes of the laboratory experiments.

Using amorphous magnesium silicate smokes prepared by vapor phase condensation, some heating experiments have been carried out (Hallenbeck et al., 1998; Brucato et al., 1999; Fabian et al., 2000). Hallenbeck et al. (1998) heated the smokes in vacuum at temperatures between 1000 and 1048 K (Fig. 1.4). Forsterite (Mg_2SiO_4) and tridymite (SiO_2) were crystallized by thermal heating of the smoke. They observed a "stall" phase during the

evolution of the IR spectra, in which the spectra remained almost unaltered. However, it remained unclear why this stall phase occurred. Rietmeijer et al. (2002) examined the starting smoke by transmission electron microscopy and found that it included amorphous silicates, forsterite, tridymite, and periclase (MgO).

Using magnesium silicate glass with the enstatite ($MgSiO_3$) composition, Fabian et al. (2000) reported the IR spectral evolution through the crystallization process of the glass. Orthoenstatite was crystallized from the enstatite glass. They evaluated activation energy of the enstatite crystallization. However, the value was estimated without doing "the Arrhenius plot" (details are given in chapter 2).

Using a sol-gel method, Jäger et al. (2003) synthesized amorphous Mg silicates with different Mg/Si ratios, and observed crystallization of forsterite and enstatite by IR measurements. Thompson et al. (2002) also synthesized amorphous silicates with enstatite composition by a sol-gel method and performed crystallization experiments. Crystallization of forsterite was observed using a synchrotron radiation X-ray diffraction method. They suggested that their starting amorphous sample was partially crystallized to forsterite.

1.4 Aim and Outline of This Thesis

The aim of this thesis is to understand the amorphous to crystalline transformation of silicate dust in circumstellar regions. There are several laboratory experiments that revealed interesting crystallization behaviors of amorphous silicates. However, two major problems remain in the previous experimental studies;

- Magnesium iron silicates have not been used in most all of the previous

crystallization experiments. However, iron is the major dust-forming element as well as magnesium and silicon, concerning the solar abundance of elements (Anders & Grevesse, 1989). In general, iron is believed to form metal, sulfides, ferric, and/or ferrous silicates or oxides.

- Degree of crystallization (the crystalline/amorphous ratio) of the heated samples has not been measured quantitatively. Information about the degree of crystallization as a function of time and temperature is critical to discussing crystallization kinetics and timescale.

In this thesis, we used synthesized amorphous magnesium iron silicates as well as an Fe-free magnesium silicate. We assumed the solar abundance of elements as the standard composition of solid material. The three cases were examined (Fig. 1.5, Table 1.1);

(1) All of the iron forms metal and/or sulfide, and is not contained in the silicates and oxides (FeO-free).

(2) All of the iron is divalent cation, forming amorphous silicates (the most FeO-rich).

(3) All sulfur formed iron sulfide grains and an Fe content of the amorphous silicate was reduced by the solar composition of sulfur as FeS.

We performed thermal heating experiments with the synthesized amorphous cosmic dust analogues. Since we needed FeO-bearing and SiO_2-poor amorphous silicates, a sol-gel method was adopted. The degree of the crystallization was estimated quantitatively by fitting of the IR spectroscopic evolutions. Using those, we discussed kinetics and timescales of the crystallization process. A behavior of ferric iron in silicates during crystallization processes was also discussed.

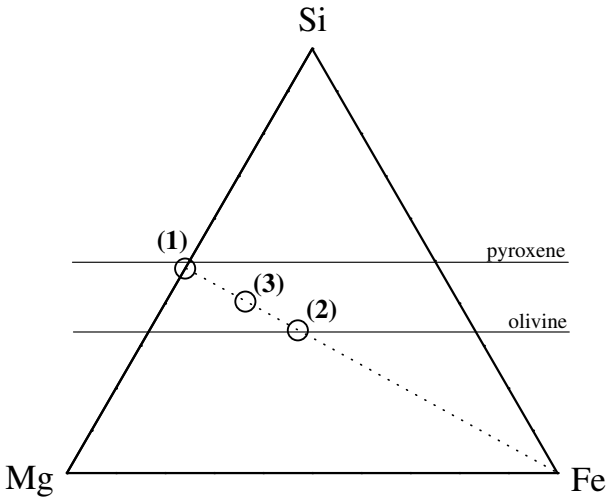

Figure 1.5: Ternary diagram of atomic proportions of starting materials of crystallization experiments in this thesis.

The structure of this thesis is following. An introduction of dust formation and processing under astrophysical conditions is given in chapter 1. The study of the crystallization experiment of an amorphous Mg silicate with the Mg/Si ratio of 1.07 (case (1)) is given in chapters 2 and 3. The activation energy of enstatite crystallization was obtained. The result indicates kinetic inhibition of the crystallization in cold circumstellar regions (chapter 2). The IR spectroscopic similarity between the heated silicate in this experiments and circumstellar dust emission is discovered (chapter 3). Chapter 2 is based on the paper by Murata et al. (2009a). In chapter 4, we show that crystallization processes in circumstellar regions should depend on the properties of amorphous silicates, such as the existence of crystallites and/or the Fe content, from the experiment of the most FeO-rich amorphous silicate (case (2)). It is based on the referred article (Murata et al., 2007). In chapter 5, using a FeO-bearing amorphous silicate (case (3)), compositional change

Table 1.1: Atomic proportions of starting materials of crystallization experiments in this thesis.

	Mg	Si	Fe	Al	Ca	Na	Ni	S
solar abundance	1.07	1	0.90	0.085	0.061	0.057	0.049	0.52
case (1) (chapter 2, 3)	1.07	1	-	-	-	-	-	-
case (2) (chapter 4)	1.07	1	0.90	0.085	0.061	0.057	0.049	-
case (3) (chapter 5)	1.07	1	0.39	-	-	-	-	-

of crystallized silicate during the crystallization process is investigated. Our discovery that Mg/Fe fractionation is involved in the crystallization process can resolve a paradox of the differing compositions of silicate dust, namely the coexistence of Mg-rich crystalline silicates and Fe-bearing amorphous silicates around stars. Chapter 5 is based on the paper by Murata et al. (2009b). Last chapter summarizes the obtained results and presents the prospects of this field for future study.

Bibliography

Alexander, C. M. O'D. 1997, in Astrophysical implications of the laboratory study of pre-solar materials, ed. Bernatowicz, T. J. & Zinner, E. K. (AIP Conference Proceedings 402), 567

Anders, E., & Grevesse, N. 1989, Geochim. Cosmochim. Acta, 53, 197

Brucato, J. R., Colangeli, L., Mennella, V., Palumbo, P., & Bussoletti, E. 1999, A&A, 348, 1012

Crovisier, J. et al. 1997, Science 275, 1904

Dorschner, J., Begemann, B., Henning, Th., Jäger, C., & Mutschke, H. 1995, A&A, 300, 503

Fabian, D., Jäger, C., Henning, Th., Dorschner, J., & Mutschke, H. 2000, A&A, 364, 282

Gail, H.-P. & Sedlmayr, E. 1999, A&A, 347, 594

Hallenbeck, S. L., Nuth III, A. J., & Daukantas, P. L. 1998, Icarus, 131, 198

Harker, D. E. & Desch, S. J. 2002, ApJ, 565, L109

Hersant, F., Gautier, D., & Huré, J.-M. 2001, ApJ, 554, 391

Henning, Th. 2003, Astromineralogy, ed. (Lecture Notes in Physics 609; New York: Springer)

Höfner, S., Gautschy-Loidl, R., Aringer, B., & Jorgensen, U. G. 2003, A&A, 399, 589

Honda, M., Kataza, H., Okamoto, Y. K., et al. 2003, ApJ, 585, L59

Honda, M., et al. 2006, ApJ, 646, 1024

Jäger, C., Dorschner, J., Mutschke, H., Posch, Th., & Henning, Th. 2003, A&A, 408, 193

Kemper, F., Vriend, W. J., & Tielens, A. G. G. M. 2004, ApJ, 609, 826

Kemper, F., Vriend, W. J., & Tielens, A. G. G. M. 2005, ApJ, 633, 534

Li, A., & Draine, B. T. 2001, ApJ, 550, L213

Malfait, K., Waelkens, C., Waters, L. B. F. M., et al. 1998, A&A, 332, L25

Molster, F. J. et al. 1999, A&A, 350, 163

Molster, F. J., Waters, L. B. F. M., Tielens, A. G. G. M., Koike, C., & Chihara, H. 2002, A&A 382, 241

Molster, F. J., & Kemper, C. 2005, Space Sci. Rev., 119, 3

Morgan, H. L., & Edmunds, M. G. 2003, MNRAS, 343, 427

Murata, K., Chihara, H., Tsuchiyama, A., Koike, C., Takakura, T., Noguchi, T., & Nakamura, T. 2007, ApJ, 668, 285

Murata, K., Chihara, H., Koike, C., Takakura, T., Imai, Y., & Tsuchiyama, A. 2009a, ApJ, 697, 836

Murata, K., Takakura, T., Chihara, H., Koike, C., & Tsuchiyama, A. 2009b, ApJ, 696, 1612

Nittler, L., Alexander, C. M. O'D., Gao, X., Walker, R. M., & Zinner, E. 1997, ApJ, 483, 475

Rietmeijer, F. J. M., Nuth III, J. A., & Karner, J. M. 1999, ApJ, 527, 395

Rietmeijer, F. J. M., Hallenbeck, S. L., Nuth III, J. A., & Karner, J. M. 2002, Icarus, 156, 269

Scott, A., & Duley, W. W. 1996, ApJS, 105, 401

Seki, J. & Hasegawa, H. 1981, Prog. Theor. Phys., 66, 903

Sogawa, H., & Kozasa, T. 1999, ApJ, 516, L33

Tielens, A. G. G. M., Waters, L. B. F. M., Molster, F. J. & Justtanont, K. 1998, Astrophys. Space Sci., 255, 415

Thompson, S. P., Fonti, S., Verrienti, C., et al. 2001, A&A, 368, 721

Toppani, A., Libourel, G., Robert, F., & Ghanbaja, J. 2006, Geochim. Cosmochim. Acta, 70, 5035

Tsuchiyama, A. 1998, Min. Jour., 20, 59

van Boekel, R. et al. 2005, A&A, 437, 189

Waelkens, C., Waters, L. B. F. M., de Graauw, M. S., et al. 1996, A&A, 315, L245

Waters, L. B. F. M., Molster, F. J., de Jong, T., et al. 1996, A&A, 315, L361

Whittet, D. C. B. 2003, Dust in the Galactic Environment (Graduate Series in Astronomy; Bristol: IOP)

Woitke, P. 2006, A&A 460, L9

Chapter 2

Activation Energy of Enstatite Crystallization

The activation energy of enstatite ($MgSiO_3$) crystallization was estimated at 1.12×10^5 K using an amorphous magnesium silicate with the Mg/Si ratio of 1.07 . This large value indicates kinetic inhibition of the crystallization in cold circumstellar regions. This chapter is a modified version of the paper as Murata et al., 2009, ApJ, 697, 836.

2.1 Introduction

Silicate dust is the main component of solid materials in astronomical environments. One of the major discoveries achieved with the IR spectroscopic observations of young and evolved stars is that silicate dust in circumstellar regions is partially crystallized (e.g., Waelkens et al., 1996; Waters et al., 1996). In contrast to circumstellar dust, it is believed that interstellar silicate dust is almost completely amorphous (Kemper et al., 2004). Therefore, interstellar amorphous silicates are considered to be precursor materials for crystalline silicates, such as olivine $[(\mathrm{Mg,Fe})_2\mathrm{SiO}_4]$ and pyroxene

[$(Mg, Fe)SiO_3$], both in circumstellar regions of young stars and in the solar nebula. Dust formed in stellar winds around evolved stars is also considered to undergo heating processes and be rearranged from amorphous into crystalline structures (e.g., Gail, 2002).

Some laboratory experiments have been carried out to investigate crystallization processes of circumstellar dust. These experiments in heating silicate dust analogues performed at temperature around 1000 K, because of limited timescales available in laboratory. However, we should pay attention to crystallization at temperature lower than in laboratory because much longer timescales of heating are allowed in astronomical environments. In order to extrapolate experimental results of crystallization conditions to lower temperature, we need a precise value of an activation energy of crystallization. In general, temperature dependence of a crystallization timescale, τ, can be written as the Arrhenius equation,

$$1/\tau = \nu_0 \exp(-E_c/k_B T), \tag{2.1}$$

where ν_0 is a frequency factor, E_c is the activation energy of crystallization, k_B is the Boltzmann constant, and T is the absolute temperature. We can estimate τ at lower temperature by extrapolating eq. 2.1 using ν_0 and E_c obtained by experiments. In the previous reports, crystallization experiments have been performed by heating amorphous Mg silicates, which have been synthesized by different methods, and the activation energy of crystallization was estimated (e.g., Brucato et al., 1999; Fabian et al., 2000). However, they estimated activation energy without doing "the Arrhenius plot" indirectly, by assuming the value of ν_0. Therefore, it has not been known whether these data are reliable for extrapolation or not (Gail, 2002).

In these previous experiments, the degree of crystallization (the crys-

talline/amorphous ratio) of the heated samples has not been measured quantitatively. It is difficult to determine characteristic crystallization time uniquely without quantitative determination of the degree of crystallization. Lately, a quantitative analysis method of crystallization processes has been developed by us, using fitting of IR spectra (Murata et al., 2007).

In this chapter, we synthesized an amorphous magnesium silicate sample in the MgO-SiO_2 system as a circumstellar dust analogue, and carried out crystallization experiments by heating the sample in the atmosphere. We obtained time constants of crystallization quantitatively at different temperatures by determining degree of crystallization, and estimated the activation energy of crystallization by the Arrhenius plot.

2.2 Experimental Procedure

2.2.1 Preparation of Starting Material

We assumed the solar abundance of elements as the standard composition of solid materials. In this experiment, the amorphous silicate was synthesized by a sol-gel method with the Mg/Si ratio of the solar composition of 1.07 (Anders & Grevesse, 1989). In general, iron is believed to form metal, sulfides, ferric, and/or ferrous silicates or oxides in circumstellar environments. In this chapter, we consider the extreme case, where all of the iron forms metal and/or sulfide, and is not contained in the silicates.

In the sol-gel method, magnesium ribbon was dissolved by 10% nitric acid first. Then, tetraethyl orthosilicate [TEOS, $Si(OC_2H_5)_4$], weighed to a mole ratio of MgO/SiO_2 of 1.07, was mixed into the solution. Ethanol was added as the same volume as the nitrate solution. The solution was stirred well by a stirrer magnet. Then, approximately 15% ammonia solution was added

to the solution slowly while the solution was stirred. In a short while, the solution began to gel by hydrolysis of TEOS; it was settled for about 2 days at room temperature until it gelled well. The material obtained was dried in air and roughly ground in an agate mortar. The gel was heated for final drying and evaporating NH_4NO_3 at 700°C for 20 hr with an electric furnace (KDF S-70) in the atmosphere.

2.2.2 Heating Experiments

Using the electric furnace, heating experiments were carried out to investigate temperature and time dependence of crystallization of the starting material. The starting material was contained in a platinum crucible and was heated in air at constant temperatures from 750 to 800°C for different durations from 0.5 to 504 hr (Table 2.1). The heating temperatures were measured using a K-type thermocouple. After heating, the crucible was cooled in water to quench the heated samples.

The phases of the starting material and the run products were determined by powder X-ray diffraction (XRD). For the XRD analysis, the samples were mounted on a thin glass fiber of 5 μm diameter with glycol phthalate as a glue. They were exposed to Mo Kα radiation ($\lambda = 0.710688\,\text{Å}$) and the diffraction patterns were measured with an imaging plate (Rigaku R-AXIS IV) at Osaka University.

For IR spectroscopic analysis, all samples were ground in an agate mortar for about 1 hr. The average diameter of the particles was less than 1 μm. These samples were dispersed and embedded in polyethylene. IR absorption spectra were obtained with a Fourier transform IR spectrometer (Nicolet Nexus 670) at Osaka University. The measured wavenumber range and resolution were 700-50 cm^{-1} (14 - 200 μm) and 1.0 cm^{-1}, respectively. The mass

Table 2.1: Heating conditions and results of the crystallization experiments. Phases and the degree of enstatite crystallization, C_{IR}, were determined by XRD and IR analyses, respectively. am = amorphous silicate, en = enstatite, fo = forsterite.

Temperature	Duration (hr)	Phase	C_{IR}
750°C	15	am	0
(1023 K)	168	en	0.29
	240	en≫fo	0.56
	336	en≫fo	0.60
	504	en≫fo	0.83
780°C	3	am	0
(1053 K)	5	am	0
	10	en	0.52
	13	en≫fo	0.56
	24	en≫fo	0.74
	72	en≫fo	0.73
790°C	1	am	0
(1063 K)	3	en	0.27
	4	en	0.50
	6	en	0.75
	18	en≫fo	0.87
	72	en≫fo	0.82
800°C	0.5	am	0
(1073 K)	1.5	en	0.64
	2	en	0.64
	3	en	0.68
	7	en≫fo	0.87

absorption coefficient, κ, was obtained from the equation

$$\kappa = S/M \ln(I_0/I), \tag{2.2}$$

where S is the cross section of the sample pellet, M is the mass of the sample in the pellet, and I_0 and I are the transmittance of a blank and sample pellet, respectively.

2.3 Results

2.3.1 X-ray Diffraction Analyses

We show, for example, an evolution of XRD patterns of the samples heated at 790°C for 1-72 hr (Fig. 2.1). The XRD profile of the starting material shows a halo pattern around 13° in 2θ, which is due to amorphous material. There is no clear peak of crystalline materials; however, there are some broad peaks at 16° and 27°, which are probably due to the amorphous material and/or the residual organic materials used in the sol-gel processing. After 1 hr heating at 790°C, crystalline materials were not observed. However, the halo profile shifted to around 12° in 2θ and two broad peaks disappeared. In the profile of the sample heated at 790°C for 4 hr, diffraction peaks due to enstatite ($MgSiO_3$) were recognized together with a weak amorphous halo. The diffraction pattern could be explained as clinoenstatite rather than orthoenstatite. The halo almost disappeared by heating at 790°C for 6 hr. After further heating, a small amount of forsterite (Mg_2SiO_4) was also crystallized. Considering a chemical composition of the starting material, whose Mg/Si ratio (= 1.07) is slightly higher than the enstatite stoichiometry (Mg/Si = 1), this is a reasonable result that enstatite and the very small

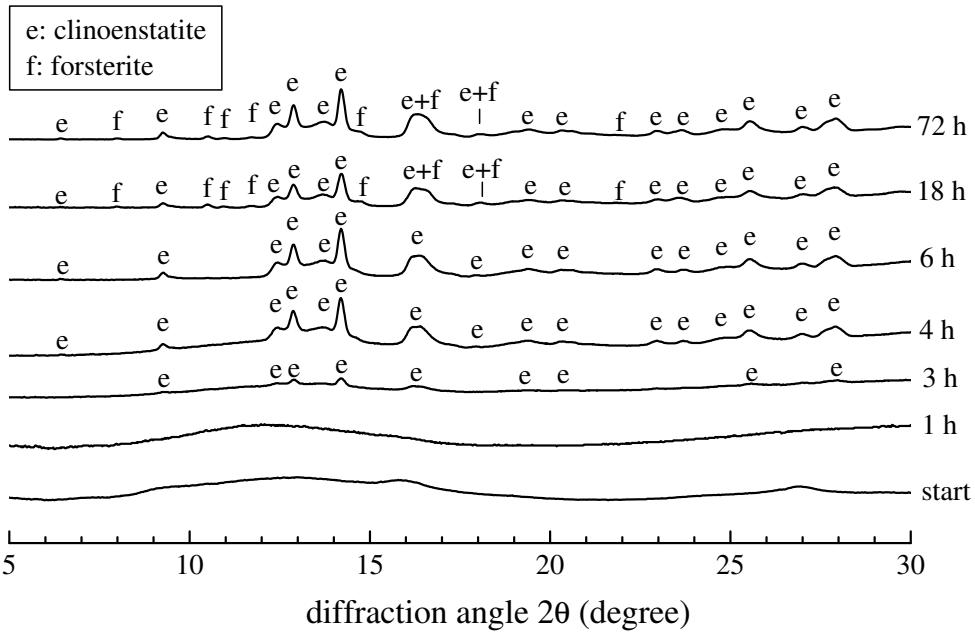

Figure 2.1: Powder X-ray diffraction patterns of the starting material and the run products of the heating experiments at 790°C. e = clinoenstatite, f = forsterite. X-ray wavelength was $\lambda = 0.710688$ Å. Enstatite was crystallized together with the small amount of forsterite.

amount of forsterite were crystallized from the starting material. The sample completely crystallized from the starting material (Mg/Si ratio = 1.07) should contain 90.5% of enstatite and 9.5% of forsterite in weight percents. Over the temperature range (750-800°C), enstatite was always crystallized from the amorphous starting material, and the amounts of forsterite were always very small when forsterite was present (Figs. 2.2, 2.3 and 2.4, Table 2.1). This shows that the difference of the heating temperatures almost affected timescales of crystallization of enstatite.

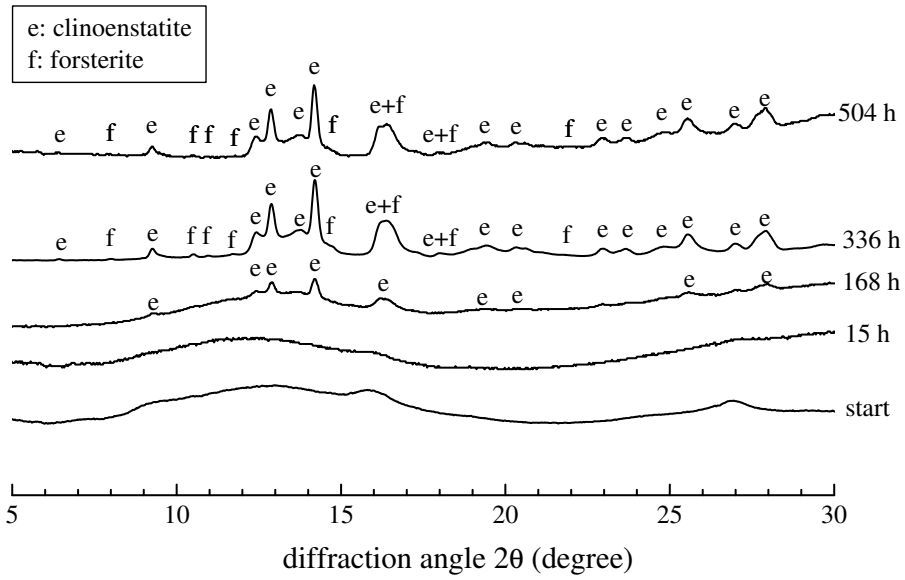

Figure 2.2: Powder X-ray diffraction patterns of the starting material and the run products of the heating experiments at 750°C. e = clinoenstatite, f = forsterite. X-ray wavelength was $\lambda = 0.710688\,\text{Å}$.

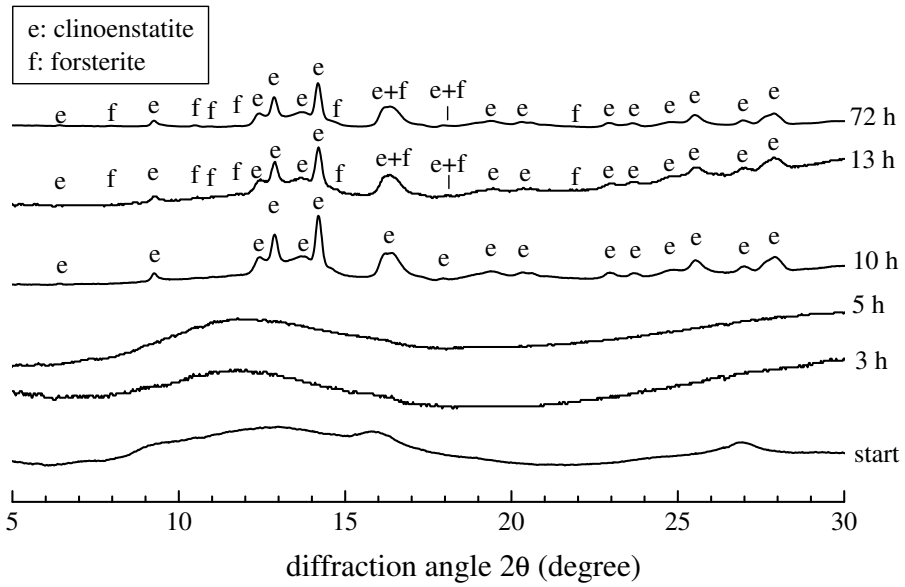

Figure 2.3: Powder X-ray diffraction patterns of the starting material and the run products of the heating experiments at 780°C. e = clinoenstatite, f = forsterite. X-ray wavelength was $\lambda = 0.710688\,\text{Å}$.

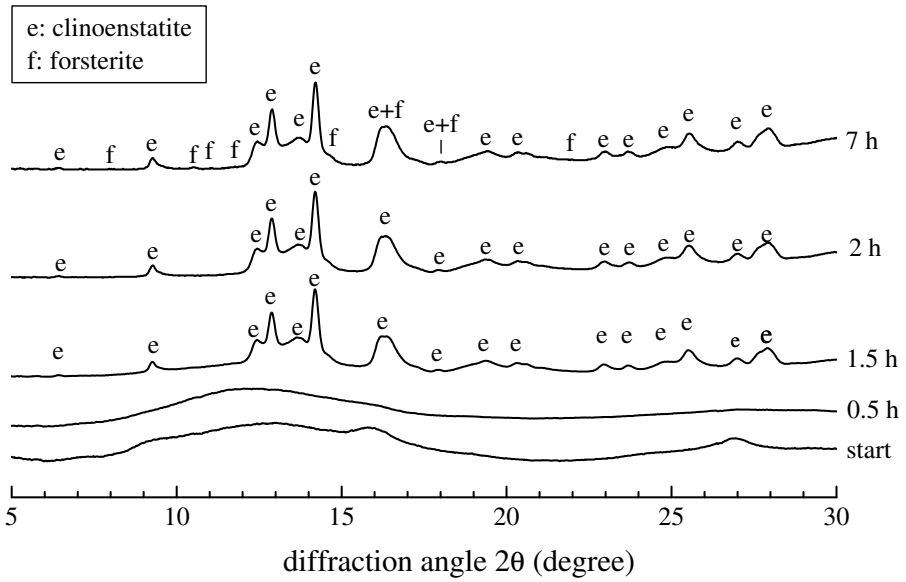

Figure 2.4: Powder X-ray diffraction patterns of the starting material and the run products of the heating experiments at 800°C. e = clinoenstatite, f = forsterite. X-ray wavelength was $\lambda = 0.710688$ Å.

2.3.2 IR Spectroscopic Analyses

IR spectra of the starting material and the samples heated at 790°C for 1-72 hr are shown in Fig. 2.5. In the spectrum of the starting material, broad and smooth absorption feature was observed around 21 μm, which is typical for amorphous silicates and originates from the O-Si-O bending vibrational mode. After 1 hr heating, an 18 μm shoulder appeared and the amorphous feature became broader than that of the starting material. This spectral evolution is caused by a structural change of the amorphous silicate, which is also observed in the XRD profile (Fig. 2.1). In the spectra of the sample heated for more than 1 hr, the sharp peaks of enstatite (15.4, 18.1, 19.7, 20.7, 21.6, 23.3, 23.7, 27.1, 28.1, 29.3, 33.0, 33.8, 35.5, 35.9, 41.1 and 43.9 μm) grew gradually from the broad amorphous feature. After further heating for 6 hr,

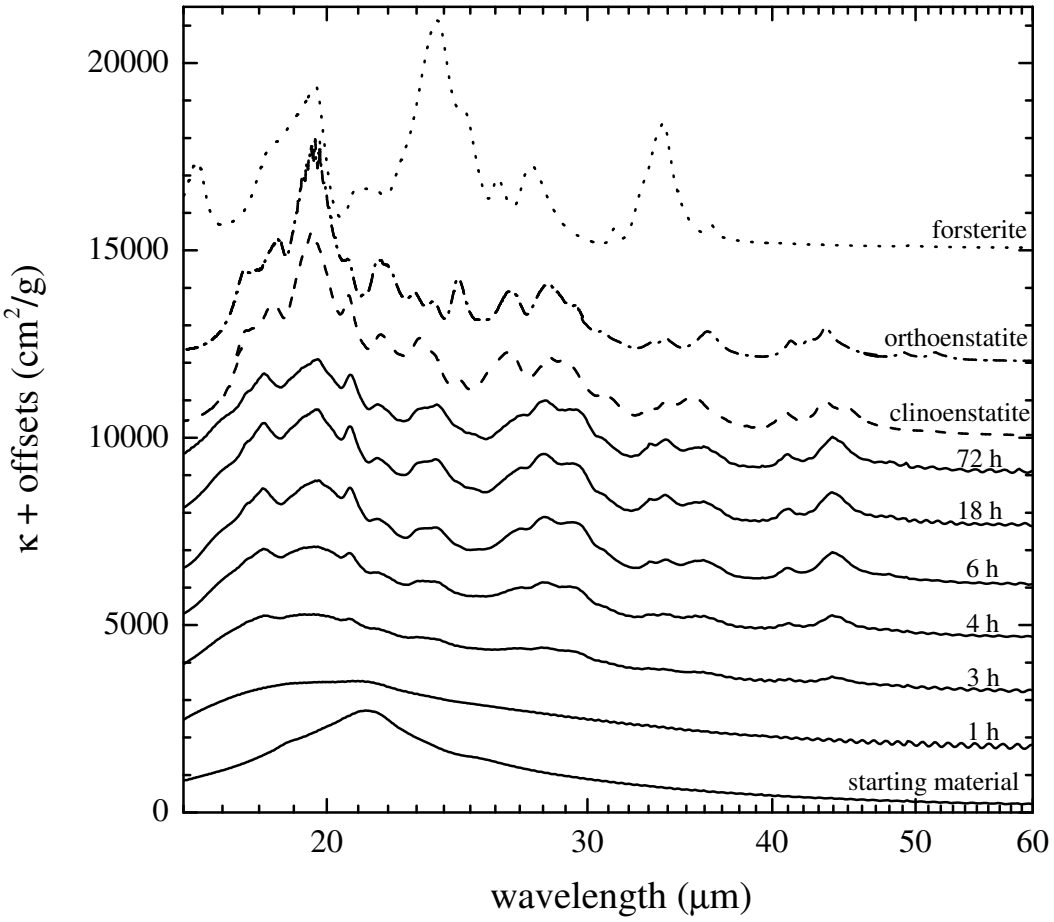

Figure 2.5: IR spectra of the samples heated at 790°C for different durations together with the spectra of clinoenstatite (*dashed line*, Chihara et al. (2002)), orthoenstatite (*dot-dashed line*, Chihara et al. (2002)) and forsterite (*dotted line*, Koike et al. (2003)).

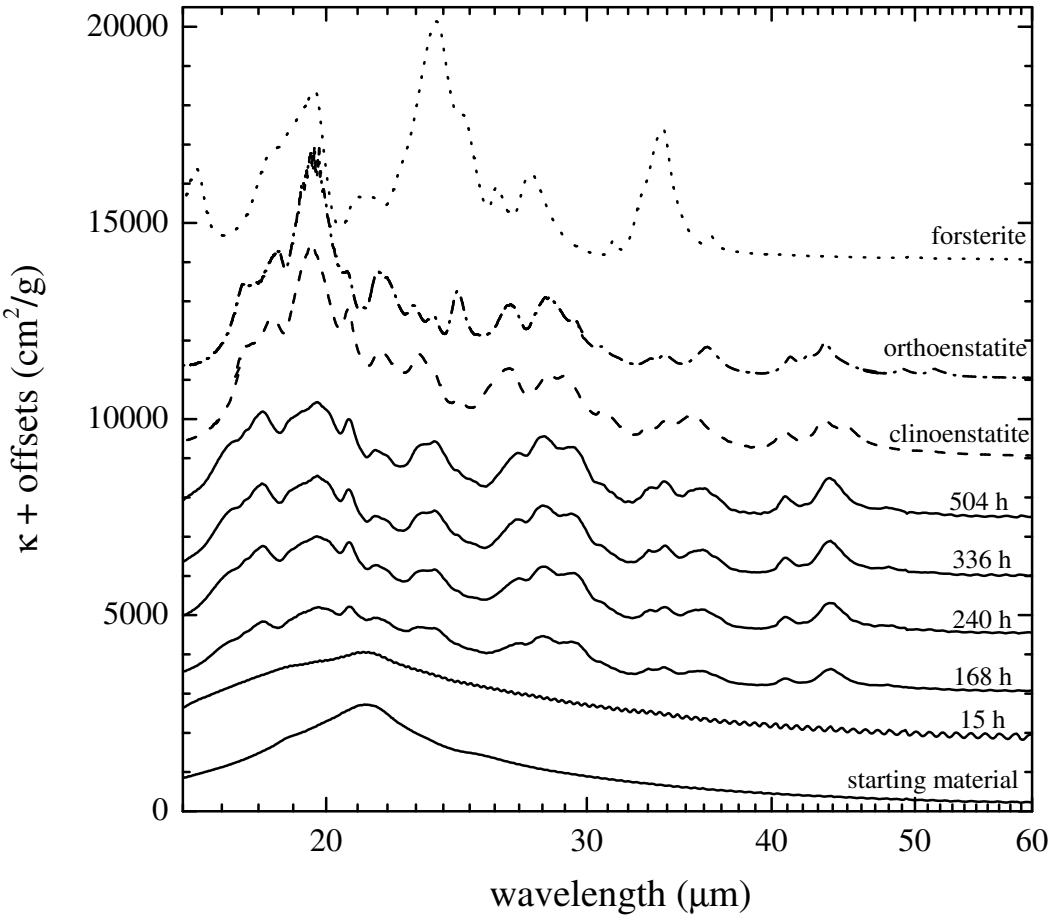

Figure 2.6: IR spectra of the samples heated at 750°C for different durations together with the spectra of clinoenstatite (*dashed line*, Chihara et al. (2002)), orthoenstatite (*dot-dashed line*, Chihara et al. (2002)) and forsterite (*dotted line*, Koike et al. (2003)).

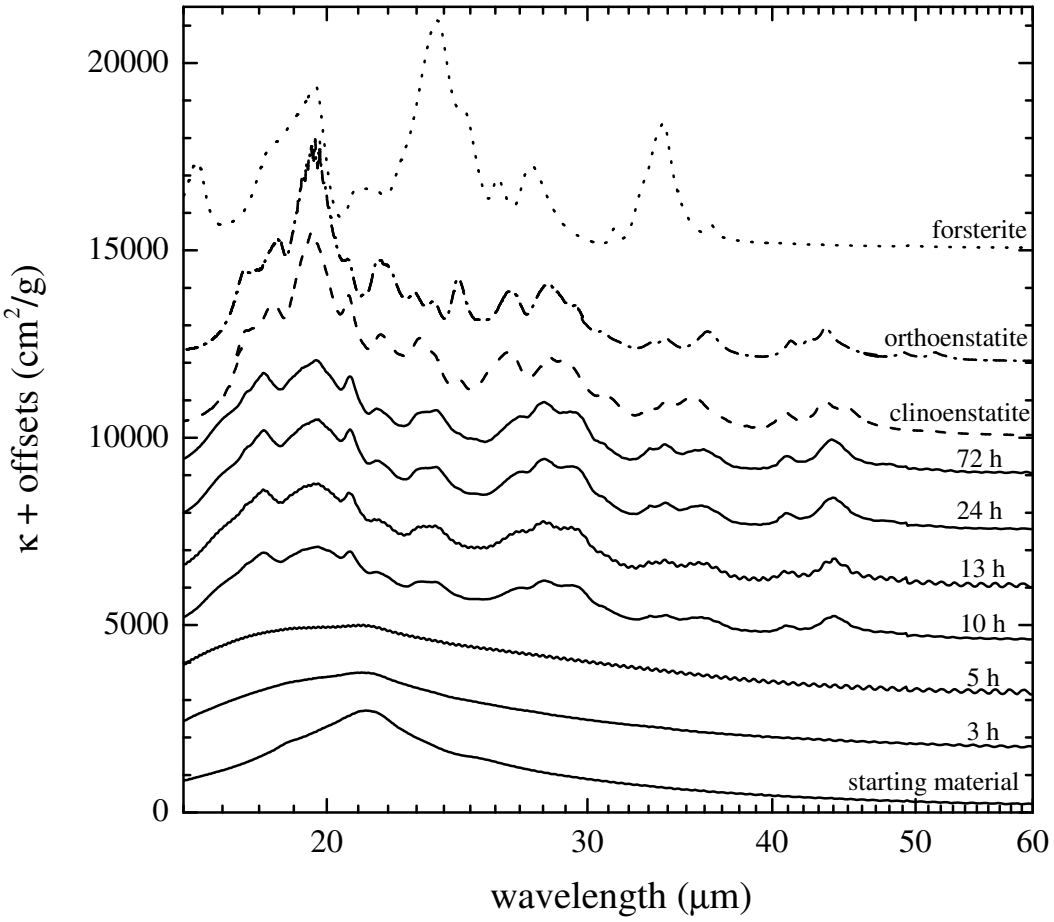

Figure 2.7: IR spectra of the samples heated at 780°C for different durations together with the spectra of clinoenstatite (*dashed line*, Chihara et al. (2002)), orthoenstatite (*dot-dashed line*, Chihara et al. (2002)) and forsterite (*dotted line*, Koike et al. (2003)).

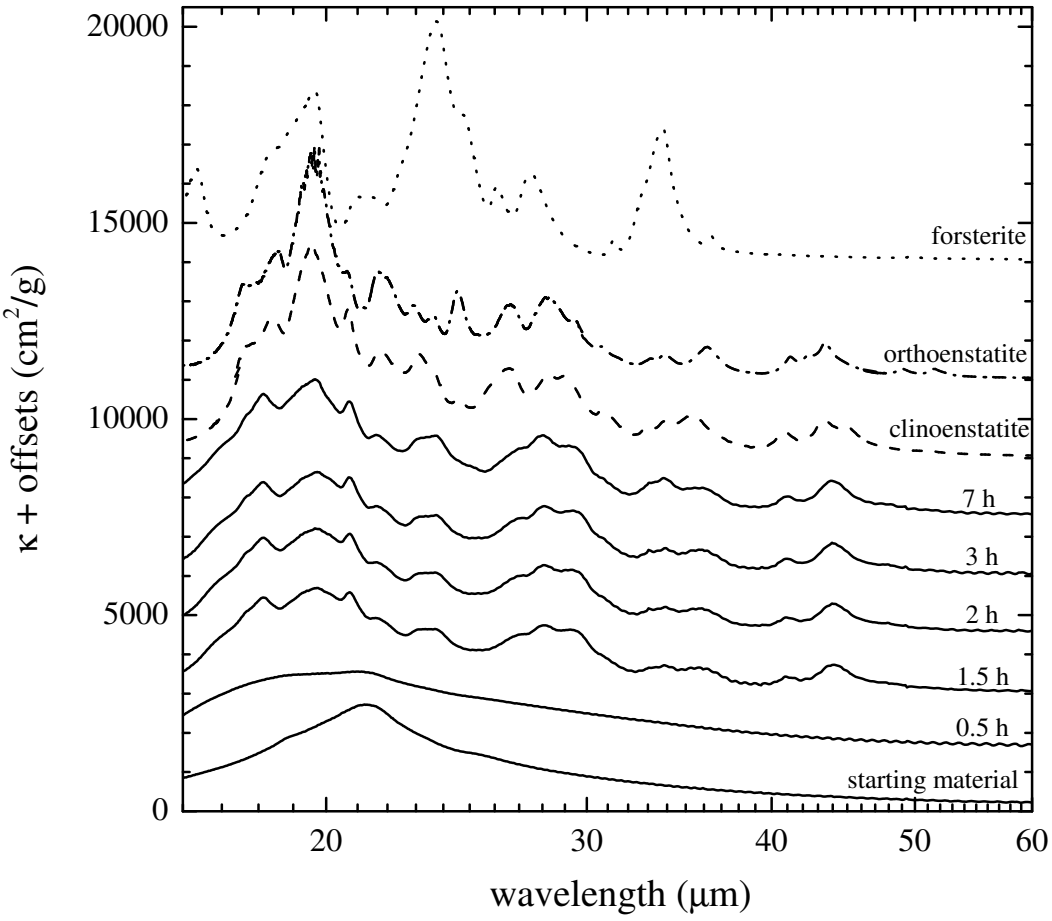

Figure 2.8: IR spectra of the samples heated at 800°C for different durations together with the spectra of clinoenstatite (*dashed line*, Chihara et al. (2002)), orthoenstatite (*dot-dashed line*, Chihara et al. (2002)) and forsterite (*dotted line*, Koike et al. (2003)).

crystallization was almost completed. The IR feature of forsterite could not be observed because the amount of forsterite was much smaller than that of enstatite (Fig. 2.1). The spectral evolutions at 750, 780 and 800°C were in a manner similar to that at 790°C (Figs. 2.6, 2.7 and 2.8). Time required for the complete crystallization was approximately 240, 13 and 2 hr at 750, 780 and 800°C, respectively.

Compared with the spectra of clinoenstatite and orthoenstatite (*dashed* and *dot-dashed lines*, respectively (Chihara et al., 2002)), the spectra of the heated samples showed partly different features; the 19.7 and 26.6 μm peaks were much weaker than those of Chihara et al., even though the crystallization was almost completed. Detailed spectroscopy was performed and discussed in chapter 3.

2.3.3 Estimation of Degree of Crystallization

In order to analyze the crystallization processes quantitatively, we estimated the degree of crystallization by fitting of the IR spectra (Murata et al., 2007). We assumed that a mass absorption coefficient of a partially crystallized silicate sample, κ, can be written as

$$\kappa = (1 - C_{\rm IR})\,\kappa_{\rm as} + C_{\rm IR}\,\kappa_{\rm xt}, \tag{2.3}$$

where $\kappa_{\rm as}$ and $\kappa_{\rm xt}$ are the mass absorption coefficients of an amorphous silicate and a crystalline silicate (enstatite), respectively, and $C_{\rm IR}$ is the degree of enstatite crystallization. Here, we ignored the presence of forsterite, because its amount was very small. The IR spectra of the heated samples were fitted using eq. 2.3 by the least-squares method, and the values of $C_{\rm IR}$ were obtained (Table 2.1). We used the spectrum of clinoenstatite (Chihara et al., 2002) as $\kappa_{\rm xt}$. We did not use the spectrum of the starting material as

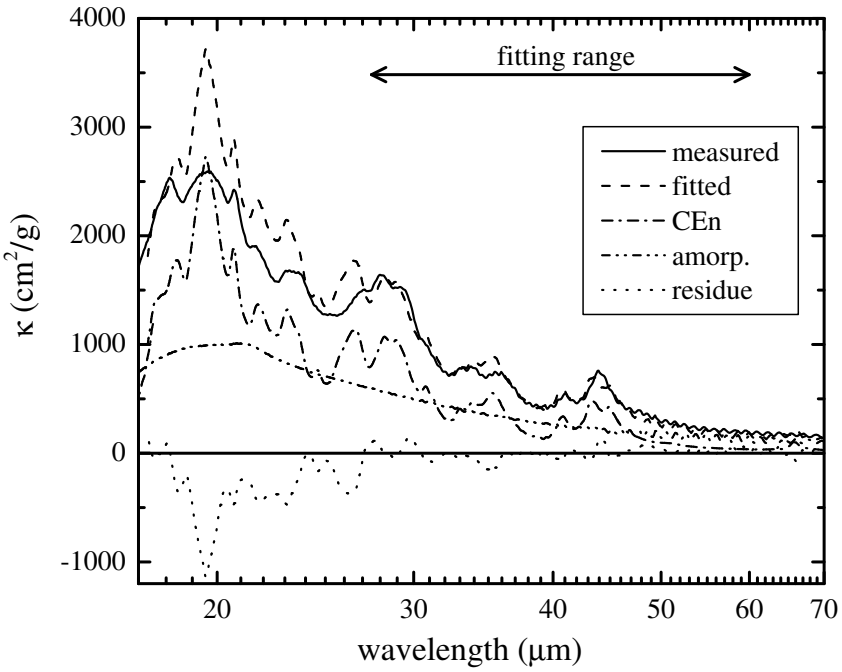

Figure 2.9: Fitting result of the sample heated at 790°C for 4 hr. The solid, dashed and dotted lines indicate the observed and fitted spectra and their residue, respectively. The fitted spectrum is the sum of spectra of amorphous silicate (*dot-dot-dashed line*) and clinoenstatite (*dot-dashed line*). The fitting range was set to from 27.5 to 60 μm.

$\kappa_{\rm as}$ because its amorphous feature changed in the early stage of the spectral evolutions. Thus, we used that of the sample heated at 790°C for 1 hr, which is a typical amorphous feature among the heated samples. The fit was made in the range from 27.5 to 60 μm, since the 19.7 and 26.6 μm peak heights are different from those in Chihara et al. (2002) and the signal to noise ratio is low in the spectra at longer than 60 μm. This fitting range can also avoid the change of the amorphous feature at around 20 μm through the crystallization.

An example of the fitting results is shown in Fig. 2.9 (790°C, 4 hr). The

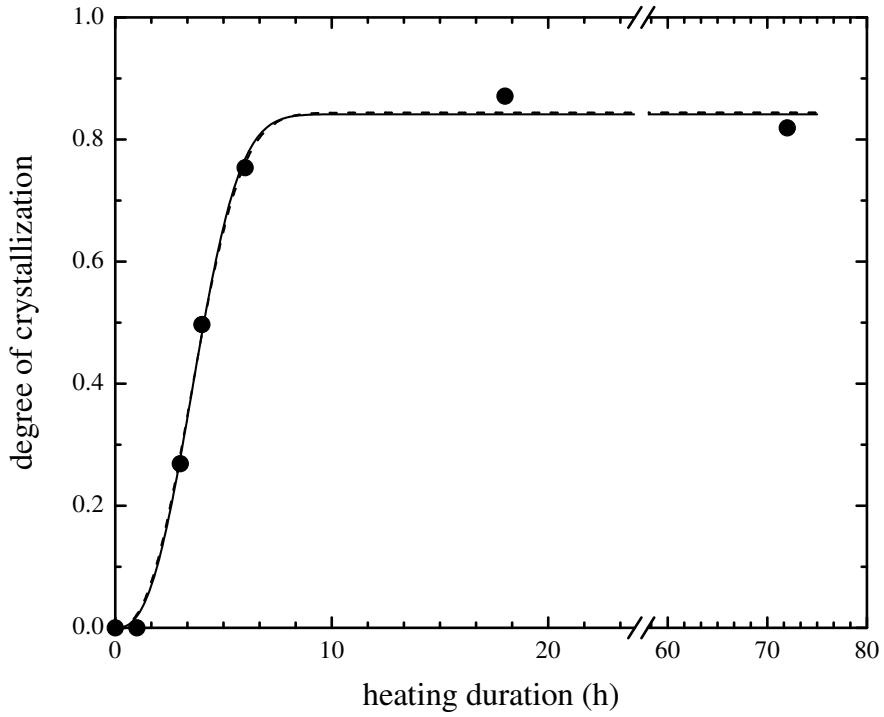

Figure 2.10: Degree of crystallization estimated from the IR spectra vs. heating duration at a constant heating temperature (790°C). The solid line shows the best-fit curve from eq. 2.4. The dashed line shows the best-fit curve from eq. 2.4 with a constant value of n of 2.5.

solid, dashed, and dotted lines indicate the measured and fitted spectra and their residue, respectively. From the fitting, we can obtain the degree of crystallization, C_{IR}. There is not a large difference between the measured and the fitted spectra in the fitting range from 27 to 60 μm.

C_{IR} of the samples heated at 790°C is plotted against the heating durations in Fig. 2.10. C_{IR} did not increase in the early stage of crystallization. After that, C_{IR} increased as the duration of heating increased, and saturated at a constant value of approximately 0.85. In order to confirm whether the residual amorphous silicate remains or not, we performed the additional

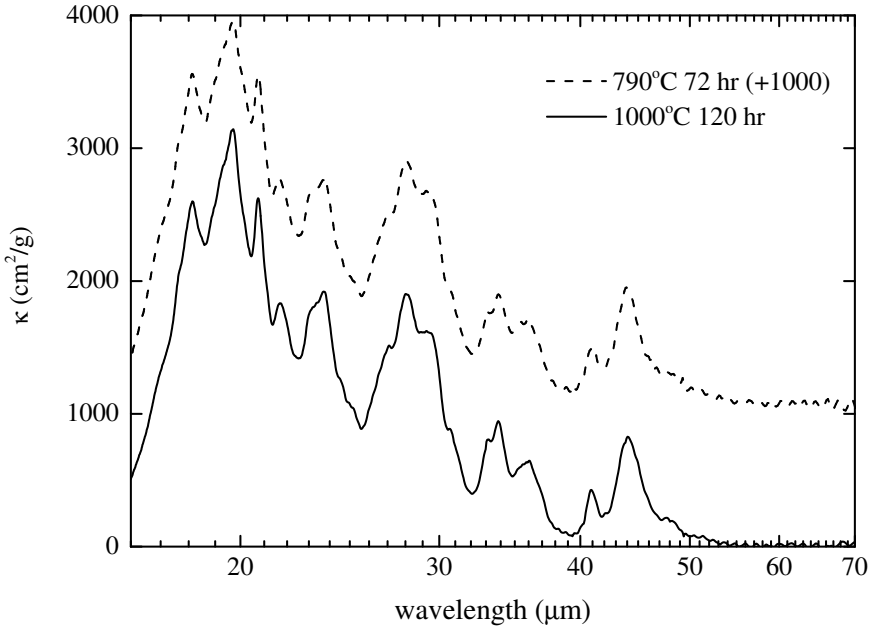

Figure 2.11: IR spectra of the samples heated at 1000°C for 120 hr and heated at 790°C for 72 hr.

heating experiment at 1000°C for 120 hr, and there was no discrepancy of the IR spectra between 1000°C and the other heating temperatures (Fir. 2.11). This result strongly indicates that the crystallization was completed in the saturated stage of the spectral evolutions.

2.3.4 Formulation of Crystallization Process

We formulated the time evolution of the degree of crystallization (Fig. 2.10) using the Johnson-Mehl-Avrami (JMA) equation (Johnson & Mehl, 1939; Avrami, 1939; Murata et al., 2007),

$$C_{\rm IR} = C_\infty \left[1 - \exp\{-(t/\tau)^n\}\right], \tag{2.4}$$

where τ is the time constant of the crystallization, n is a kinetic parameter,

which depends on crystallization kinetics, and C_∞ is a constant corresponding to C_{IR} at infinite time.

The solid line in Fig. 2.10 shows the best-fit curve found with the χ^2 method using eq. 2.4 with values for n, τ and C_∞ of 2.61 ± 0.25, 15300 ± 400 s, and 0.841 ± 0.017, respectively (determination coefficient is 0.997). The obtained value of C_∞ was slightly lower, taking into account the chemical composition of the starting material (Mg/Si ratio = 1.07, which should contain 90.5% of enstatite and 9.5% of forsterite in weight percents). However, the values of n and τ are not largely affected by the underestimation of C_∞, as long as a degree of the underestimation are similar among the different run products.

According to Burke (1965), the JMA equation with $n = 2.5$ was derived from a theoretical crystallization model of three-dimensional diffusion-controlled growth with a constant nucleation rate. The value of $n = 2.61 \pm 0.25$ in the present experiment is close to 2.5, and three-dimensional crystal growth is suitable for crystallization of enstatite. Murata et al. (2007) performed crystallization experiments of a FeO-bearing amorphous silicate, which contained pre-existing nucleation sites, and the growth curve of C_{IR} did not show nucleation delay (chapter 4). In the present experiments, the growth curve of C_{IR} is sigmoidal in shape and the crystallization did not proceed until 1 hr (Fig. 2.10). The structural change of the amorphous silicate in the early stages of heating, which was observed in XRD patterns (Fig. 2.1) and IR spectra (Fig. 2.5), is related to the nucleation: the enstatite nucleation requires the change in the amorphous structure. Thus, the crystallization of enstatite in this study occurred by nucleation and diffusion-controlled crystal growth.

τ in eq. 2.4 is involved in several parameters, such as nucleation rate and

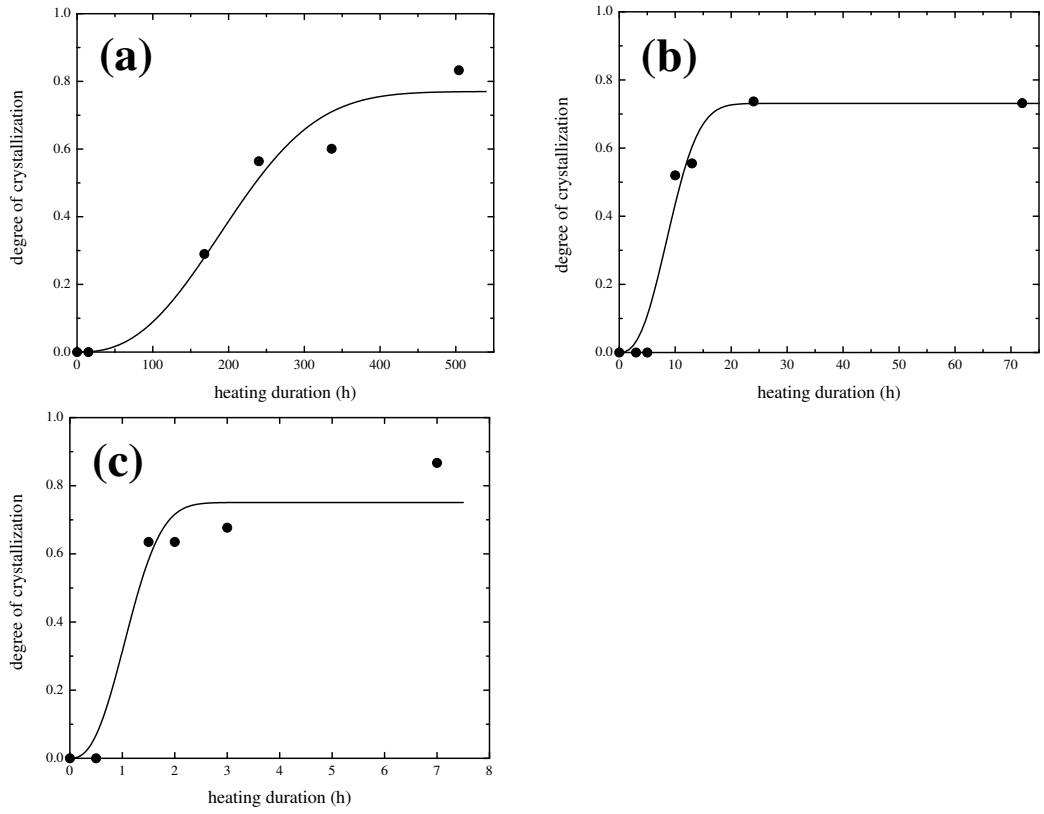

Figure 2.12: Degree of crystallization estimated from the IR spectra vs. heating duration at a constant heating temperature ((a) 750°C, (b) 780°C, (c) 800°C). The solid line shows the best-fit curve from eq. 2.4 with a constant value of n of 2.5.

diffusion coefficient. Different kinetic processes give different definitions of τ. Therefore, we fixed a value of n as 2.5, which means three-dimensional diffusion-controlled growth with a constant nucleation rate, for estimation of τ in the crystallization processes at different temperatures. The growth curves of C_{IR} were fitted by eq. 2.4 with $n = 2.5$ at all the experimental temperature (Fig. 2.12). The values of τ at 750, 780, 790 and 800°C were 832000 ± 80000, 37400 ± 3300, 15400 ± 400 and 4600 ± 730 s, respectively.

2.4 Discussion

2.4.1 Activation Energy of Crystallization

The Arrhenius plot of the time constant of crystallization, τ, shows a linear line (Fig. 2.13) and was fitted using eq. 2.1. The values of $E_{\mathrm{c}}/k_{\mathrm{B}}$ and $\ln(\nu_0)$ were 1.12 (± 0.03) $\times 10^5$ K and 93 ± 2, where ν_0 is in s^{-1}, respectively.

From theoretical and experimental approaches, the parameters of the JMA equation have been investigated (Ruitenberg et al., 2002; Ranganathan & von Heimendahl, 1981). Assuming the nucleation rate per unit volume of untransformed material, I, has an Arrhenian temperature dependence, we have

$$I = I_0 \exp(-E_{\mathrm{n}}/k_{\mathrm{B}}T), \tag{2.5}$$

where E_{n} is the activation energy for nucleation and I_0 is a constant. For a growth rate, G, we also have

$$G = G_0 \exp(-E_{\mathrm{g}}/k_{\mathrm{B}}T), \tag{2.6}$$

where E_{g} is the activation energy for growth and G_0 is a constant. In the case

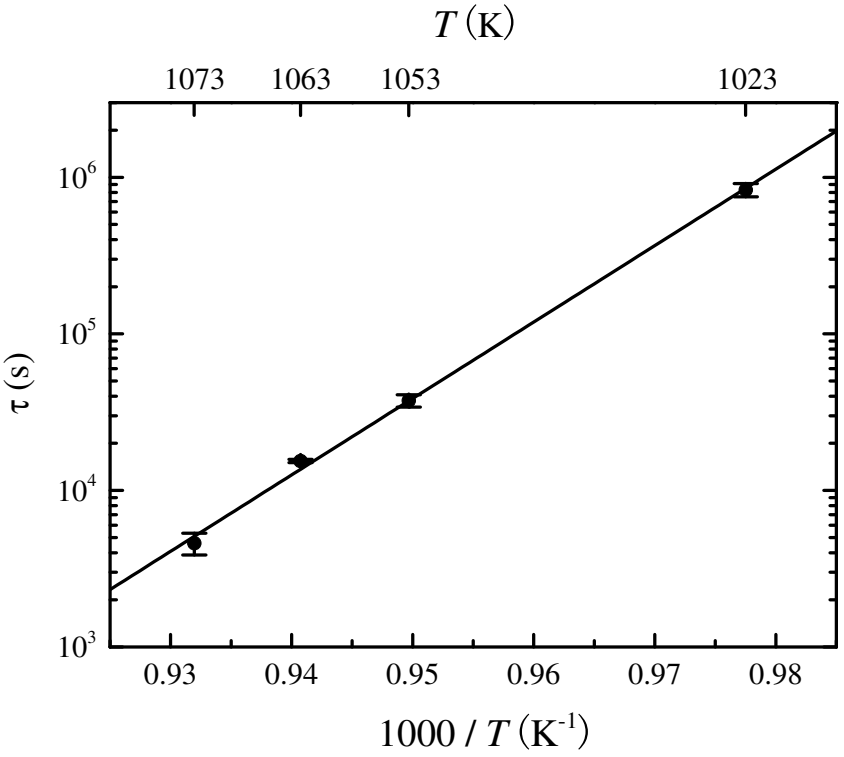

Figure 2.13: The Arrhenius plot of τ vs. T^{-1} over the temperature range 750 - 800°C. The bars are the fitting errors of the eq. 2.4.

of crystallization including nucleation with a constant rate and 3-dimensional diffusion-controlled growth ($n = 2.5$), empirical formulae were given as,

$$E_{\rm c} = (2/5)E_{\rm n} + (3/5)E_{\rm g}, \tag{2.7}$$

$$\ln(\nu_0) = (2/5)\ln(I_0) + (3/5)\ln(G_0). \tag{2.8}$$

In this study, the value of $E_{\rm c}$ is larger than that estimated by Brucato et al. (1999) and Fabian et al. (2000). The large value of $E_{\rm c}$ is probably due to nucleation, taking into account a value of an activation energy of diffusion of Mg or other cations in silicate materials (2×10^4 - 5×10^4 K, Freer (1981);

Hofmann (1980)). The assumption of ν_0 in the previous studies also affected the value of E_c. The value of ln (ν_0) obtained in this experiment was larger than the assumed value (~ 30) in their studies. Small changes in the slope of the trend line in an Arrhenius plot result changes in the intercept, ln(ν_0). In the present experiment, a structural change of the amorphous silicate may affect the value of ln(ν_0). In addition, I_0 in eq. 2.5 has small temperature dependence in the strict sense. Thus, the intercept of the Arrhenius plot should be considered as empirical.

2.4.2 Implication for Enstatite Crystallization under Circumstellar Conditions

The Arrhenius relation does not change as long as the crystallization process (nucleation and diffusion-controlled growth in the present case) is not changed. Thus, we assumed that eq. 2.1 can be extrapolated to temperature lower than the experimental range by about 170 K in following discussion. We also assumed that crystallization in circumstellar environments needs nucleation and crystal growth, including the change in the amorphous structure (Figs. 2.1 and 2.5), as well as this study. Note that crystallization kinetics depends on nature of circumstellar amorphous silicates. If amorphous silicates already contain some crystallites before heating, for example, nucleation is not initially needed and growth proceeds from the crystallites (Murata et al., 2007).

Figure 2.14 shows time required for crystallization with degrees of crystallization of 0.05, 0.5 and 0.99, derived from eqs. 2.1 and 2.4. We assumed C_∞ in eq. 2.4 as unity for simplicity. It is clearly shown that crystallization depends very strongly on temperature due to the large E_c, and thus enstatite crystallization is kinetically inhibited in cold environments. Forsterite crys-

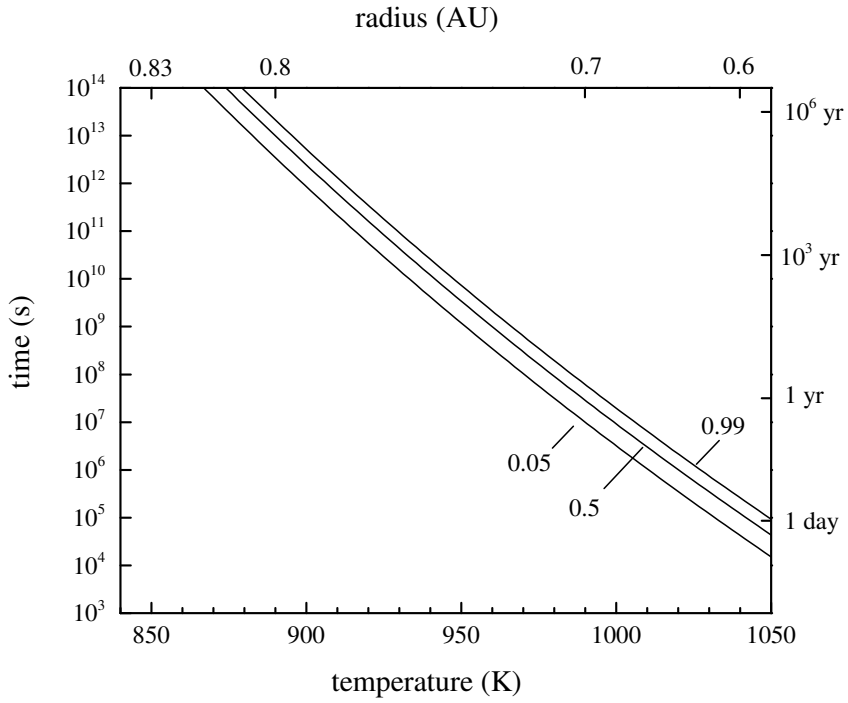

Figure 2.14: Time required for crystallization with degrees of crystallization of 0.05, 0.5 and 0.99. Upper abscissa shows the corresponding radius in the accretion disk, which was calculated by Bell et al. (1997) for the accretion rate of 10^{-7} $M_{\odot}yr^{-1}$ and the viscous efficiency factor, α, of 0.01.

tallization is an important process in circumstellar environments; however, is not discussed here, because of lack of appropriate experimental data.

Enstatite around Young Stars

The present experimental result indicates that enstatite crystallization around young stars occurs only in the inner disk region.

During the evolutional stage of pre-main-sequence stars of the active disk phase, the disk accretes material, such as amorphous silicates, from the surrounding cloud. The accretion of matter provides the energy production by

viscous dissipation and makes the disk temperature high. During the active disk phase, there is a region in the inner disk where the temperature is above the crystallization temperature. In the general understanding of low-mass star formation, the accretion from the surrounding cloud typically lasts for 10^5 yr (André & Montmerle, 1994; Bachiller, 1996). Thus, the upper limit of crystallization timescale in the active disk phase is the order of magnitude of 10^5 yr ($= 10^{12}$ s). The detection of enstatite around a T-Tauri star with a stellar age of 1 Myr (Honda et al., 2006) supports the upper limit. Based on Fig. 2.14, we suggested that most of amorphous silicates cannot crystallize in situ at temperature lower than 870 K.

In order to discuss silicate crystallization region in protoplanetary disks, the temperature distribution in the disk is required. The upper abscissa of Fig. 2.14 shows the temperature distribution at the mid-plane estimated for the evolutional stage of the accretion disk in radius (Bell et al., 1997), according to the model with the typical values of viscous efficiency factor, α, and accretion rate of 0.01 and 10^{-7} $M_{\odot}yr^{-1}$, respectively. If timescale for the active disk phase ($\sim 10^5$ yr) is considered, in situ crystallization of enstatite occurs in the inner disk region within $\sim$ 0.8 AU. Note that the radius determined in this way depends greatly on the accretion model itself and the parameters used. From the model with the parameters of α of 0.01 and accretion rate of 10^{-6} $M_{\odot}yr^{-1}$, enstatite is expected to be crystallized within $\sim$ 2.3 AU.

When the supply of material from the surrounding cloud has exhausted, further accretion onto the star proceeds only on an extremely low level (referred to as the passive disk phase). Under these conditions, as the energy production by viscous dissipation can be fully neglected, the region whose temperature is higher than 870 K will be smaller than in the active disk

phase. Thus, enstatite crystallization is limited only in the vicinity of the inner edge of disks.

Enstatite around Evolved Stars

In stellar outflows of oxygen-rich evolved stars, it is considered that silicate condensation starts at a temperature of about 1000 K (e.g., Gail & Sedlmayr, 1999; Sogawa & Kozasa, 1999). The silicates should be amorphous at the initial stage of condensation. During the annealing process of a temperature decrease, amorphous silicate dust can crystallize (Sogawa & Kozasa, 1999). For an investigation of the crystallization process of enstatite in stellar outflows, we assumed a simple model that circumstellar amorphous silicate, with constant outward velocity, v, decreases its temperature, T, monotonically. We also assumed that the dust temperature decreases exponentially with the cooling timescale of silicate dust, $\tau_{\rm cool}$,

$$T(t) = T_c \exp\left(-t/\tau_{\rm cool}\right), \tag{2.9}$$

where $T_{\rm c}$ is the condensation temperature (Seki & Hasegawa, 1981).

Using eqs. 2.1, 2.4 and 2.9, the estimation of degree of crystallization was carried for the parameters v = 10 km/s (Sogawa & Kozasa, 1999), $\tau_{\rm cool}$ = 10^7 s (Kozasa & Hasegawa, 1987; Yamamoto & Hasegawa, 1977) and $T_{\rm c}$ = 1010, 1020, 1030, 1040, and 1060 K. Figure 2.15 shows the degree of crystallization as a function of the distance from the condensation radius, $\rm R_c$, normalized by the stellar radius, $\rm R_\star$. Sogawa & Kozasa (1999) calculated $\rm R_c$ around AGB stars as approximately $10\rm R_\star$. It is clearly indicated that the crystalline evolution proceeds only in the vicinity of the condensation radius. Furthermore, the final degree of crystallization has large dependence on $T_{\rm c}$. When $T_{\rm c}$ is above 1060 K, crystallization is complete during cooling

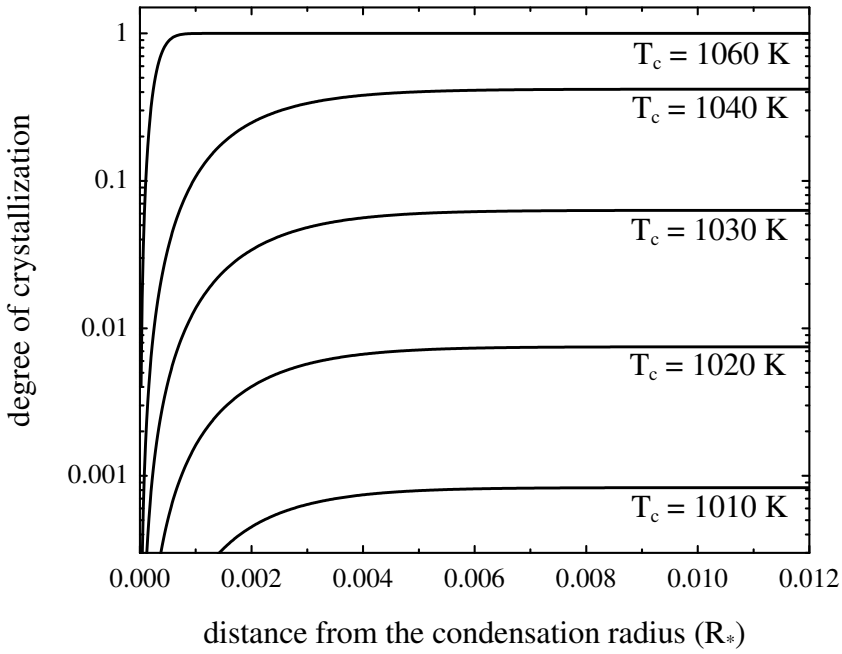

Figure 2.15: Degree of crystallization vs. distance from the condensation radius. We assumed C_∞ in eq. 2.4 as unity for simplicity.

of dust. On the other hand, when T_c is below 1010 K, the silicate dust remains virtually as amorphous. Partial crystallization occurs only in the narrow T_c interval, 1010-1060 K. Sogawa & Kozasa (1999) indicated that T_c has large dependence on mass-loss rate. Since mass-loss rate is not always constant value, T_c should vary (Fig. 2.16). When an average value of T_c is about 1000 K, a major fraction of silicate dust cannot be crystallized, while a minor fraction of it, whose T_c is above 1010 K, can be crystallized partially or completely. As a total fraction, a partial crystallization is achieved.

2.5 Conclusions

Heating experiments of an amorphous magnesium silicate with the Mg/Si ratio of 1.07 were carried out at 750 - 800°C to examine the process and con-

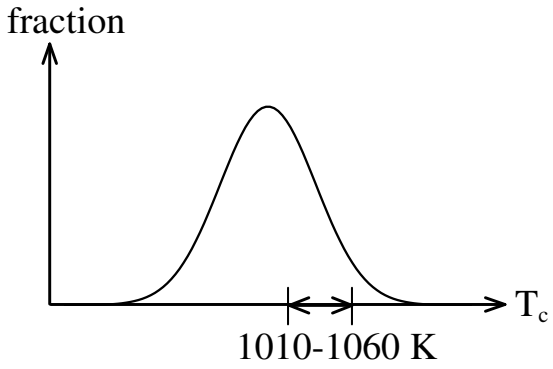

Figure 2.16: Schematic of $T_{\rm c}$ distribution of silicate dust. In a range of $T_{\rm c}$ between 1010 K and 1060 K, partial crystallization of enstatite will occur. Above those temperatures, completely crystallization is expected. Below 1010 K, silicates remain amorphous.

dition of the crystallization. We evaluated quantitatively the time constant of the enstatite crystallization, τ, in the Johnson-Mehl-Avrami equation, and determined the activation energy as 1.12×10^5 K. The large value of the activation energy indicates kinetic inhibition of the crystallization in cold regions. We showed that enstatite can crystallize only in the inner disk region around young stars and in the vicinity of the condensation zone around evolved stars. In stellar winds of evolved stars, the final degree of crystallization of silicate dust has large dependence on the condensation temperatures.

Bibliography

Anders, E., & Grevesse, N. 1989, Geochim. Cosmochim. Acta, 53, 197

André P, & Montmerle T. 1994, ApJ, 420, 837

Avrami, M. 1939, J. Chem. Phys., 7, 1103

Bachiller, R. 1996, ARA&A, 34, 111

Bell, K. R., Cassen, P. M., Klahr, H. H., & Henning, T. 1997, ApJ, 486, 372

Brucato, J. R., Colangeli, L., Mennella, V., Palumbo, P., & Bussoletti, E. 1999, A&A, 348, 1012

Burke, J. 1965, The Kinetics of Phase Transformation in Metals (England: Pergamon Press Limited)

Chihara, H., Koike, C., Tsuchiyama, A., Tachibana, S., & Sakamoto, D. 2002, A&A, 391, 267

Fabian, D., Jäger, C., Henning, Th., Dorschner, J., & Mutschke, H. 2000, A&A, 364, 282

Freer, R. 1981, Contrib. Miner. Petrol., 76, 440

Gail, H.-P. & Sedlmayr, E. 1999, A&A, 347, 594

Gail, H.-P. 2002, in Astromineralogy, ed. Henning, Th. (Lecture Notes in Physics 609; New York: Springer), 55

Hofmann, A. W. 1980, in Physics of Magmatic Processes, ed. Hargraves, R. B. (Princeton University Press), 385

Honda, M., et al. 2006, ApJ, 646, 1024

Johnson, W. A., & Mehl, R. F. 1939, Trans. Am. Inst. Min. Metal Eng., 135, 416

Kemper, F., Vriend, W. J., & Tielens, A. G. G. M. 2004, ApJ, 609, 826

Koike, C., Chihara, H., Tsuchiyama, A., Suto, H., Sogawa, H., & Okuda, H. 2003, A&A, 399, 1101

Kozasa, T., & Hasegawa, H. 1987, Prog. Theor. Phys., 77, 1402

Murata, K., Chihara, H., Tsuchiyama, A., Koike, C., Takakura, T., Noguchi, T., & Nakamura, T. 2007, ApJ, 668, 285

Ranganathan, S., & von Heimendahl, M. 1981, J. Mater. Sci. 16, 2401

Ruitenberg, G., Petford-Long, A. K., & Doole, R. C. 2002, J. Appl. Phys, 92, 3116

Seki, J. & Hasegawa, H. 1981, Prog. Theor. Phys., 66, 903

Sogawa, H., & Kozasa, T. 1999, ApJ, 516, L33

Waelkens, C. et al. 1996, A&A, 315, L245

Waters, L. B. F. M., et al. 1996, A&A, 315, L361

Yamamoto, T. & Hasegawa, H. 1977, Prog. Theor. Phys., 58, 816

Chapter 3

Low-Temperature Infrared Spectra of Heated Amorphous Magnesium Silicate

In this chapter, we measured low-temperature IR spectra of the heated amorphous silicate obtained in chapter 2. We discovered that circumstellar dust emission of enstatite is similar to the IR feature measured in this experiment.

3.1 Introduction

On the basis of the observations of the Infrared Space Observatory (ISO), silicate dust in circumstellar regions seemed to be partially crystallized (e.g., Waelkens et al., 1996; Waters et al., 1996). A detailed analysis of the ISO spectra of evolved stars showed that most of IR emission features by crystalline silicates can be fitted well with laboratory spectra of enstatite and forsterite (Molster et al., 2002). However, Molster et al. mentioned problems of fit (Fig. 3.1). The enstatite features at 20 and 27 μm in the ISO spectra

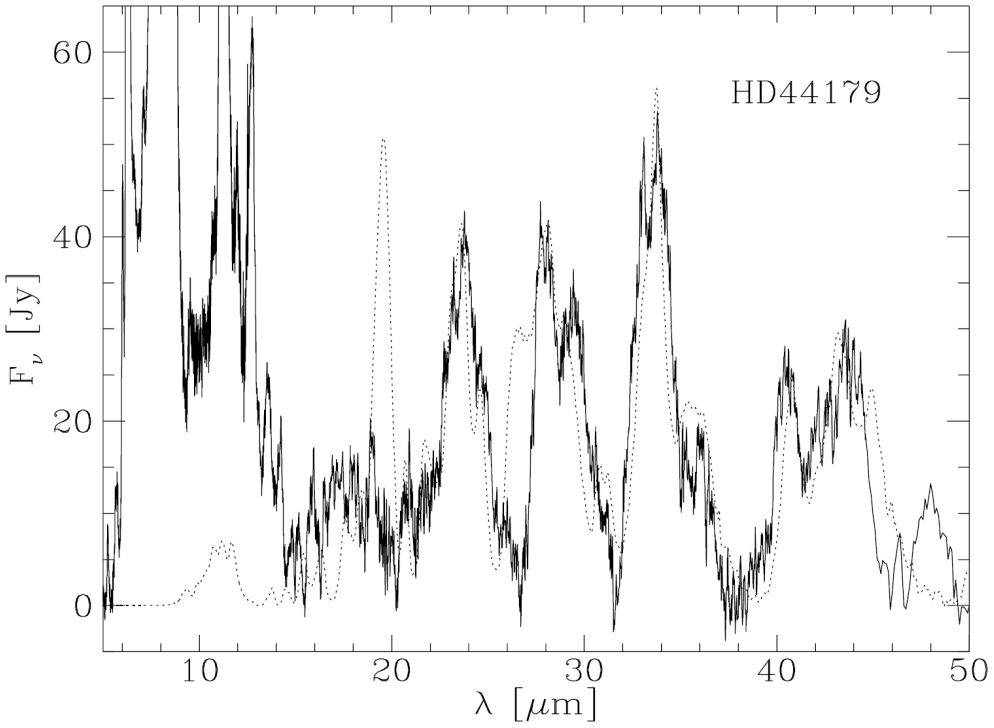

Figure 3.1: A fitting result of the continuum subtracted spectrum of HD44179 (solid line). A dotted line shows a model spectrum using laboratory spectra of enstatite and forsterite. Below 15 μm the spectrum is dominated by PAH features. Figure taken from Molster et al. (2002).

were often too weak relative to other enstatite features. In contrast, although the strong 48 μm peak was observed in at least six ISO spectra out of fourteen sample stars, the laboratory spectrum of enstatite does not show the peak at 48 μm. Furthermore, the 70 micron band of enstatite, which is a good indicator of the differences between ortho and clinoenstatite (Chihara et al., 2002), have not been reported, even for the objects in which the existence of enstatite has been considered.

Laboratory data for comparison of the astronomical spectra were obtained using fine powdered single crystalline samples (e.g., Chihara et al.,

2002; Koike et al., 2003, 2006). However, it is expected that crystalline silicates around evolved stars are not single crystal, taking into account that the crystalline silicates are considered to undergo heating processes in the circumstellar regions and be rearranged from amorphous into crystalline structures at relatively low temperatures at around 1000 K (e.g., Gail & Sedlmayr, 1999; Sogawa & Kozasa, 1999). In the previous chapter, we showed that the IR spectra of enstatite which was crystallized from the amorphous silicate had partly different features from that obtained by Chihara et al., especially 19.6 and 26.6 μm. These peaks correspond to the peaks which are badly fitted to the observed ones. A spectroscopy using a sample crystallized via thermal heating, which simulates expected circumstellar processes, becomes important for detailed astromineralogy.

A large amount of the silicate emission often originates from dust particles over the temperature range of 50 to 200 K. It is well known that the dust temperature strongly affects the frequency, bandwidth, and band structure of vibrational bands of solids. Therefore, in order to compare laboratory spectra with the observed ones, the laboratory spectra should be measured with sample cooling at the low temperatures. In this chapter, we performed low-temperature IR spectroscopy of the heated amorphous magnesium silicate obtained in the previous chapter. A transmission electron microscopy (TEM) of this sample was also carried to investigate difference of lattice structure between our sample and single crystalline one.

3.2 Experimental Procedure

We synthesized an amorphous magnesium silicate sample in the MgO-SiO_2 system with the Mg/Si ratio of 1.07 (solar composition) by the sol-gel

method as a circumstellar dust analog. For crystallization of the amorphous silicate, it was heated in the atmosphere at 1063 K for 72 hr. The heated amorphous silicate sample (hereafter labeled as HAS) was identified by X-ray diffraction as enstatite and the small amount of forsterite (Fig. 2.1). Details are given in chapter 2.

For IR spectroscopic analysis, the sample was ground in an agate mortar for about 1 hr. The average diameter of the particles was less than 1 μm. The sample was dispersed and embedded in polyethylene. For sample cooling, a closed-cycle helium cryostat equipped with polyethylene IR optical windows was adopted. The setup has already been described by Koike et al. (2006). IR absorption spectra were obtained with a Fourier transform IR spectrometer (Nicolet Nexus 6700) at Ritsumeikan University at room temperature, 200, 150, 100, 50 and 9 K. The measured wavenumber range and resolution were 700 - 50 cm^{-1} (14 - 200 μm) and 1.0 cm^{-1}, respectively. In the far-IR region (334 - 50 cm^{-1}), we also measured at the lower resolution of 2 cm^{-1} to avoid interference fringe. The mass absorption coefficient, κ, was obtained from the equation

$$\kappa = S/M \ln(I_0/I), \tag{3.1}$$

where S is the cross section of the sample pellet, M is the mass of the sample in the pellet, and I_0 and I are the transmittance of a blank and sample pellet, respectively.

For TEM observation, the samples were embedded in epoxy resin and microtomed by the Leitz-Reichert Super Nova ultramicrotome, and observed with JEOL JEM-2000FX II at Ibaraki University.

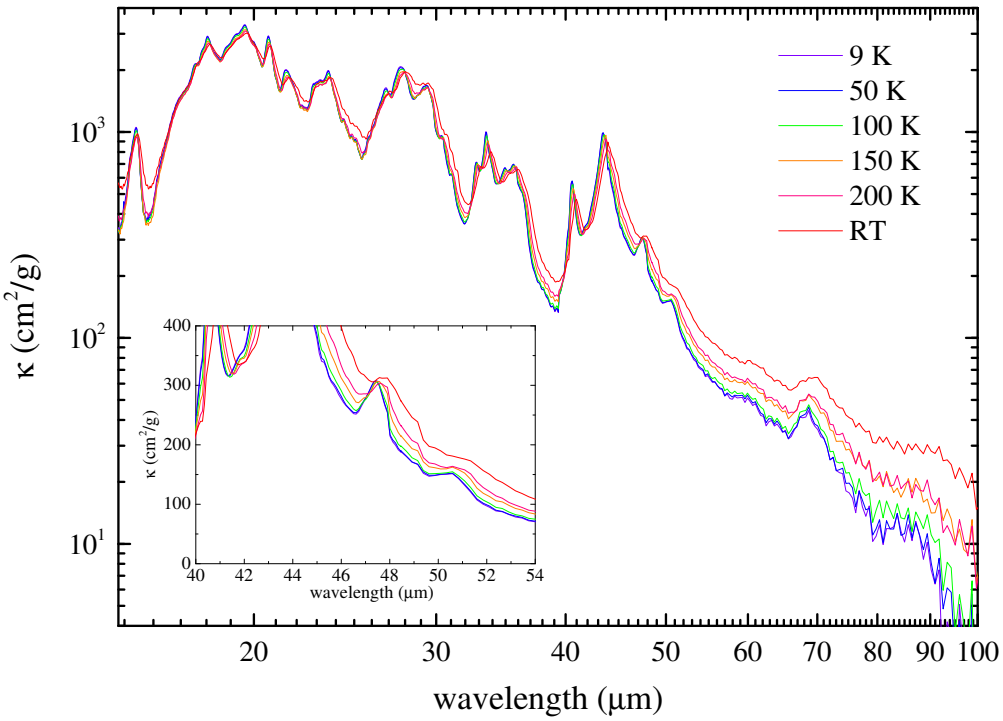

Figure 3.2: IR spectra of the sample in this study at room temperature, 200, 150, 100, 50 and 9 K.

3.3 Results & Discussion

3.3.1 IR spectra

The mass absorption coefficients of HAS are shown in Fig. 3.2. The intensity and width of each band increased and decreased, respectively, as temperature decreased, and a new band appeared at around 48 μm. Furthermore, the peak positions of the bands shifted to shorter wavelengths as temperature decreased.

The obtained spectrum is compared with data of single crystalline enstatite (hereafter labeled as SCE) in Fig. 3.3. While the whole feature resembles each other, 19.9 and 26.6 μm peaks of HAS are weaker than those

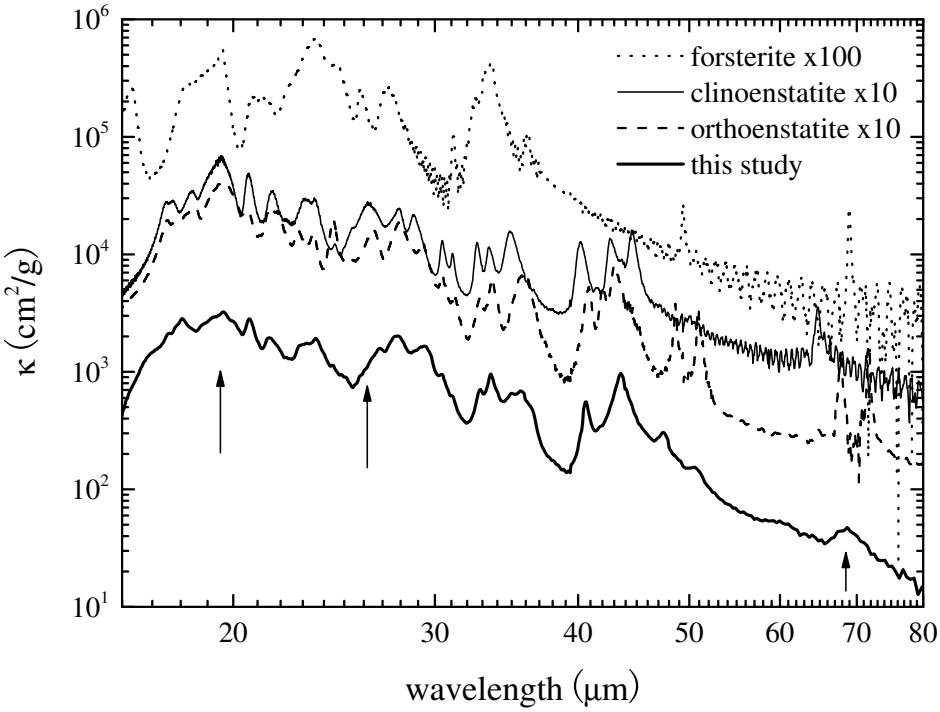

Figure 3.3: IR spectra of the sample in this study together with clino and orthoenstatite (Koike, private communication) and forsterite (Koike et al., 2006). All the spectra were measured at 100 K. The arrows indicate peaks largely different from powdered single crystalline sample of enstatite. For clarity, each spectrum is multiplied.

of SCE. The new band at 48 μm is observed in the spectra of HAS. Furthermore, there is a large difference between HAS and SCE at around 70 μm. HAS has a very broad peak at 69 μm, although clino and orthoenstatite have a sharp peak at 65 μm and twin peaks at 68 and 72 μm, respectively. This discrepancy between HAS and SCE is suggested to be caused by a discrepancy in lattice structure of enstatite, because far-IR resonance reflects vibration of metal ions and chains of SiO_4-tetrahedrons.

Figure 3.4 shows a TEM image and a selected area electron diffraction

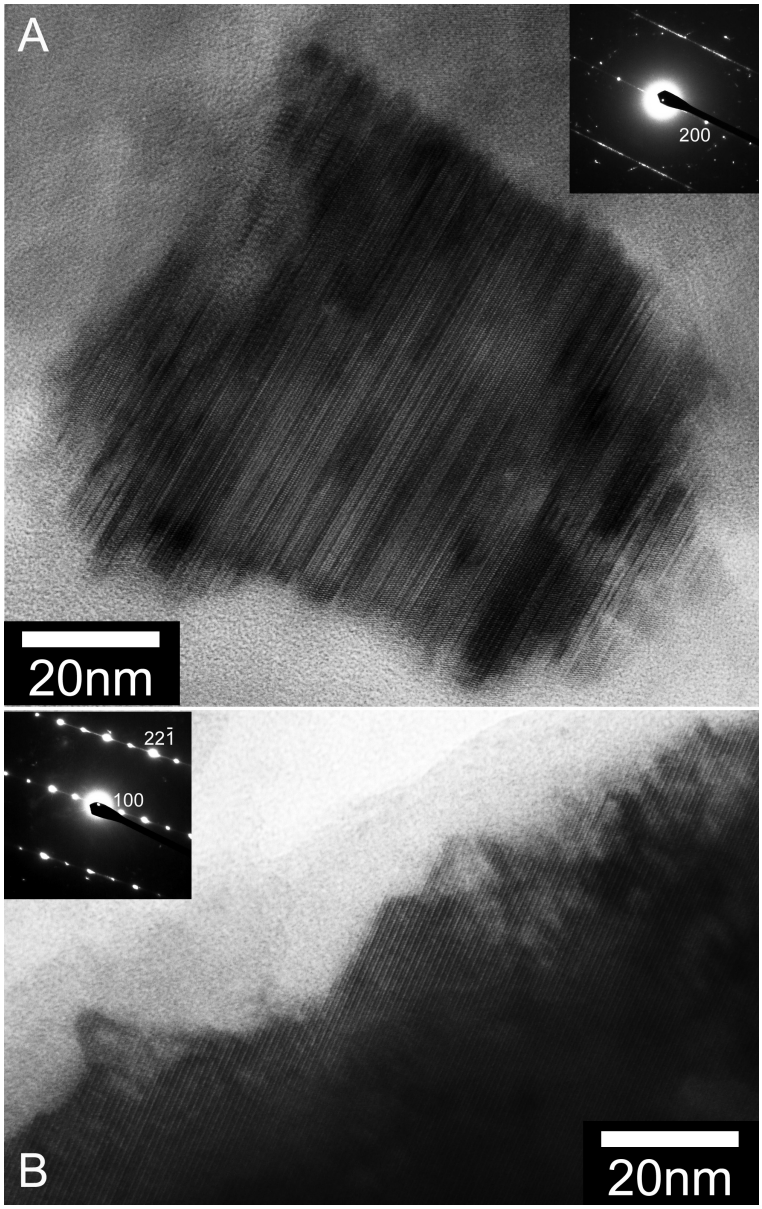

Figure 3.4: TEM images and SAED patterns of (A) enstatite in the sample in this study and (B) fine powdered single crystal of clinoenstatite viewed parallel to a*-axis.

(SAED) pattern of HAS. For comparison, we also show those of a powdered sample of SCE. A typical size of enstatite in HAS is about 100 nm. The image shows that a large amount of (100) stacking faults are accumulated. A much diffuse (100) diffraction spot was shown in the SAED pattern of HAS (Fig. 3.4 A), while (200) diffraction spot was observed. This is caused by (100) stacking faults. A strong streak parallel to the a*-axis is also due to (100) stacking disorder. In contrast, SCE has a well-ordered lattice structure (Fig. 3.4 B). Diffraction spots were observed clearly in the SAED pattern of SCE. A streak was much weaker than that of HAS. These TEM and SAED results strongly indicate that a discrepancy of the IR features was caused by (100) stacking faults.

3.3.2 Comparison with Observations

We compared the obtained spectra with astronomical data in Figs. 3.5 and 3.6. The continuum subtracted spectra in the lower panel in Figs. 3.5 and 3.6 indicate the ISO data of the sources HD 44179 and MWC 922 (Molster et al., 2002), respectively. HD 44179 is an evolved star surrounded by the Red Rectangle nebula. The evolutionary status of MWC 922 is unclear. The spectra revealed the existence of a significant amount of crystalline silicates. We produced simple model spectra of mixtures of enstatite and forsterite using the following formula,

$$F_{model} = \sum_{i=1}^{2} m_i \kappa_i(T) B(T), \tag{3.2}$$

where m_i is a multiplication factor which is related to the total mass of dust species i, $\kappa_i(T)$ is the mass absorption coefficient of dust species i at dust temperature T, and $B(T)$ is the Planck function of T. $B(T)$ of 150 K is adopted for this comparison. For the first model (thin lines in the upper

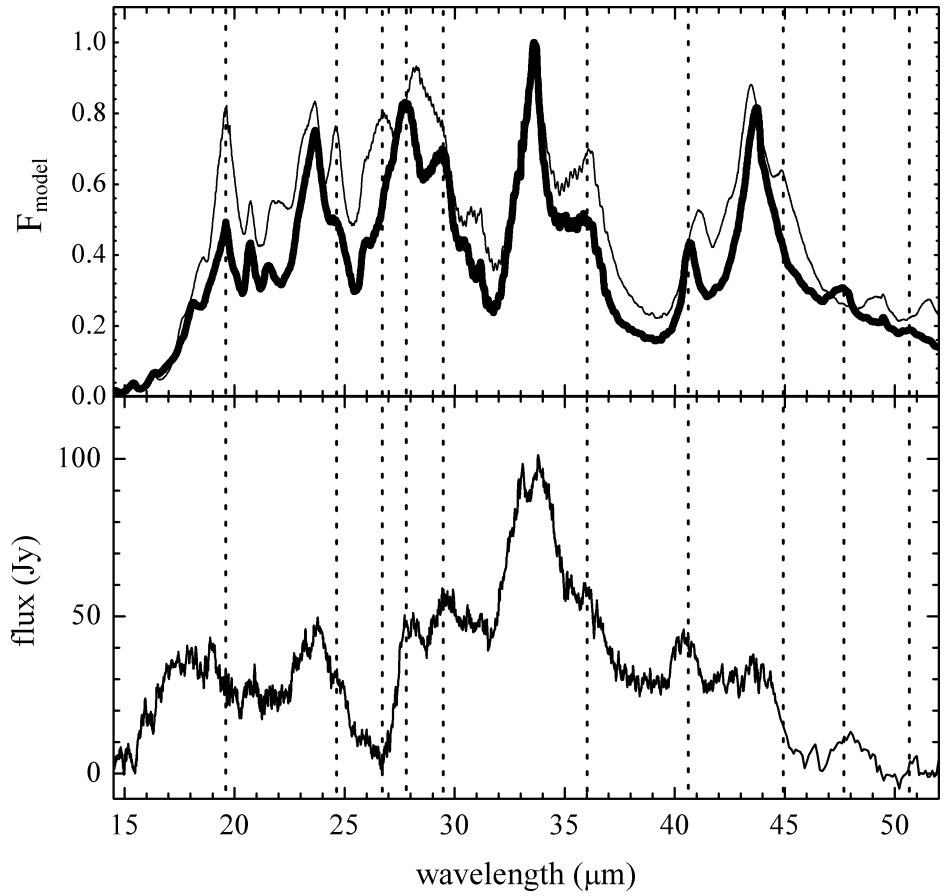

Figure 3.5: Comparison of the continuum subtracted spectrum of HD 44179 with the model (1) (SCE + forsterite, thin line) and (2) (HAS + forsterite, thick line) multiplied by the Planck function of 150 K and normalized to one.

panel in Figs. 3.5 and 3.6), we assumed κ of enstatite as 50% clinoenstatite and 50% orthoenstatite using SCE data. This is the same assumption as in Molster et al. (2002). Forsterite to enstatite mass ratios, m_{en}/m_{fo}, of HD 44179 and MWC 922 were roughly evaluated by Molster et al. as 4.0 and 2.7, respectively. We also used the values in this comparison. The whole features of the model spectra are almost consistent with the observed spectra. However, there are some differences of detailed spectral features

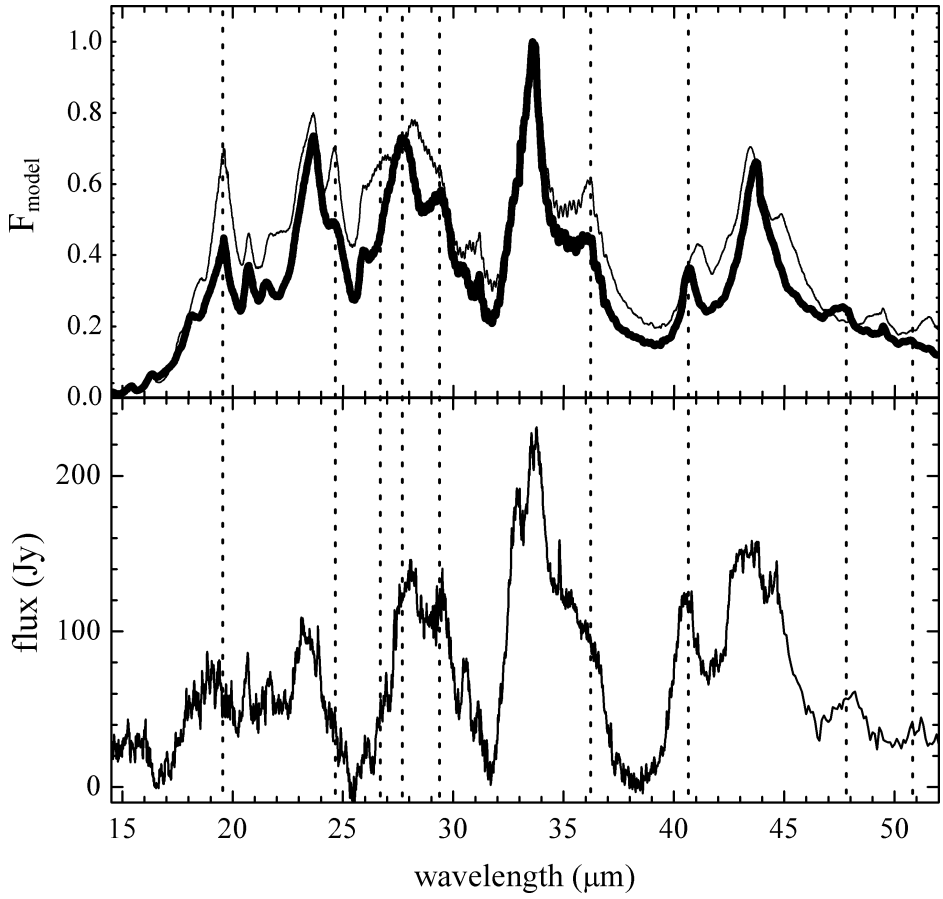

Figure 3.6: Comparison of the continuum subtracted spectrum of MWC 922 with the model (1) (SCE + forsterite, thin line) and (2) (HAS + forsterite, thick line) multiplied by the Planck function of 150 K and normalized to one.

among them, especially 20, 27 and 48 μm bands as mentioned before (see also Fig. 3.1). The next model is a mixture of forsterite and HAS (thick lines in the upper panel in Figs. 3.5 and 3.6). We used the same values of T and m_{en}/m_{fo} as those in the first model. In this spectra, peaks at 20 and 27 μm became weaker than those of the first model, and 48 μm peak appeared. Thus, this model spectrum should be better fitted to the observed spectra of HD 44179 and MWC 922. Some detailed features (indicated by

vertical dashed lines) are also consistent. In addition to those, the broad peak around 70 μm of HAS (Fig. 3.2) agree with the observation: The 70 μm band of enstatite has not been detected even when enstatite is considered to exist. Since this feature of HAS is too broad and the peak position overlaps with that of forsterite, a detection of the 70 μm feature by observation seems to be close to impossible. Therefore, we conclude that the HAS spectrum represents the observed spectra better than the SCE one does. This suggests that circumstellar enstatite has stacking faults, and are different from the crystalline structure as well as SCE.

In the previous laboratory crystallization experiments, a spectroscopy of the crystallized materials was performed. Fabian et al. (2000) measured IR spectra of enstatite which was crystallized from $MgSiO_3$ glass. The IR spectrum showed that peaks at 20, 26 and 70 μm seem to be relatively weak. Brucato et al. (1999) also monitored mid-IR spectral evolution during Mg-rich pyroxene crystallization. Although they observed only limited range of wavelengths, the 20 μm peak was weaker than that of natural crystalline sample. These results are consistent with the present crystallization experiment. The IR features of enstatite are suggested to reflect its formation process and physical and chemical condition, such as thermal heating at low temperature about 1000 K.

3.4 Conclusions

A low-temperature IR spectroscopy of the sample obtained in chapter 2 was given. There was a discrepancy between the IR feature of enstatite obtained in this experiment and that obtained in the spectroscopic experiments using single crystals. This reflects a discrepancy in stacking disorder

of enstatite. Circumstellar dust emission of enstatite was similar to the IR feature measured in this experiment. This result suggested that circumstellar enstatite has stacking faults and is different from the single crystalline enstatite.

Bibliography

Brucato, J. R., Colangeli, L., Mennella, V., Palumbo, P., & Bussoletti, E. 1999, A&A, 348, 1012

Chihara, H., Koike, C., Tsuchiyama, A., Tachibana, S., & Sakamoto, D. 2002, A&A, 391, 267

Fabian, D., Jäger, C., Henning, Th., Dorschner, J., & Mutschke, H. 2000, A&A, 364, 282

Gail, H.-P. & Sedlmayr, E. 1999, A&A, 347, 594

Koike, C., Chihara, H., Tsuchiyama, A., Suto, H., Sogawa, H., & Okuda, H. 2003, A&A, 399, 1101

Koike, C., et al. 2006, A&A, 449, 583

Molster, F. J., Waters, L. B. F. M., Tielens, A. G. G. M., Koike, C., & Chihara, H. 2002, A&A 382, 241

Sogawa, H., & Kozasa, T. 1999, ApJ, 516, L33

Waelkens, C. et al. 1996, A&A, 315, L245

Waters, L. B. F. M., et al. 1996, A&A, 315, L361

Chapter 4

Olivine Crystallization from Pre-existing Nucleation Site in FeO-bearing Silicate

In this chapter, we show that crystallization processes in circumstellar regions should depend on the properties of amorphous silicates, such as the existence of crystallites and/or the Fe content, from the experiment of a FeO-rich amorphous silicate. This chapter is a modified version of the paper published as Murata et al., 2007, ApJ, 668, 285.

4.1 Introduction

The previous studies of crystallization experiments were performed using Mg-silicates with simple compositions in the Mg-Si-O system. However, in general, if the solar abundance is considered, the chemical composition of amorphous silicates in circumstellar environments must be more complicated than the simple ones. Anhydrous chondritic porous interplanetary dust particles (IDPs), which are considered as cometary origin (usually considered

as preserver of building blocks of the solar system as well), have almost the chondritic chemical composition (Bradley, 1994a). They contain submicron-scale amorphous silicate grains, named glass with embedded metal and sulfide (GEMS), which considered as circumstellar origin. The glass parts of GEMS are not simple Mg-silicates but contain Fe, Ca and Al as well (Bradley, 1994b).

In this chapter, we synthesized a Fe-bearing amorphous silicate sample with the CI chondritic composition by a sol-gel method as circumstellar dust analogue, and carried out crystallization experiments by heating the sample under controlled redox conditions. The starting material was analyzed with IR spectroscopy, X-ray diffraction (XRD) and transmission electron microscopy (TEM). The heated samples were analyzed using IR, XRD and scanning electron microscopy (SEM) methods to discuss crystallization kinetics.

4.2 Experimental Procedure

4.2.1 Preparation of Starting Material

The system of the amorphous material which was used in this study is Na_2O-MgO-Al_2O_3-SiO_2-CaO-FeO-NiO with the CI chondritic composition. The starting material was synthesized by a sol-gel method. In the first step of the sol-gel method, magnesium ribbon, iron powder, aluminum powder, calcium carbonate powder, sodium carbonate powder and nickel powder were weighed as the CI chondritic ratio (Anders & Grevesse, 1989). Approximately 10% nitric acid was added to dissolve them. Tetraethyl orthosilicate (TEOS, $Si(OC_2H_5)_4$), which was weighed as the chondritic ratio, was mixed to the solution. Ethanol was added as same volume as the nitrate solution.

The solution was stirred by a stirrer magnet. And then, approximately 15% ammonia solution was added to the solution slowly when the solution was stirred. In a short while, the solution gelled by hydrolysis of TEOS. It was settled for about 2 days at room temperature until it gelled well. The obtained material was dried in air and roughly ground in an agate mortar. Finally the gel was heated at 400°C for 10 hours with a one-atmosphere gas-mixing furnace under the redox condition on the iron-wüstite buffer curve using H_2-CO_2 gas mixture in order not to be oxidized divalent iron to trivalent.

4.2.2 Heating Experiments

Using a one-atmosphere gas-mixing furnace, heating experiments were carried out to investigate the temperature and time dependence of crystallization of the starting material. The starting material was heated at various temperatures for a constant duration (at 660-1200°C for 0.5 hour) and heated at a constant temperature for various durations (at 680°C for 0.5-12 hours) (Table 4.1). To prevent oxidation of the Fe^{2+} cation, the oxygen partial pressure in the furnace was controlled on the iron-wüstite buffer curve using H_2-CO_2 gas mixture. The samples were cooled with the cooling rates ranging from 20 to 30 K/min. In such cooling rate, crystallization during cooling can be ignored compared with crystallization at high constant temperatures.

4.2.3 Characterization

The sample materials were analyzed by XRD, TEM, SEM and IR spectroscopy. For XRD analysis, the starting material and the run products of the heating experiments were mounted on a thin glass fiber of 5 μm in diameter with glycol phthalate as a glue. They were exposed to Mo K_α ra-

Table 4.1: Heating conditions.

	0.5 h	1 h	3 h	6 h	12 h
660°C	√				
680°C	√	√	√	√	√
690°C	√				
700°C	√				
720°C	√				
758°C	√				
1200°C	√				

diation (λ=0.710688 Å) and measured with an imaging plate diffractometer (Rigaku R-AXIS IV, Osaka University). In addition, they were exposed to synchrotron radiation (λ=2.1597 and 2.1599 Å) and measured with a Gandolfi camera at the beamline 3A in the Photon Factory Institute of Material Structure Science, High Energy Accelerator Research Organization (Nakamura et al., 2001).

For TEM observation, the starting material was embedded in epoxy resin and microtomed by Leitz-Reichert Super Nova ultramicrotome for TEM observation (JEOL JEM-2000FX II, Ibaraki University).

For SEM observation, the sample heated at 1200°C was embedded in epoxy resin and polished with diamond paste. Backscattered electron images and energy dispersive X-ray spectra of the sample were obtained with a scanning electron microscope (JSM-5510V, Osaka University) equipped with an energy dispersive X-ray analysis system (EX-23000BU).

For IR spectroscopic analysis, all samples were ground in an agate mortar for about 1 hour. An average diameter of the particles was less than 1 μm. These samples were dispersed and embedded in potassium bromide

for the mid-IR (1.4-25 μm) measurements and polyethylene for the far-IR (15-200 μm) measurements. IR absorption spectra were obtained with a Fourier transform IR spectrometer (Nicolet Nexus 670, Kyoto Pharmaceutical University). The measured wavenumber range and resolution were 7000-50 cm^{-1} (1.4-200 μm) and 1.0 cm^{-1}, respectively. The mass absorption coefficient, κ, was obtained from the equation

$$\kappa = S/M \ln(I_0/I), \tag{4.1}$$

where S is the cross section of the sample pellet, M is the mass of the sample in the sample pellet and I_0 and I are the transmittance of a blank and sample pellet, respectively.

4.3 Results

4.3.1 Starting Material

The XRD profile of the starting material shows a halo pattern around 12° in 2θ, which is due to amorphous materials (Fig. 4.1). There are also some small and broad peaks, which are identified as magnetite (Fe_3O_4) and ferrihydrite ($5Fe_2O_3 \cdot 9H_2O$). The broad features of the peaks indicate that the size of the crystallite is very small. A TEM image of the starting material shows very small fibrous crystals and globular crystals embedded in a matrix (Fig. 4.2). The image is consistent with the XRD result: the fibrous crystal is ferrihydrite, the globular crystal is magnetite, and the matrix is amorphous silicates. Ferrihydrite might be formed during aging of the gel under wet conditions. Some ferrihydrite might be transformed to magnetite during drying at 400°C.

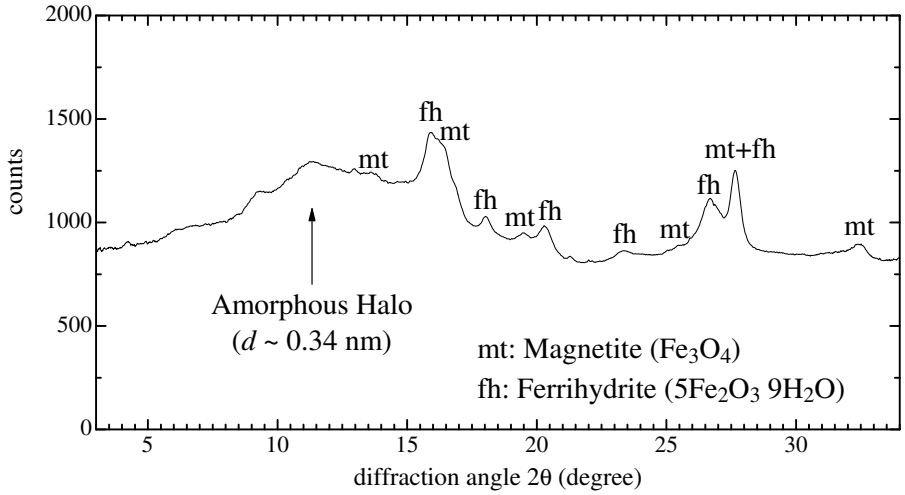

Figure 4.1: XRD pattern of the starting material. A diffuse halo attributed to amorphous silicates in the diffraction pattern is identified around 12°. Abbreviations: mt = magnetite; fh = ferrihydrite. Wavelength of X-ray was λ=0.710688 Å.

In contrast to the XRD and TEM analyses, broad and smooth absorption features were observed at approximately 10 and 20 μm in the IR spectrum of the starting material (Fig. 4.3). The 10 and 20 micron features are typical for amorphous silicates originated from Si-O stretching and O-Si-O bending vibrational modes, respectively. The 10 micron feature was located at 9.8 μm (FWHM = 1.8 μm) and mass absorption coefficient at the peak was 4260 cm^2/g. The 20 micron feature was located at 21.4 μm (FWHM = 11.0 μm) and mass absorption coefficient at the peak was 2710 cm^2/g. An IR spectrum of magnetite has an absorption peak at 18 μm (Keller et al., 2002) but we could not recognize any peaks for magnetite in this spectrum. Peaks of ferrihydrite (9 μm and 15-20 μm, Russell (1979)) could not be identified, either. Therefore we can conclude that the amounts of magnetite and ferrihydrite are much smaller than the amount of the amorphous silicate.

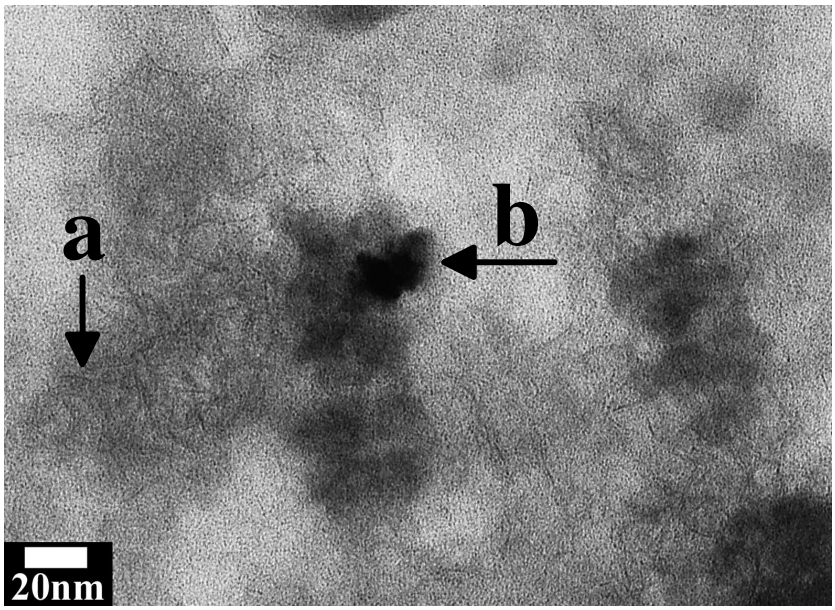

Figure 4.2: TEM image of amorphous silicate matrix, ferrihydrite fibers (arrow-a) and magnetite globules (arrow-b) of the starting material.

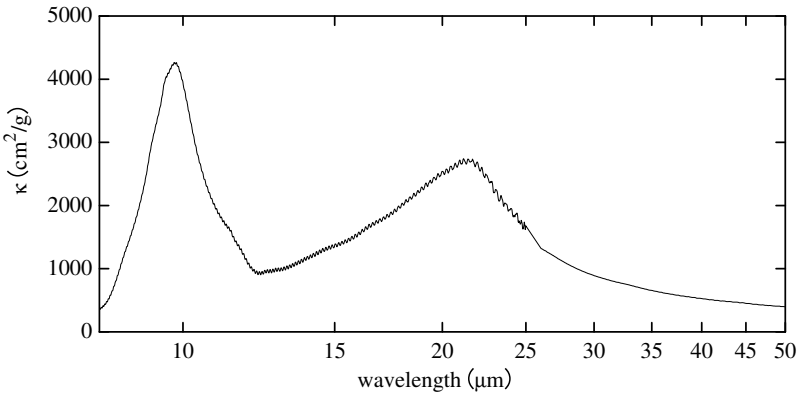

Figure 4.3: IR spectrum of the starting material. Broad absorption features due to amorphous silicates were observed at approximately 10 and 20 μm

4.3.2 Temperature Dependence of Crystallization

Mineral phases of the samples heated at different temperatures for a constant duration (0.5 hr) were examined by synchrotron radiation-XRD (Fig. 4.4). Olivine, magnesiowüstite ((Mg, Fe) O) and taenite ((Fe, Ni)) were recognized at 680°C for 0.5 hour. Magnesiowüstite and taenite were probably formed from magnetite and ferrihydrite by reduction. Olivine was crystallized from the amorphous silicate. By heating at higher temperature of 758°C, olivine, taenite and pyroxene crystallized. Pyroxene has orthorhombic or monoclinic unit cell symmetry. We can identified pyroxene in the sample at 1200°C as clinopyroxene but the XRD patterns of the others did not allow an clear identification of the polymorphs. Magnesiowüstite was reduced to taenite at this temperature.

A backscattered electron image, which indicates composition, of the sample heated at the highest temperature of 1200°C had three phases (Fig. 4.5), grains and very small bright particles embedded in a dark matrix, although we could not recognize any texture within a resolution limit of SEM observation for the samples heated at the lower temperatures. The texture of the run product at 1200°C shows partial melting at the high temperature, above solidus (about 780°C calculated by MELTS program). A typical energy dispersive X-ray analysis of the grain indicated olivine composition including magnesium, iron and silicon, while the spectrum of the matrix showed sodium, aluminum and calcium-rich composition, which olivine does not include. Considering the XRD result (Fig. 4.4), the grains were olivine formed by partial melting and recrystallization, and the dark matrix was the glass formed by partial melting and quenching. The small bright particles are taenite, which is consistent in the XRD study. The energy dispersive X-ray analysis could not reveal presence of pyroxene. It seemed from SEM

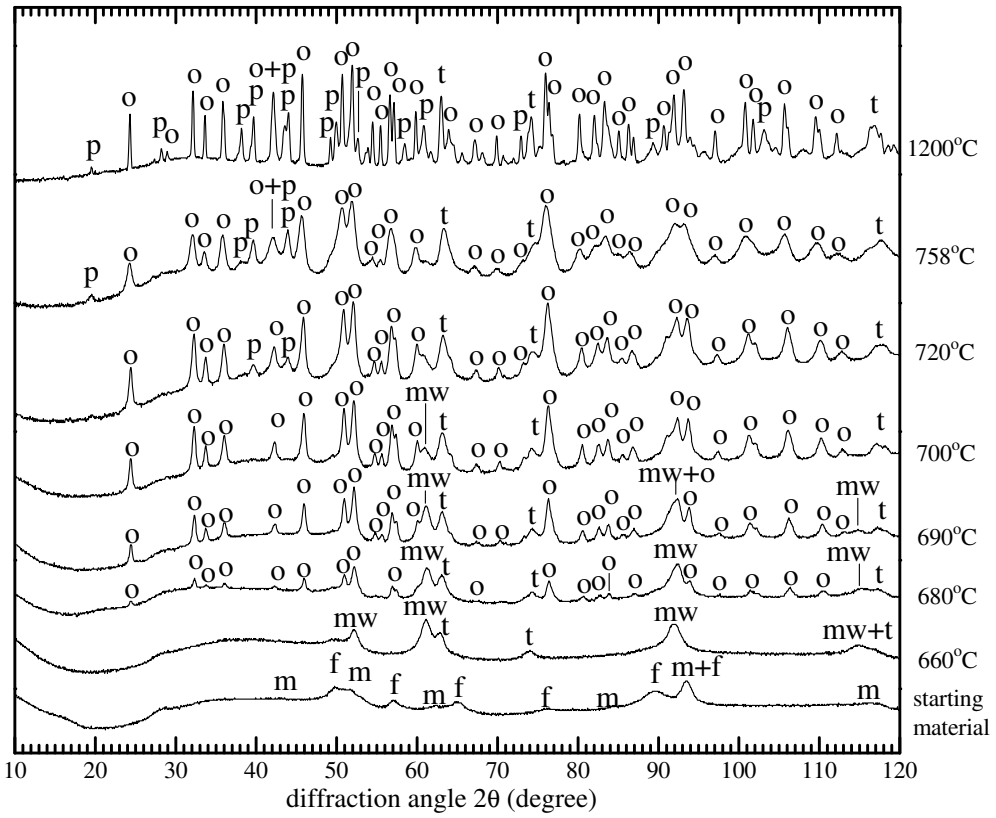

Figure 4.4: Synchrotron radiation-XRD patterns of the starting material and the samples heated at various temperatures for 0.5 hr. Abbreviations: o = olivine; p = pyroxene; t = taenite; mw = magnesiowüstite; m = magnetite; f = ferrihydrite. Wavelength of X-ray was λ=2.1597 Å for all the samples except the 1200°C sample and 2.1599 Å for the 1200°C sample.

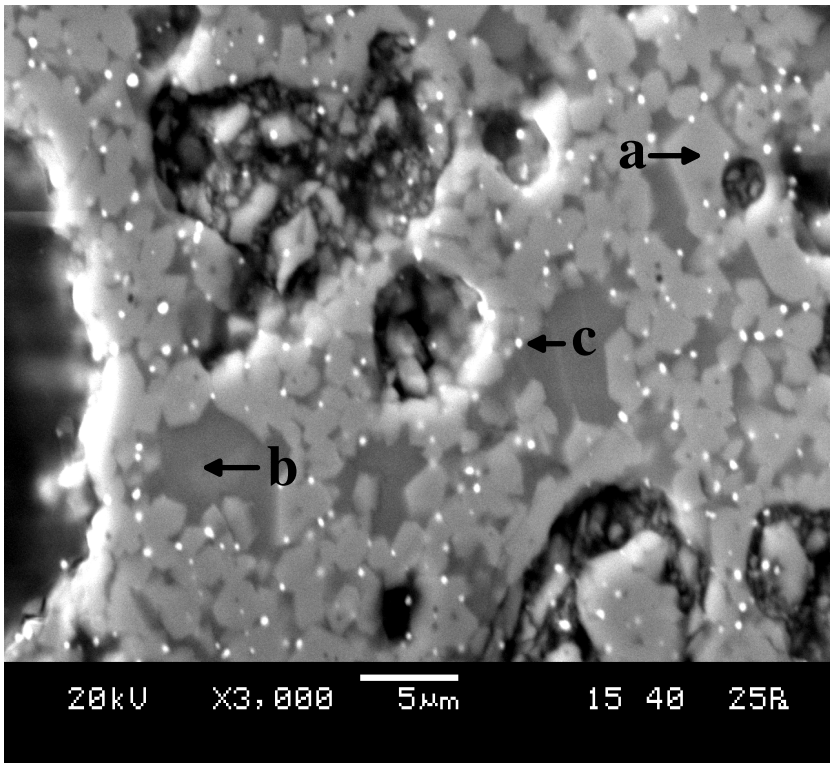

Figure 4.5: Backscattered electron image of the sample heated at 1200°C for 0.5 hour. Arrows of a, b and c indicate grains, a dark matrix and very small bright particles, respectively.

and XRD analyses that the amount and size of pyroxene was very small.

IR spectra of the samples heated at 660-1200°C for 0.5 h are shown in Fig. 4.6. Sharp and prominent absorption peaks were increased gradually from the broad amorphous features. Compared with IR spectra of olivine (Koike et al., 2003), these peaks (at 9.2, 10.0, 10.3, 10.6, 11.3, 11.9, 16.5, 18.6, 19.8, 22.3, 24.3, 28.3 and 35.1 μm, 1200°C) were identified as olivine. Most of the peaks shifted to longer wavelength with proceeding of crystallization (Table 4.2). Considering the previous studies of the compositional effect of solid solution on peaks in IR spectra (Koike et al., 2003), this peak shift

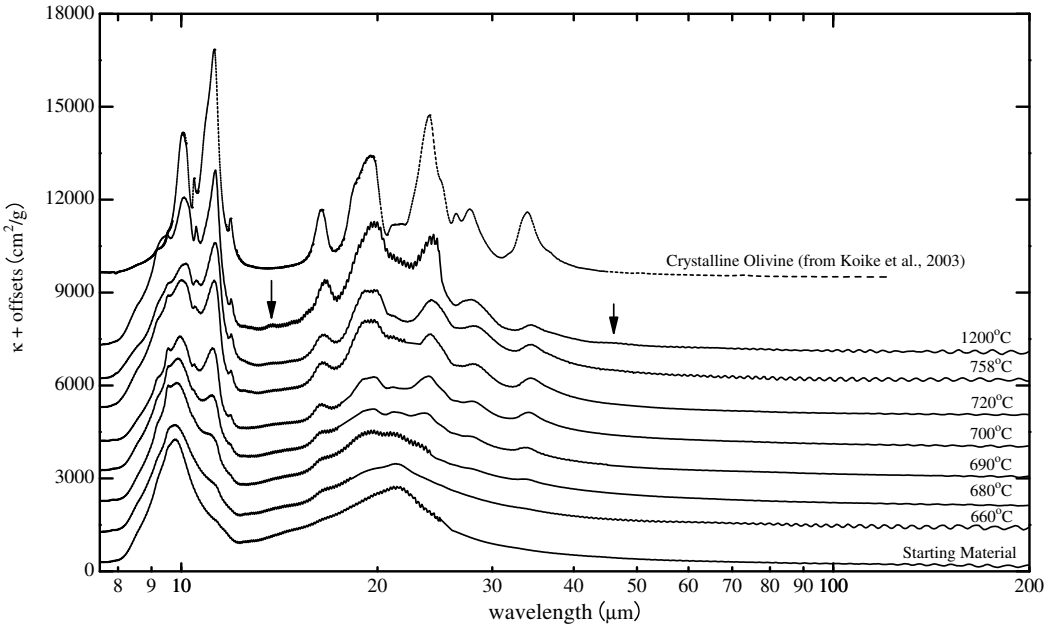

Figure 4.6: IR spectra of the samples heated at different temperatures for a constant duration (0.5 hour) together with the spectrum of crystalline olivine with the atomic Mg/(Mg+Fe) ratio of 0.907 from Koike et al. (2003). Arrows indicate weak shoulders of pyroxene.

indicates Fe-enrichment in olivine through crystallization process. From the comparison of peak positions between Koike et al. and this work, it was roughly estimated that Mg# (= the atomic Mg/(Mg+Fe) ratio) of the olivine changed from almost Mg-end member to 0.8.

We cannot recognize a peak around 18 μm for magnesiowüstite. Taenite has no IR active vibrational modes in the measured region. Two broad shoulders at 13.8 and 46.3 μm in the IR spectrum of 1200°C would be originated from pyroxene (arrows in Fig. 4.6). A large absorption peak at 9.5 μm was also detected in the spectrum of 1200°C. Fabian et al. (2000) reported that a peak attributed to amorphous silica is recognized at 9.5 μm after heating of amorphous Mg-silicates. This IR feature is consistent with the Si-rich

amorphous matrix (Fig. 4.5).

4.3.3 Time Dependence of Crystallization

The XRD patterns of the run products at 680°C show that olivine, magnesiowüstite and taenite were crystallized by heating for 0.5 hour (Fig. 4.7). The amount of olivine increased by heating and magnesiowüstite was reduced to taenite for longer heating duration (6 hours).

IR spectra of the samples heated at 680°C for 0.5-12 hours are shown in Fig. 4.8. Sharp peaks of olivine (9.2, 10.0, 10.2, 10.6, 11.3, 11.9, 16.4, 18.9, 19.9, 21.5, 23.8, 28.3 and 34.7 μm, 12 hours) grew gradually from initial broad features. Olivine peaks were barely seen in the 0.5-hour spectrum. After farther heating duration for 6 hours, crystallization was almost complete. Shift of peaks to longer wavelength due to change of a Mg/Fe ratio of olivine was also observed (Table 4.3). The Mg# of olivine was estimated very roughly by spectral peak positions as decreasing from 1 to 0.8. We cannot recognize a peak around 18 μm for magnesiowüstite, neither.

4.4 Discussion

4.4.1 Estimation of Degree of Crystallization

The spectral evolutions in this study (Fig. 4.8) suggest a gradual change of ratio of amorphous and crystalline silicates. Quantitative estimation of the degree of crystallization is necessary for precise analyses of the crystallization process of amorphous silicates. We assumed that a spectrum of an intermediate crystallized silicate can be represented by a linear combination of spectra of an amorphous silicate and a complete crystallized silicate. Thus,

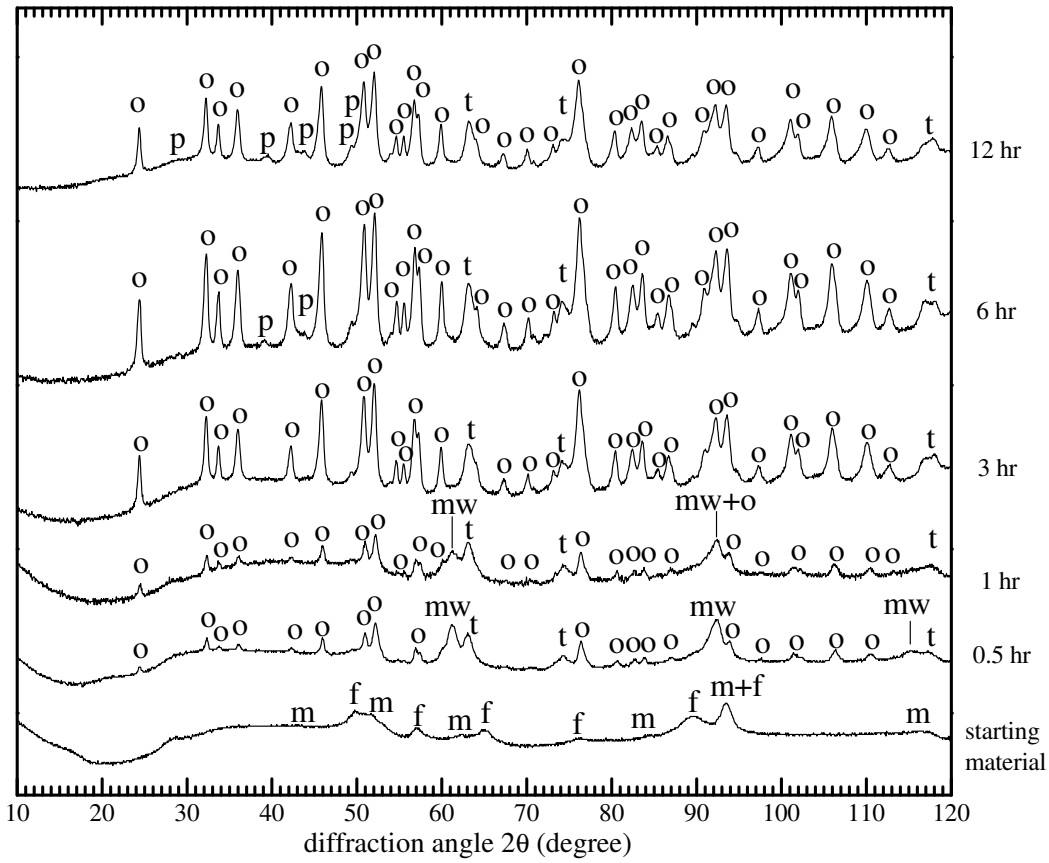

Figure 4.7: Synchrotron radiation-XRD patterns of the starting material and the samples heated at 680°C for various durations. Abbreviations: o = olivine; p = pyroxene; t = taenite; mw = magnesiowüstite; m = magnetite; f = ferrihydrite. Wavelength of X-ray was λ=2.1597 Å for all the samples except the 12 hr sample and 2.1599 Å for the 12 hr sample.

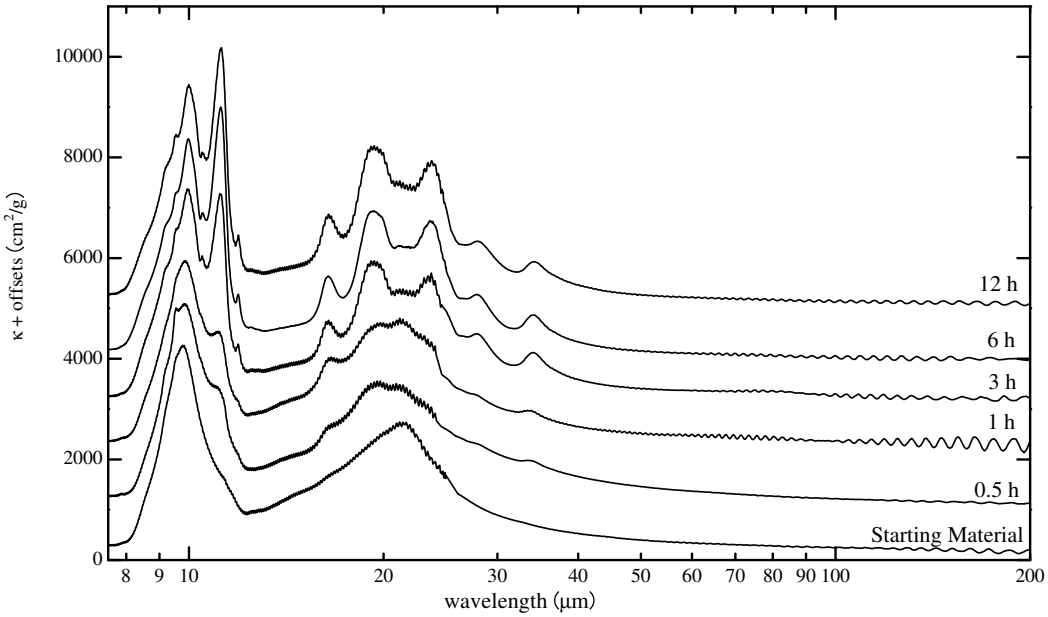

Figure 4.8: IR spectra of the samples heated at a constant temperature (680°C) for different durations.

the mass absorption coefficient of a partially crystallized silicate, κ, can be written as follows;

$$\kappa = (1 - C_{\rm IR})\,\kappa_{\rm as} + C_{\rm IR}\,\kappa_{\rm xt}, \tag{4.2}$$

where $\kappa_{\rm as}$ and $\kappa_{\rm xt}$ are the mass absorption coefficients of an amorphous silicate and a crystalline silicate (olivine), respectively, and $C_{\rm IR}$ is defined as the degree of crystallization determined by the IR measurement. Here, we ignored the presence of magnesiowüstite, taenite and pyroxene because their amounts are so small that their IR features were not detected. Such fitting with a linear combination of spectra for supposed materials is often performed to analyze observed astronomical spectra (e.g., Honda et al., 2003).

The IR spectra of the heated samples were fitted with eq. 4.2 by the least square method and the values of $C_{\rm IR}$ were obtained. In the present experiments, because of the multi-component system of the starting material,

Table 4.2: Peak positions in unit of μm of IR spectra of the starting material and the samples heated at various temperatures for a constant duration of 0.5 hour.

starting material	660°C	680°C	690°C	700°C	720°C	758°C	1200°C
		8.75	8.65	8.72	8.58	8.52	8.62
		9.18	9.20	9.20	9.18	9.20	9.21
		9.53	9.53	9.54	9.55	9.57	9.53
9.79	9.76	9.85	9.81	9.86	9.92	9.99	10.02
			10.12	10.13	10.19	10.24	10.26
			10.53	10.58	10.60	10.59	10.57
		10.98	11.05	11.03	11.08	11.09	10.94
	11.21	11.25	11.28	11.28	11.33	11.35	11.29
			11.89	11.91	11.94	11.96	11.94
	14.21	14.31	14.33				
	16.52	16.45	16.35	16.37	16.43	16.45	16.54
			19.02	19.26	18.97	18.98	18.60
	19.36	19.24	19.74	19.93	19.92	20.00	19.77
21.48	21.55	21.57	21.43	21.45	21.46	21.39	22.26
	22.71	23.34	23.76	23.96	24.29	24.29	24.26
		25.56					
			27.88	28.18	28.33	28.48	28.26
		34.27	33.93	34.58	35.03	35.01	35.06

Table 4.3: Peak positions in unit of μm of IR spectra of the starting material and the samples heated at a constant temperature of 680°C for various durations.

starting material	0.5 h	1 h	3 h	6 h	12 h
	8.75	8.66	8.61	8.58	8.57
	9.18	9.12	9.17	9.18	9.22
	9.53	9.58	9.55	9.55	9.54
9.79	9.85	9.98	9.95	9.98	9.98
			10.20	10.22	10.23
		10.49	10.55	10.56	10.59
	10.98	10.96	11.02	11.04	11.05
	11.25	11.25	11.26	11.27	11.29
		11.85	11.92	11.94	11.94
	14.31	14.33			
	16.45	16.45	16.40	16.42	16.43
			19.00	18.92	18.90
	19.24	19.27	19.90	19.86	19.86
21.48	21.57	21.73	21.34	21.47	21.52
	23.34	23.67	23.61	23.76	23.84
	25.56	27.56	28.04	28.12	28.32
	34.27	33.98	34.47	34.45	34.65
			75.76		

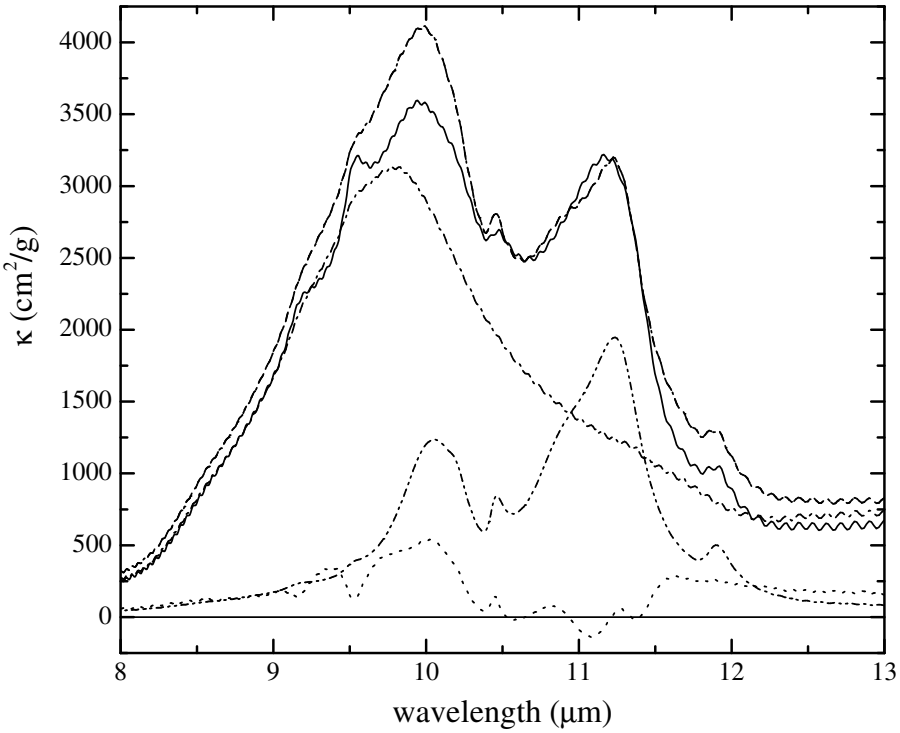

Figure 4.9: Fitting result of the sample heated at 700°C for 0.5 hour. The solid, dashed and dotted lines indicate the observed, fitted spectrum and their residue, respectively. The fitted spectrum is the sum of spectra of amorphous silicate (*dot-dashed*) and olivine with the atomic Mg/(Mg+Fe) ratio of 0.907 (*dot-dot-dashed*).

olivine crystallized from the amorphous silicate and the residual silicate might change their compositions during crystallization. However, we used $\kappa_{\rm xt}$ and $\kappa_{\rm as}$ as the spectrum of olivine with the Mg# of 0.907 (San Carlos, Koike et al. (2003)) and that of the starting material. The chemical composition of olivine does not affect the fitting results very much in the narrow range of the Mg#. Since the compositional change of the amorphous silicate affects the results especially in the fitting range around 10 μm, the fitting was made in the range from 10.6 to 11.7 μm, which includes the strongest peak of olivine.

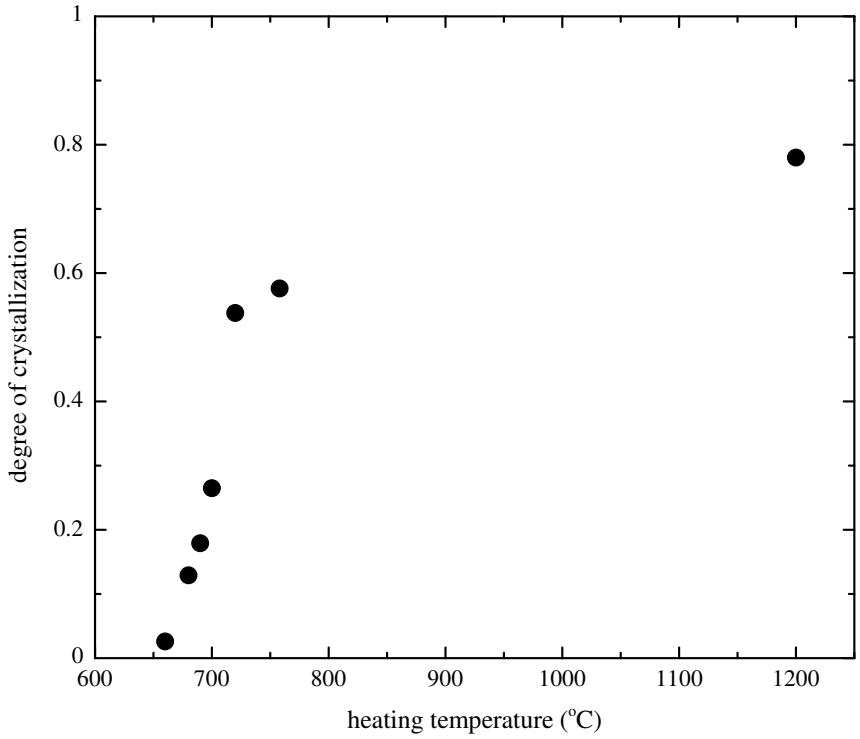

Figure 4.10: Degrees of crystallization estimated from the IR spectra, $C_{\rm IR}$, versus heating temperature for a constant heating duration (0.5 hour).

An example of the fitting results was shown in Fig. 4.9 (700°C-0.5 hour). The solid, dashed and dotted lines indicate the observed, fitted spectrum and their residue, respectively. From the fitting, we can obtain the degree of crystallization, $C_{\rm IR}$. There is a slight difference between the observed and the fitted spectra because the chemical compositions of both of olivine and the amorphous silicate change through the crystallization process.

The degree of crystallization at a series of heating temperatures and for a series of heating durations was plotted in Figs. 4.10 and 4.11, respectively. Some errors of the fitting are present due to the assumptions of the constant compositions of olivine and the amorphous silicate, and neglect of minor

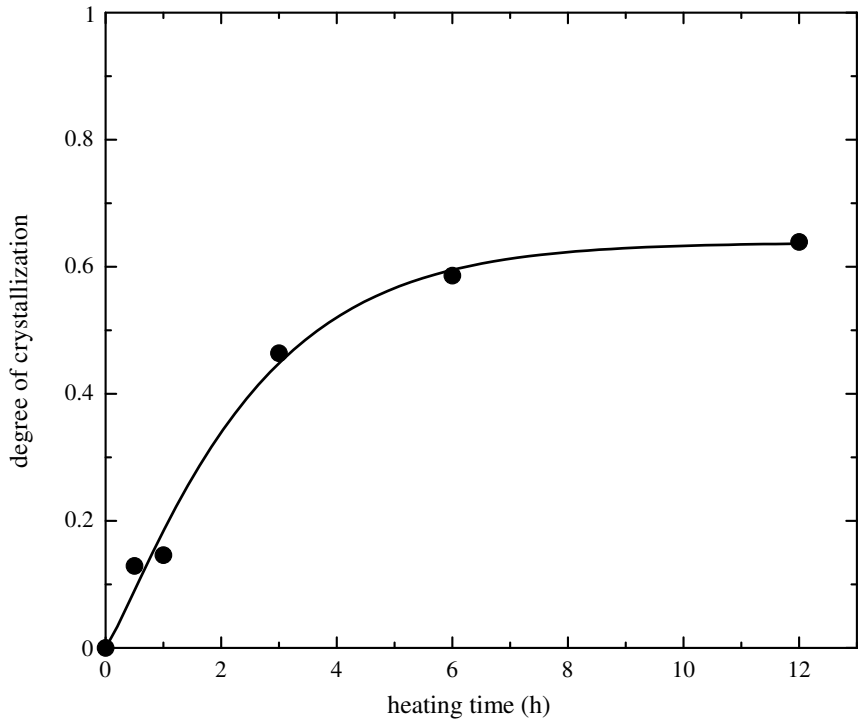

Figure 4.11: Degrees of crystallization estimated from the IR spectra, C_{IR}, versus heating time at a constant heating temperature (680°C). The solid line shows the best-fit curve by eq. 4.4.

phases (magnesiowüstite, taenite and pyroxene). From the fitting, we can discuss the crystallization process.

With increasing temperature for a constant heating duration, C_{IR} increases from 0 to approximately 0.8 (Fig. 4.10). At a constant temperature (680°C), C_{IR} increases with the heating duration and saturates at a constant value of approximately 0.65 (Fig. 4.11). These results indicate that complete crystallization did not occur and amorphous silicates were remained in the run products. At 1200°C where the temperature exceeds the solidus temperature (about 780°C), glass quenched from melt is present (Fig. 4.5). In case

of lower temperature heating below solidus, Al, Ca and Na-bearing phases, such as plagioclase and/or nepheline, should be present by complete crystallization. Since crystallization of these phases should be much slower than Mg, Fe, Si-rich phases, the run products in the present experiments can be regarded as olivine, minor crystalline materials and the metastable residual amorphous silicates.

4.4.2 Formulation of Crystallization Process

We can formulate time evolution of the degree of crystallization (Fig. 4.11) using the Johnson-Mehl-Avrami (JMA) equation (Avrami, 1939; Johnson & Mehl, 1939) for kinetics of transformation processes;

$$X = 1 - \exp\{-(t/\tau)^n\}, \tag{4.3}$$

where X is the transform fraction, τ is the time constant of the transformation and n is a kinetic parameter which depends on crystallization kinetics. We modified eq. 4.3 for the present study as follows:

$$C_{\rm IR} = C_\infty \left[1 - \exp\{-(t/\tau)^n\}\right] \tag{4.4}$$

where C_∞ is a constant corresponding to $C_{\rm IR}$ at infinity of time. This upper limit of saturated growth should correspond to the final metastable state of the heated samples including olivine and the amorphous silicate.

The solid line (Fig. 4.11) indicates the best-fit curve by the χ^2 method using eq. 4.4 with the parameters of n, τ and C_∞ of 1.16 ± 0.17, 9140 ± 1300 s and 0.638 ± 0.033, respectively (the coefficient of determination was 0.991).

According to Burke (1965), the JMA equation with $n = 1.5$ was derived from a theoretical crystallization models of 3-dimensional diffusion-controlled growth from a state that a number of nuclei is constant, or 1-dimensional diffusion-controlled growth with a constant nucleation rate. On

the other hand, a model of the JMA equation with $n = 2.5$ was obtained by 3-dimensional diffusion-controlled growth with a constant nucleation rate. 3-dimensional crystal growth is probably suitable for crystallization of olivine. The value of n ($\sim$1.2) obtained from the present experiments is consistent with the theoretical crystallization model of 3-dimensional diffusion-controlled growth from a state of a constant number of nuclei ($n = 1.5$). Moreover, a state which nuclei number is constant represents that the starting material contains tiny crystallites such as magnetite and ferrihydrite as nucleation sites of olivine crystals. Thus, the crystallization of olivine in this work occurs by heterogeneous nucleation on tiny crystallites already present in the starting material.

As a preliminary investigation, the temperature dependence of τ was estimated with eq. 4.4 using C_{IR} of the samples heated at the different temperatures. We assumed C_∞ as the same values of the heating at 680°C, although these values probably depend on temperature. We also assume n as 1.5. Since crystallization kinetics of the partially melted sample (1200°C) was different from that of the other samples, that sample was neglected in this analyses. The sample heated at 758°C was also neglected, since the pyroxene crystallization was proceeded as well as the olivine crystallization (Fig. 4.4). The temperature dependence of τ was fitted by the Arrhenius equation;

$$1/\tau = \nu_0 \exp(-E_{\mathrm{a}}/k_{\mathrm{B}}T) \tag{4.5}$$

where, ν_0 is a frequency factor, E_{a} is the activation energy of crystallization, k_{B} is the Boltzmann constant and T is the absolute temperature. As the results, ln (ν_0) and $E_{\mathrm{a}}/k_{\mathrm{B}}$ were calculated to be 52, where ν_0 is in s^{-1}, and 6×10^4 K, respectively (Fig. 4.12). Because time evolution of C_{IR} at different temperatures was not obtained in the present experiment, these values are

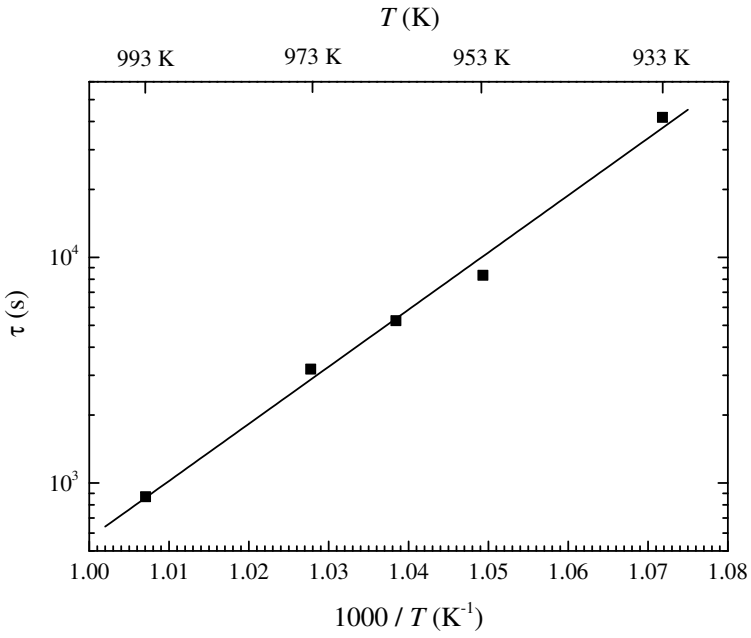

Figure 4.12: The Arrhenius plot of τ vs. T^{-1} over the temperature range 660-720°C.

not accurate well and some deviations should be present by the extrapolation of the JMA equation to higher or lower temperatures. If a more precise value of $E_{\rm a}$ is obtained by more detailed experiments, as well as chapter 2, we will discuss time evolution of $C_{\rm IR}$ of circumstellar silicates at temperatures lower than those in the laboratory.

4.4.3 Implication for Spectral "Stall"

Hallenbeck et al. (1998) carried out the related crystallization experiments using smoke in the past. They reported that there was no IR spectral change between 10.5 and 48 hours of the heating at 1027 K, which was named a "stall" phase. In our experiment, however, crystalline peaks gradually increased and the "stall" spectrum did not appear (Fig. 4.11). Thompson &

Tang (2001) suggested that the "stall" time was required when tetrahedral SiO_4 units were reformed in amorphous phase to increase the number of non-bridging oxygen atoms. Kamitsuji et al. (2005) performed crystallization experiments of Mg-silicate grains. They also insist on pre-nucleation structural change of Mg-silicate before crystallization by a direct TEM observation study. These processes should correspond to a nucleation delay in the early stage of crystallization. If a transformation starts by nucleation and is followed by diffusion-controlled growth, the degree of crystallization-time curve is a sigmoidal shape, which is typically represented by the JMA equation with n of 2.5 (Fig. 2.10 in chapter 2).

However, in the experiment of Hallenbeck et al. (1998), there were two processes in the spectral evolution. Crystallization started from the beginning to 10.5 hours of the heating, and, after the "stall" phase, crystallization proceeded again. Rietmeijer et al. (2002) observed their starting material under TEM and found that it was heterogeneous and contained tiny crystals of tridymite, periclase and forsterite. Therefore, from a view point of our discussion with the JMA equation, the two-step crystallization phenomena such as "stall" should be regarded as combination of crystal growth on pre-existing nuclei in the starting material, and a new crystallization process by nucleation of a new phase and its crystal growth. Because diffusion at temperatures in the experiments of Hallenbeck et al. (1027 K) is so slow that only a limited amount of crystals can grow near the pre-existing nuclei, further nucleation should be required in regions far from the nuclei. In the present experiments, the starting material contained Fe. Since diffusion of Fe cation occurs faster than that of Mg cation (e.g., Kress & Ghiorso, 1995), it is considered that crystal growth of olivine could proceed continuously and the "stall" phase could not be observed.

4.4.4 Implication for Crystallization Nature of Circumstellar Silicate Dust

Our experimental results and the comparison with the previous studies indicate clearly that properties of precursor materials of crystalline silicates strongly influence their crystallization processes. The interstellar silicates, which are considered to be precursor materials for circumstellar crystalline silicates of young stars, are considered as amorphous based on the IR observation (e.g., Kemper et al., 2004). However, although the starting materials of both Hallenbeck et al. (1998) and ours (Fig. 4.3) contained tiny crystallites as nucleation sites, their IR spectra did not show crystalline features but amorphous features. This fact suggests that the IR observations cannot detect existence of any crystallites in amorphous silicates.

Figure 4.13 is a schematic of crystallization processes for various properties of starting materials. If circumstellar amorphous silicates do not at all contain crystallites before a heating event, crystallization includes nucleation and crystal growth, and can be represented by the JMA equation with n of 2.5 (Type-C in Fig. 4.13). In fact, the crystallization of the Mg amorphous silicate synthesized by us, including nucleation and crystal growth, showed Type-C process (chapter 2). If circumstellar amorphous silicates have some crystallites such as the Mg-pure and Fe-free silicate smoke of Hallenbeck et al. and the FeO-bearing starting material as this study, nucleation is not needed initially. As discussed in the previous section, crystallization behavior with some crystallites probably depends on the existence of Fe cation in the precursor amorphous material. The other cations such as Al, Na, Ca and Ni might not affect the process very much because olivine does not include these cations and they are in minor abundances. FeO-bearing amorphous silicates might crystallize as predicted by the JMA equation with n of 1.5

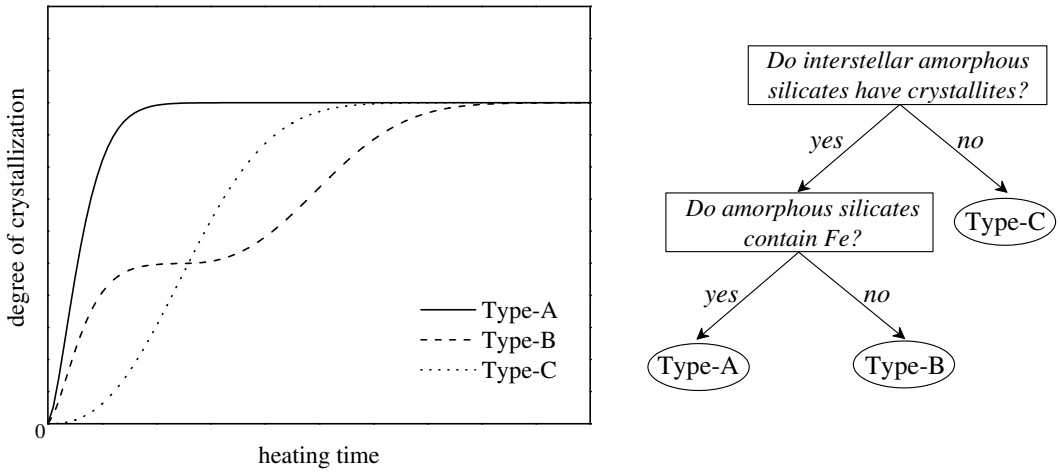

Figure 4.13: Schematic of time evolution of crystallization for amorphous silicates in circumstellar environment of young stars at a constant temperature. Type-A curve represents crystallization process with diffusion-controlled crystal growth from pre-existing nuclei ($n = 1.5$ in eq. 4.4). Type-B curve represents crystallization process with a combination of diffusion-controlled crystal growth from pre-existing nuclei and new crystallization process by nucleation and diffusion-controlled crystal growth, which includes a "stall" phase. Type-C curve represents crystallization process with nucleation and diffusion-controlled crystal growth ($n = 2.5$ in eq. 4.4).

(Type-A in Fig. 4.13) such as the present experiment and the experiment in the next chapter, whereas Fe-free amorphous silicates might show "stall" during their crystallization (Type-B in Fig. 4.13) such as the Hallenbeck et al. (1998).

4.5 Conclusions

We synthesized an FeO-bearing amorphous silicate with the chondritic composition as analogue of circumstellar silicate dust. Heating experiments were carried out at 660-1200°C for 0.5-12 hours to examine crystallization of the amorphous silicate. Olivine was mainly crystallized from the starting material. The observed IR peak positions suggested that the Mg# of the olivine decreased from 1 to 0.8 through crystallization.

We estimated the degree of crystallization of the heating samples quantitatively based on fitting of their IR spectra near 11.2 μm by use of individual spectra of olivine with the Mg/(Mg+Fe) ratio of 0.907 and the amorphous silicate. Time evolution of the crystallization could be formulated by the Johnson-Mehl-Avrami equation with the power of about 1.2, which is consistent with a theoretical crystallization model of 3-dimensional diffusion-controlled growth from a state of a constant number of nuclei. The constant number of the nuclei corresponds that the starting material contains crystallites such as magnetite and ferrihydrite as nucleation sites of olivine crystals.

From the quantitative analyses, we suggest that crystallization processes in circumstellar regions should depend on properties of the interstellar amorphous silicates such as the existence of crystallites and/or Fe-content. We proposed a model of crystallization processes for various initial properties of circumstellar silicates of young stars (Fig. 4.13).

Bibliography

Anders, E., & Grevesse, N. 1989, Geochim. Cosmochim. Acta, 53, 197

Avrami, M. 1939, J. Chem. Phys., 7, 1103

Burke, J. 1965, The Kinetics of Phase Transformation in Metals (England: Pergamon Press Limited)

Bradley, J. P. 1994a, Science, 265, 925

Bradley, J. P. 1994b, Geochim. Cosmochim. Acta, 58, 2123

Fabian, D., Jäger, C., Henning, Th., Dorschner, J., & Mutschke, H. 2000, A&A, 364, 282

Hallenbeck, S. L., Nuth III, A. J., & Daukantas, P. L. 1998, Icarus, 131, 198

Hanner, M. S., Lynch, D. K., & Russell, R. W. 1994, ApJ, 425, 274

Honda, M., Kataza, H., Okamoto, Y. K., et al. 2003, ApJ, 585, L59

Johnson, W. A., & Mehl, R. F. 1939, Trans. Am. Inst. Min. Metal Eng., 135, 416

Kamitsuji, K., Sato, T., Suzuki, H., & Kaito, C. 2005, A&A, 436, 165

Keller, L. P., Hony, S., Bradley, J. P., et al. 2002, Nature, 417, 148

Kemper, F., Vriend, W. J., & Tielens, A. G. G. M. 2004, ApJ, 609, 826

Koike, C., Chihara, H., Tsuchiyama, A., Suto, H., Sogawa, H., & Okuda, H. 2003, A&A, 399, 1101

Kress, V. C., & Ghiorso, M. S. 1995, Geochim. Cosmochim. Acta, 59, 313

Malfait, K., Waelkens, C., Waters, L. B. F. M., et al. 1998, A&A, 332, L25

Nakamura, T., Noguchi, T., Yada, T., Nakamuta, Y., & Takaoka, N. 2001 Geochim. Cosmochim. Acta, 65, 4385

Rietmeijer, F. J. M., Hallenbeck, S. L., Nuth III, J. A., & Karner, J. M. 2002, Icarus, 156, 269

Russell, J. D. 1979, Clay Miner., 14, 109

Thompson, S. P., & Tang, C. C. 2001, A&A, 368, 721

Chapter 5

Mg/Fe Fractionation Involved in Crystallization of Fe-bearing Silicate

IR observations of young and evolved stars show that only Mg-rich crystalline silicates exist in circumstellar regions, and Fe, one of the most important dust-forming elements, is extremely depleted. Here we show the first experimental evidence that Fe-depleted olivine [$(Mg, Fe)_2SiO_4$] can be formed by crystallization via thermal heating of FeO-bearing amorphous silicates. This chapter is a modified version of the paper as Murata et al., 2009, ApJ, 696, 1612.

5.1 Introduction

ISO revealed that crystalline silicates (e.g., olivine $[(\mathrm{Mg, Fe})_2\mathrm{SiO}_4]$, pyroxene $[(\mathrm{Mg, Fe})\mathrm{SiO}_3]$) are present in circumstellar environments around oxygen-rich young and evolved stars and comets (Waters et al., 1996; Waelkens et al., 1996; Molster et al., 1999; Crovisier et al., 1997), whereas interstellar

silicate dust is almost completely amorphous (Kemper et al., 2004). It is thought that crystalline silicates form by thermal annealing of amorphous silicates. Using high quality astronomical spectra, the circumstellar crystalline silicates are determined to be highly Mg-rich and Fe-poor (Mg# = atomic Mg/(Mg+Fe) ratio > 0.9 (Tielens et al., 1998)). This composition of circumstellar crystalline silicates differs fundamentally from the primitive extraterrestrial materials in our solar system such as chondritic meteorites and interplanetary dust particles (Brearley & Jones, 1989; Rietmeijer, 1989). Although iron, along with magnesium and silicon, is the major dust-forming element, concerning the solar abundance of elements (Anders & Grevesse, 1989), the observations show that only Mg-rich crystalline silicates exist in circumstellar regions. This fact produces one of the biggest unsolved mysteries since the first detection of crystalline silicates by ISO: Why do circumstellar crystalline silicates contain only magnesium and what is the major Fe-carrying phase? The clue to solving these questions is in the fact that the iron content of dust is closely connected to dusty material evolutions, which changes thermal properties, such as crystallization, melting, and condensation temperatures, and optical properties, such as absorption efficiency (Tielens et al., 1998; Dorschner et al., 1995).

Iron sulfides are candidates for an alternative Fe-carrier. In the spectra of some young stars, there is a band emission at $23.5\,\mu$m, which is expected to be attributed to iron sulfide grains (Keller et al., 2002). However, the solar abundance of sulfur is about half that of iron (S/Fe = 0.5/0.9), and the other half of iron cannot form iron sulfides. The second candidate for an Fe-carrying material is metallic iron. However, it has no IR-active vibrational modes, and we therefore cannot obtain any direct evidences from observations. In contrast to these materials, amorphous silicates are ubiquitous and

abundant in both circumstellar and interstellar space. Although it is difficult to determine the detailed composition of amorphous silicates because of their broad emission features, laboratory data of Fe-bearing amorphous silicates are well fitted to the astronomical spectra (e.g., Molster et al., 1999; Kemper et al., 2004; Dorschner et al., 1995; van Boekel et al., 2005). Therefore, it is a promising candidate as an iron carrier. However, the difference in chemical composition between coexisting Mg-rich crystalline and Fe-bearing amorphous phases looks paradoxical. To confirm whether Mg/Fe distribution occurs between crystalline and amorphous phases, we need to perform laboratory simulations of crystallization of Fe-bearing amorphous silicates under a subsolidus condition, because thermodynamics cannot predict Mg/Fe distribution even under metastable conditions at low temperatures (appendix A). Some interesting heating experiments have been performed using amorphous magnesium silicates. However, no experiment has been devised to investigate Mg/Fe distribution during crystallization using amorphous magnesium iron silicates.

5.2 Experimental Procedure

We heated synthetic amorphous silicate to investigate the chemical composition of silicates crystallized from the amorphous state. The MgO-FeO-SiO_2 system was chosen for its simplicity. The amorphous silicate was synthesized by the sol-gel method (Mg/Si ratio of the starting material is equal to the solar composition of 1.07 (Anders & Grevesse, 1989)). We assume that all sulfur formed iron sulfide grains and the Fe content of the amorphous silicate was reduced by the solar composition of sulfur as FeS (Fe/Si = 0.39). Note that the estimation of the Mg/Fe ratio of amorphous silicates

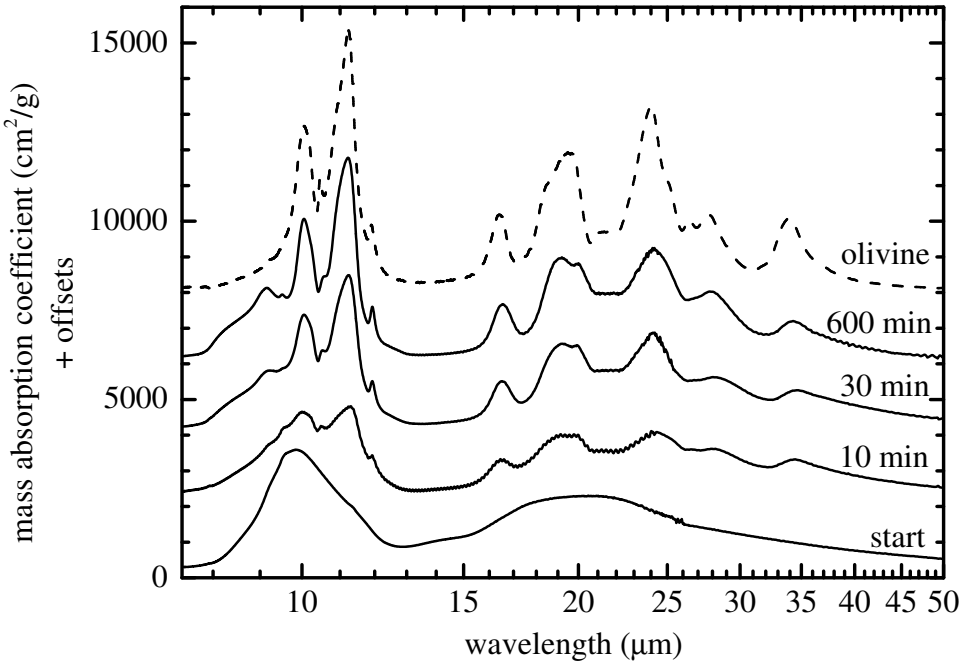

Figure 5.1: IR spectra of the starting material and the samples heated at 700°C for different durations (10, 30, and 600 min) together with the spectrum of olivine (Fo_{91} from San Carlos, Arizona, USA (Koike et al., 2003)). The broad 10- and 20-μm features of the starting material are typical for amorphous silicates and originate from Si-O stretching and O-Si-O bending vibrational modes, respectively. The sharp and prominent absorption peaks of crystalline olivine grew gradually from the initial broad features.

from IR spectroscopic observation is close to impossible. The FeO content of amorphous silicates decreases when part of the iron exists as a metal phase.

The starting amorphous material was heated at 700°C in a one-atmosphere gas-mixing furnace for various durations (10, 30, 60, 120, 360, and 600 min). To prevent oxidation of the Fe^{2+} cation, the oxygen partial pressure in the furnace was controlled (0.5 log units above the Fe-FeO buffer). We performed IR absorption spectroscopy (Nicolet Nexus 670) to estimate the degree of

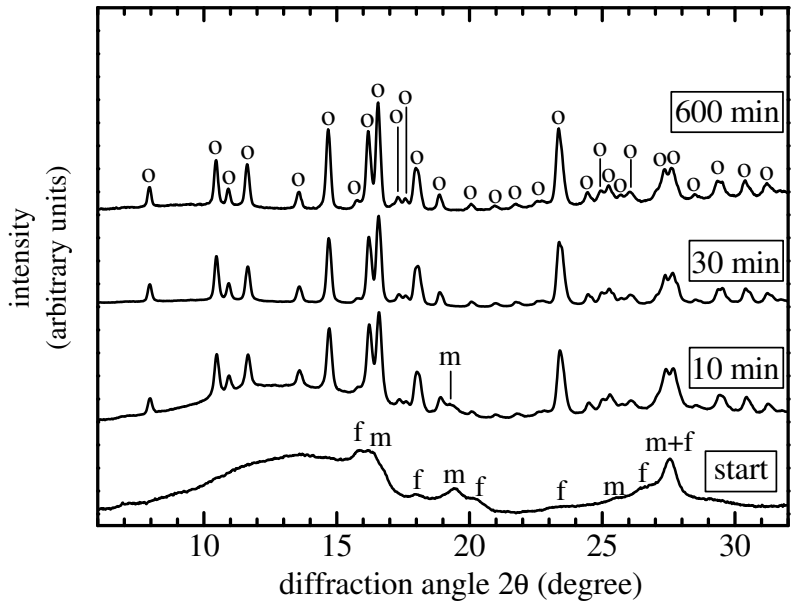

Figure 5.2: X-ray powder diffraction patterns of the starting material and the samples heated at 700°C for different durations (10, 30, and 600 min). The starting material shows a halo pattern due to amorphous materials around 14° in 2θ. The sharp peaks of the heated samples represent olivine (o) crystallized from the amorphous silicate. Some small and broad peaks are also present in the patterns of the starting material, which are identified as magnetite (m) and ferrihydrite (f).

crystallization. The degree of crystallization of the heated samples was estimated quantitatively by fitting the IR spectra (Murata et al., 2007). We also performed X-ray powder diffraction (Rigaku R-AXIS IV) to estimate the Mg# of crystallized olivine, based on the d-spacings (Brown, 1982). Details are described in the previous chapters 2 and 4.

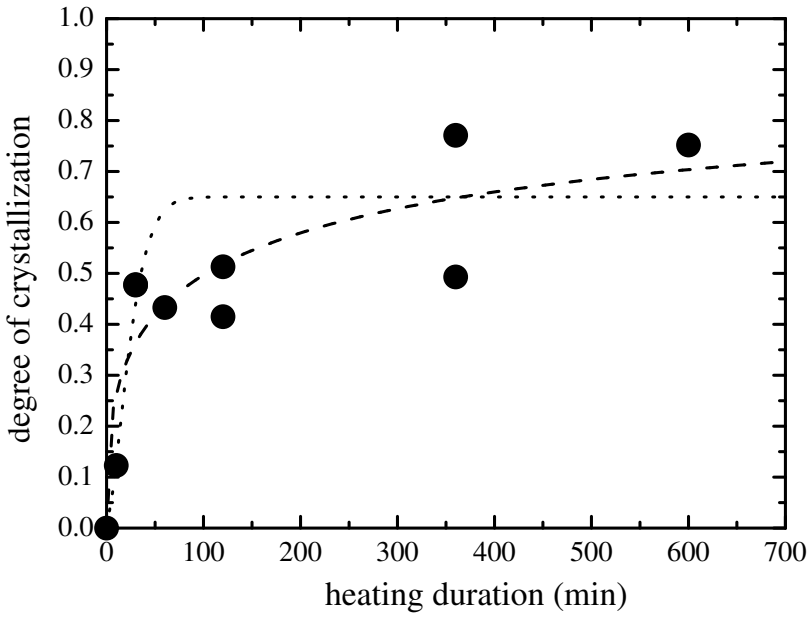

Figure 5.3: Degree of crystallization versus heating duration at 700°C. The degree of crystallization was estimated by IR spectral fit (Murata et al., 2007) using individual spectra of olivine (San Carlos (Koike et al., 2003)) and the starting material. The crystallization curve (*dashed line*) is fitted by the Johnson-Mehl-Avrami equation (eq. 4.4) with the values of C_∞, n and τ are 0.88, 0.37 and 9700 s, respectively. The dotted line shows a fitting result by the Johnson-Mehl-Avrami equation with a constant value of n of 1.5.

5.3 Results & Discussion

Figures 5.1 and 5.2 show typical IR spectra and XRD patterns respectively of the starting material and the heated samples. The starting material has a chemical composition between olivine and pyroxene ((Mg+Fe)/Si = 1.46), but only olivine crystallized in the experiments. The degree of crystallization increased as the duration of heating increased, and finally saturated at about 0.8 (Fig. 5.3). The amorphous silicates coexisted metastably

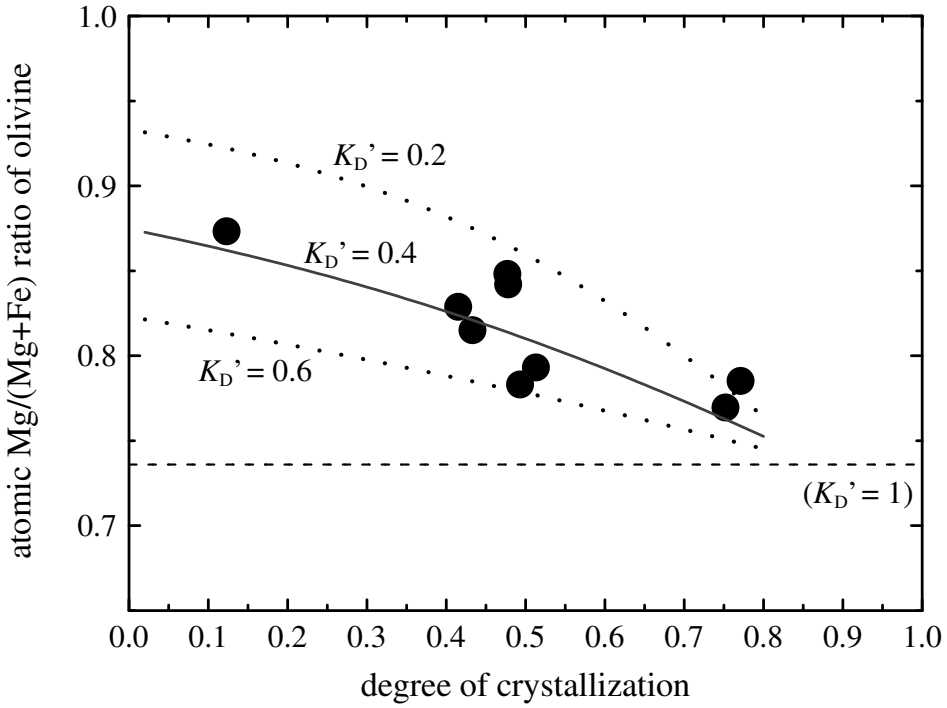

Figure 5.4: Compositional evolution of crystalline olivine through the crystallization process. The dashed line indicates an atomic Mg/(Mg+Fe) ratio of the starting material equal to 0.736. The solid line indicates an Mg/Fe distribution curve assuming the effective distribution coefficient of K'_D = $(\mathrm{Mg/Fe})_{amorphous\,silicate}$ / $(\mathrm{Mg/Fe})_{olivine}$ = 0.4. The dotted lines indicate Mg/Fe distribution curve assuming K'_D = 0.2 and 0.6.

with olivine when the crystallization was saturated (Fig. 5.3) without crystallization of pyroxene and plagioclase. The olivine peaks shifted to longer wavelength (Fig. 5.1), indicating an increase of the iron content (Koike et al., 2003) through the crystallization process. XRD of the starting material shows minor amounts of magnetite (Fe_3O_4) and ferrihydrite ($5Fe_2O_3 \cdot 9H_2O$) (Fig. 5.2); however, they are not identified in the IR spectra (Fig. 5.1). Their diffraction peaks almost disappeared after 10 min of heating. These phases

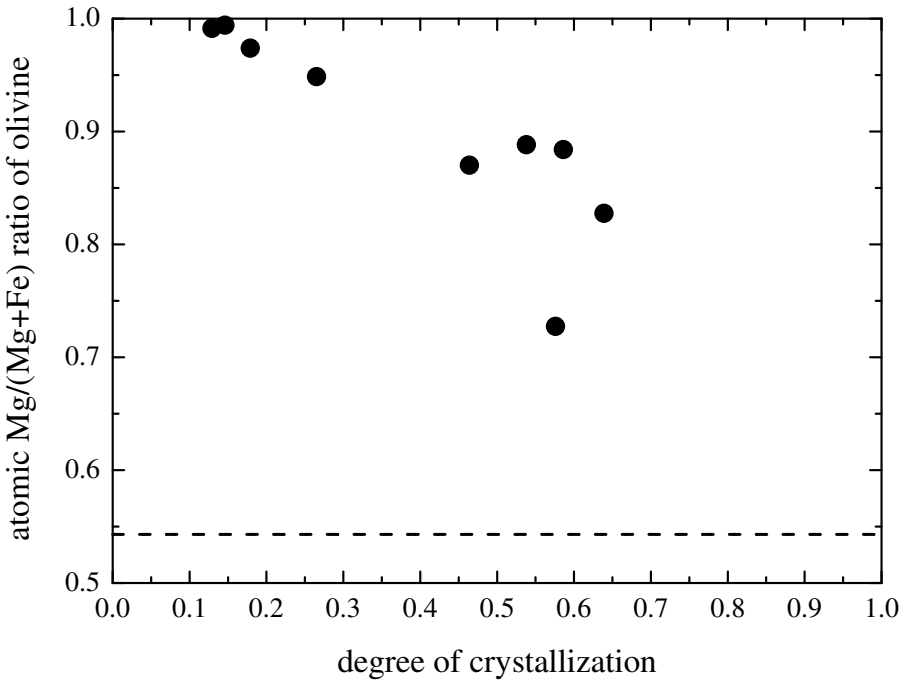

Figure 5.5: Compositional evolution of crystalline olivine during crystallization of the samples in chapter 4. The dashed line indicates an atomic Mg/(Mg+Fe) ratio of the starting material equal to 0.543.

reacted with amorphous silicate to form olivine, or dissolved into amorphous silicates in the early stage of crystallization, and were negligible for further discussion.

Figure 5.4 shows the relationship between Mg#s of olivine and degrees of crystallization. In the early stages of crystallization, the composition of crystallized olivine is considerably richer in magnesium than that of the starting material. The Mg# of olivine gradually decreases as crystallization proceeds from 0.87 to 0.77. Even when metastable equilibrium was reached between olivine and amorphous silicate at a degree of crystallization of about 0.8 (Fig. 5.3), the Mg# of olivine was higher than that of the starting material.

In chapter 4, Mg-rich olivine was crystallized from the amorphous silicate

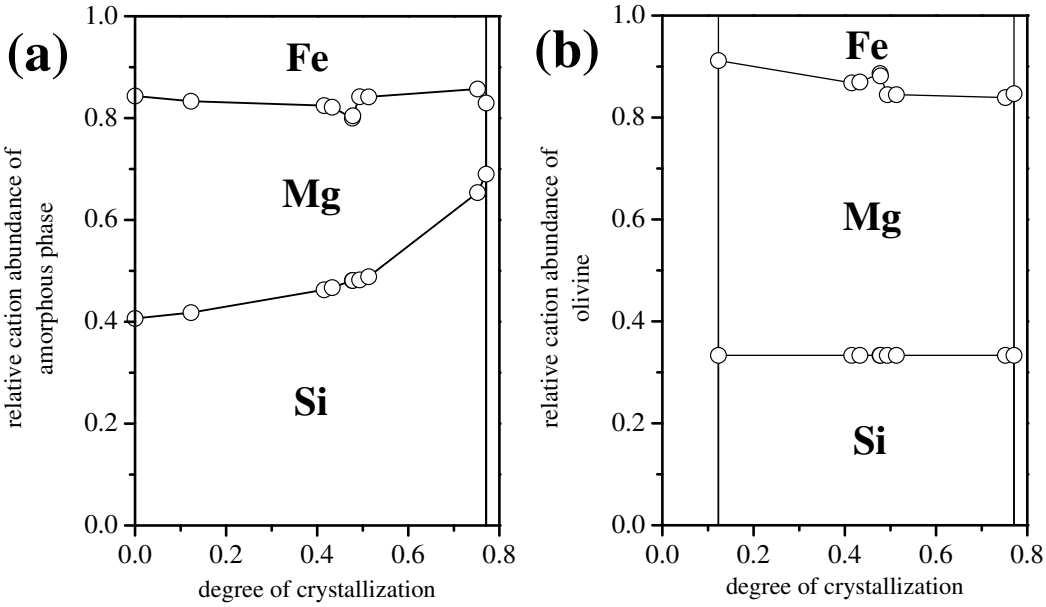

Figure 5.6: Cation fractions of (a) amorphous silicate and (b) crystalline olivine versus the degree of crystallization. The fractions of the amorphous silicate in the heated samples were calculated using the initial elemental ratio of the starting material, mass fraction of olivine in the heated samples derived from the IR spectra and the Mg/(Mg+Fe) ratio of the olivine derived from the X-ray diffraction patterns.

which has a composition richer in Fe than that in this chapter. Figure 5.5 shows that the compositions of crystallized olivine in chapter 4 was also considerably richer in magnesium than that of the starting material. This result suggested that Mg-rich olivine crystallization may occur under various temperatures (660-758°C). Note that a not negligible amount of metallic iron coexisted in these samples so that it is close to impossible to discuss the quantitative composition.

From the Mg# of olivine and the degree of crystallization in the MgO-FeO-SiO_2 system, we can obtain the evolution of the chemical composition

of both crystalline and amorphous silicate during crystallization (Fig. 5.6). Because olivine with an (Mg+Fe)/Si ratio of 2 was crystallized from the relatively Si-rich starting material with an (Mg+Fe)/Si ratio of 1.46, the SiO_2 content of the amorphous phase increased as crystallization proceeded. The Fe/Mg ratio of the amorphous phase also clearly increased by crystallization because magnesium cations distributed to the crystalline phase preferentially. The mixture of Fe-enriched amorphous silicate and Mg-rich olivine obtained in this experiment is consistent with astronomical observations; the IR spectra of circumstellar dust is well fitted by the Fe-rich amorphous silicates of Mg/Fe = 1 (Molster et al., 1999; Kemper et al., 2004; Dorschner et al., 1995; van Boekel et al., 2005).

It has been known that the distribution coefficient of Mg/Fe between olivine and the melt, K_D = $(\mathrm{Mg/Fe})_{melt}$ / $(\mathrm{Mg/Fe})_{olivine}$, is about 0.3 over a wide range of magmatic compositions at high temperatures (1150-1300°C) (Roeder & Emslie, 1970). Distribution coefficients of less than 1 mean preferential distribution of Mg and Fe into olivine and the coexisting melt. However, the behavior of the Mg/Fe distribution at high temperatures cannot be directly extrapolated to low temperatures even when amorphous silicate is in metastable equilibrium with olivine, based on thermodynamic consideration of the Mg/Fe distribution (appendix A). In the present experiment, the effective distribution coefficients of Mg/Fe between olivine and the amorphous silicates, K'_D, is 0.4 ± 0.1 during crystallization (Fig. 5.4). Note that olivine is not in equilibrium with amorphous silicate in the early stages of crystallization, and the distribution coefficient is effectively one. However, the effective distribution coefficient almost equals the metastable coefficient (K'_D = 0.4), which can be obtained under olivine-amorphous silicate metastable conditions. The present experimental results show that K_D is less than 1

in non-equilibrium and metastable states under the subsolidus condition. A similar value of K_D at high temperature (> 1100°C) and the temperature in the present experiments (700°C) suggests that effective distribution coefficients K'_D over a wide range of subliquidus temperatures are roughly 0.3-0.4.

Formation of Mg-rich olivine from Fe-bearing amorphous silicates is expected in circumstellar regions. A typical degree of crystallization is about 0.1 in Herbig AeBe and T Tauri stars (van Boekel et al., 2005; Honda et al., 2006), and about 0.05 in AGB stars (Tielens et al., 1998). These low degrees of crystallization correspond to highly Mg-rich olivine composition (Mg# = 0.85 - 0.9) in the present experiments. If some iron exists as a metal phase, the Fe content of amorphous silicates should be less than the starting material, and more Mg-rich olivine is expected. If we assume K'_D is 0.4 and Mg# of an amorphous silicate is 0.8 (0.74 in the present experiment), Mg# of crystallized olivine is higher than 0.9 until the degree of crystallization reaches 0.15. Therefore, we propose that the crystallization of circumstellar silicates is involved in Mg/Fe fractionation, as seen in the experiments.

Stellar wind is commonly assumed to be dust-driven in circumstellar environments of evolved stars (Sedlmayr & Dominik, 1995; Ferrarotti & Gail, 2006). Opacity of dusty materials is an important parameter for the wind driving mechanism. Metallic iron inclusions or Fe-bearing silicates have a high absorption efficiency in the range of near-infrared wavelength, although pure magnesium silicates are almost transparent (Tielens et al., 1998; Dorschner et al., 1995). Moreover, Mg-pure silicates with metallic iron inclusions are more opaque than a mixture of Fe-bearing amorphous silicates and Mg-rich crystalline silicates (Posch, 2005). If iron is absent from dust, stellar wind cannot be driven because of the transparency of Mg-pure silicates. In the case of Mg-pure silicates with metallic iron inclusions, their

absorption efficiency is so high that radiative heating allows only limited amount of dust to survive without evaporation (Woitke, 2006). A mixture of Fe-bearing amorphous silicates and Mg-rich olivine is a promising dust model that is consistent with observations and can drive stellar wind around oxygen-rich evolved stars.

5.4 Conclusions

We show the first experimental evidence that Fe-depleted olivine can be formed by crystallization processes via thermal heating of FeO-bearing amorphous silicates under subsolidus conditions. In the past, there has been an inconsistency in compositions between coexisting crystalline and amorphous phases. Our discovery that the crystallization process is involved in Mg/Fe fractionation can answer the composition paradox of the coexistence of Mg-rich crystalline silicates and Fe-bearing amorphous silicates around stars.

Bibliography

Anders, E., & Grevesse, N. 1989, Geochim. Cosmochim. Acta, 53, 197

Brearley, A., & Jones, R. H. 1989, in Planetary Materials, ed. Papike, J. (The Mineralogical Society of America)

Brown, G. E. 1982 in Orthosilicates, ed. Ribbe, P. (The Mineralogical Society of America)

Crovisier, J. et al. 1997, Science 275, 1904

Dorschner, J., Begemann, B., Henning, Th., Jäger, C., & Mutschke, H. 1995, A&A, 300, 503

Ferrarotti, A. S. & Gail, H. P. 2006, A&A, 447, 553

Honda, M. et al. 2006, ApJ, 646, 1024

Keller, L. P., Hony, S., Bradley, J. P., et al. 2002, Nature, 417, 148

Kemper, F., Vriend, W. J., & Tielens, A. G. G. M. 2004, ApJ, 609, 826

Koike, C., Chihara, H., Tsuchiyama, A., Suto, H., Sogawa, H., & Okuda, H. 2003, A&A, 399, 1101

Molster, F. J. et al. 1999, A&A, 350, 163

Murata, K. et al. 2007, ApJ, 668, 285

Posch, Th. Ph.D. Thesis. (Gedruckt mit Unterstützung der Universität Wien, 2005)

Rietmeijer, F. J. M. 1989, in Planetary Materials, ed. Papike, J. (The Mineralogical Society of America)

Roeder, P. L. & Emslie, R. F. 1970, Contrib. Miner. Petrol., 29, 275

Sedlmayr, E. & Dominik, C. 1995, Space Science Reviews, 73, 211

Tielens, A. G. G. M., Waters, L. B. F. M., Molster, F. J. & Justtanont, K. 1998, Astrophys. Space Sci. 255, 415

van Boekel, R. et al. 2005, A&A, 437, 189

Waelkens, C. et al. 1996, A&A, 315, L245

Waters, L. B. F. M., Molster, F. J., de Jong, T., et al. 1996, A&A, 315, L361

Woitke, P. 2006, A&A, 460, L9

Chapter 6

Summary & Future Prospects

Using amorphous silicate materials synthesized by a sol-gel method, we have carried out laboratory simulations of crystallization process in circumstellar environments of young and evolved stars. By quantitative analyses of IR spectral evolutions during crystallization processes of these silicates, several interesting new results have been obtained. We believe that these results are an important step towards solving the not-yet-understanding mechanisms for formation processes of crystalline silicates around stars.

In chapter 2, pyroxene (enstatite) crystallization was expressed with the Johnson-Mehl-Avrami (JMA) equation with $n = 2.5$, which is consistent with nucleation and diffusion-controlled growth. We evaluated quantitatively the time constant of the crystallization process in the JMA equation, and obtained the activation energy of the enstatite crystallization as 1.12×10^5 K. In chapter 4, olivine (Mg# $\sim$ 0.8 - 1) crystallization was expressed with the JMA equation with $n = 1.5$, which is consistent with diffusion-controlled growth from pre-existing nucleation sites. The activation energy of the olivine crystallization was roughly evaluated as 6×10^4 K.

A low-temperature IR spectroscopy of the sample obtained in chapter 2

was given in chapter 3. There is a discrepancy between the IR feature of enstatite obtained in this experiment and that obtained in the spectroscopic experiments using single crystals. This reflects a discrepancy in stacking disorder of enstatite. We discovered that circumstellar dust emission of enstatite is similar to the IR feature measured in this experiment. This result suggested that circumstellar enstatite has stacking faults and is different from the single crystal. These detailed structures of IR feature may reflect physical and chemical conditions of crystalline silicate formation. In the context of astromineralogy, identification of circumstellar mineral species was in the main focus of interest. Our result will draw attentions to more detailed mineralogy to discuss specific processes in astrophysical environments. More laboratory simulations combined with more detailed spectroscopy at low temperature are needed.

In chapter 5, we showed experimental evidence that Fe-depleted olivine can be formed by crystallization processes via thermal heating of FeO-bearing amorphous silicates. In the past, there has been an inconsistency in compositions between coexisting crystalline and amorphous phases. Our discovery that the crystallization process is involved in Mg/Fe fractionation can answer the composition paradox of the coexistence of Mg-rich crystalline silicates and Fe-bearing amorphous silicates around stars. Pyroxene crystallization from FeO-bearing amorphous silicates should be verified for future study.

The work presented in this thesis poses a serious question: what is nature of typical amorphous silicates in interstellar and circumstellar regions? Chemical compositions of amorphous silicates are important but are still unknown precisely. The Mg/(Mg+Fe) ratio of amorphous silicates is closely connected to that of crystalline silicates (> 0.9). We proposed in chapter 5 that the Mg/(Mg+Fe) ratio of an amorphous silicate is restricted as

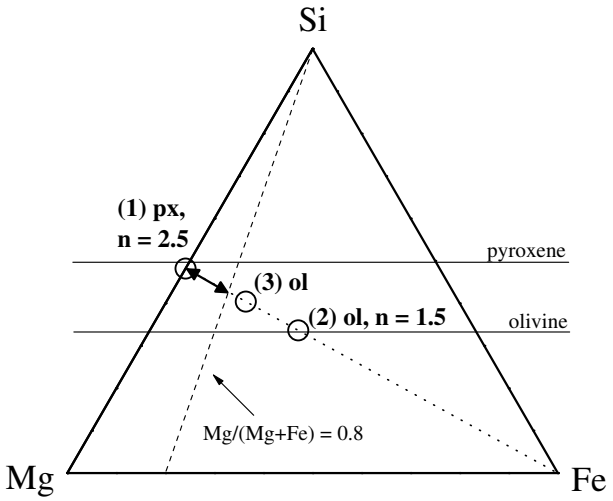

Figure 6.1: Ternary diagram of atomic proportions of starting materials of crystallization experiments in this thesis. The arrow indicates constraint of a composition of amorphous silicates by K'_D of 0.4.

higher than 0.8 using $K'_D = 0.4$ (indicated by the arrow in Fig. 6.1). The (Mg+Fe)/Si ratio of amorphous silicates is another important parameter for its mineralogical evolution. In this thesis, pyroxene was crystallized from the amorphous silicate with the (Mg+Fe)/Si ratio of 1.07 and olivine was crystallized from those of 1.46 and 1.97. Furthermore, our experiments suggested that an existence of nucleation "seeds" should affect the crystallization kinetics and the activation energy (chapter 4).

A comparison of pyroxene crystallization with olivine one will give important information about the (Mg+Fe)/Si ratio of amorphous silicates because the crystallized mineral phases are limited by the (Mg+Fe)/Si ratio. Although we do not have enough data to argue with both the chemical compositions and the existence of seeds, we compared their crystallization for preliminary investigation using data obtained in this thesis. In general, it is difficult

to synthesize an SiO_2-poor amorphous silicate because of its rapid crystallization. This suggests that an amorphous silicate with a high (Mg+Fe)/Si ratio tends to contain nucleation sites before the crystallization process starts. In fact, the present experimental results on three different (Mg+Fe)/Si ratios are consistent with this tendency. Thus, we assumed here in general that an amorphous silicate with a high (Mg+Fe)/Si ratio (∼1.5 - 2, hereafter called as SiO_2-poor amorphous silicate) crystallizes to olivine without nucleation (n = 1.5), and an amorphous silicate with a low (Mg+Fe)/Si ratio (∼1, hereafter called as SiO_2-rich amorphous silicate) crystallizes to pyroxene by nucleation and growth (n = 2.5). The experimental parameters obtained in chapter 4 ((2) in Fig. 6.1) and chapter 2 ((1) in Fig. 6.1) were used tentatively for the former and latter crystallization processes, respectively. Note that the value of the Arrhenius parameters (activation energy and frequency factor) of olivine crystallization were roughly estimated in chapter 4. In addition, the (2) composition in Fig. 6.1 is not consistent with observation of Mg-rich circumstellar olivine when K'_D is assumed as 0.4. We used these experimental data because of lack of other appropriate data. The Arrhenius parameters of pyroxene crystallization are estimated more precisely (chapter 2). However, a problem of starting amorphous silicate remains: the enstatite nucleation required the change in the amorphous structure in this experiment, while we cannot determine whether a circumstellar amorphous silicate needs its structure change accompanied with crystallization or not.

Figure 6.2 shows time required for olivine and pyroxene crystallization with degrees of crystallization of 0.05, 0.5 and 0.99 as a function of temperature. The dots also indicate time required for crystallization of olivine with degrees of crystallization of 0.05, 0.5 and 0.99, that were obtained in chapter 5 ((3) in Fig. 6.1). These dots were plotted close to olivine crystallization

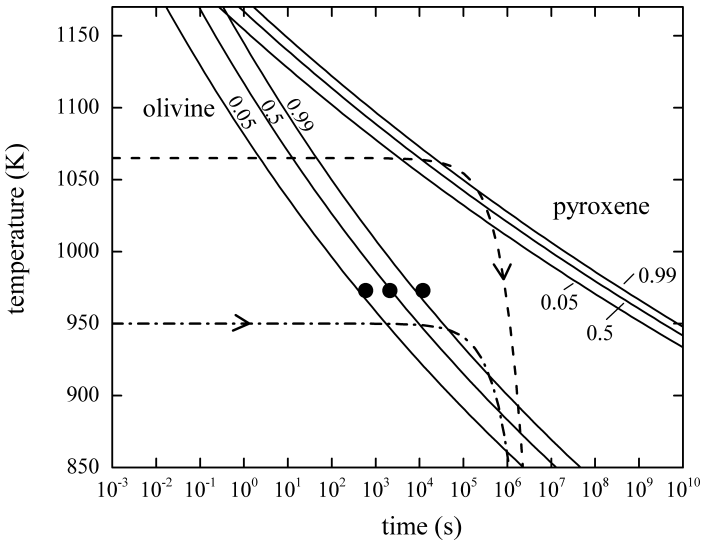

Figure 6.2: TTT (time - temperature - transformation) diagram for olivine and pyroxene crystallization from SiO_2-poor and -rich amorphous silicates, respectively. The solid lines indicate time required for crystallization with degrees of crystallization of 0.05, 0.5 and 0.99 using data obtained in chapter 2 for pyroxene and chapter 4 for olivine. The dots also indicate time required for crystallization of olivine with degrees of crystallization of 0.05, 0.5 and 0.99, that were obtained in chapter 5. The arrow lines indicate cooling processes of silicate dust in stellar winds of evolved stars (eq. 2.9 with $\tau_{\rm cool}$ of 10^7 s).

lines in Fig. 6.2. This implies that olivine crystallization lines estimated using data of the (2) composition (Fig. 6.1) is not so far from precise estimation using not-obtained experimental data of amorphous silicates whose compositions are indicated by the arrow in Fig. 6.1. Time and temperature ranges for partial crystallization of olivine are wider than those of pyroxene due to the smaller value of n for olivine. Although quantitative discussion cannot be made in detail, at a constant temperature below 1150 K, time for crys-

tallization of pyroxene is always longer than that of olivine. The arrow lines in Fig. 6.2 show cooling processes of silicate dust condensed in stellar winds of evolved stars, which were considered in a same manner in chapter 2. The amorphous silicates are thought to condense from gas phase in winds. The (Mg+Fe)/Si ratio of those is expected as approximately constant in individual stars, although it changes through evolutionary sequences. Condensation temperatures of SiO_2-poor and -rich amorphous silicates around evolved stars are not clear. Here we assume that both of them condense at same temperature for both SiO_2-poor and -rich compositions. When condensation temperature is high (dashed line), both olivine and pyroxene are crystallized from SiO_2-poor and -rich amorphous silicates, respectively. In a case of low condensation temperature (dot-dashed line), only olivine is crystallized from the SiO_2-poor amorphous silicate, while the SiO_2-rich silicate remains amorphous. Astronomical observation suggested that pyroxene is more abundant than olivine in circumstellar regions of evolved stars (Molster et al., 2002). Therefore, it is implied that amorphous precursors of pyroxene are condensed more abundant than that of olivine, or crystallized olivine reacts with SiO gas and transforms to pyroxene (Gail, 2002).

The arrow line in Fig. 6.3 shows schematic dust temperature history when dust moves toward hot inner region of protoplanetary disks. The (Mg+Fe)/Si ratio of amorphous silicates in disks is considered to be variable, since amorphous silicates are accreted from the surrounding clouds. It is shown that olivine is crystallized first, and pyroxene crystallization occurs in the inner hotter region of disks, if dust is a mixture of SiO_2-poor and -rich amorphous silicates. Thus, both pyroxene and olivine are expected to exist in the inner region of disk, while almost only olivine is present as the crystalline phase in the outer region.

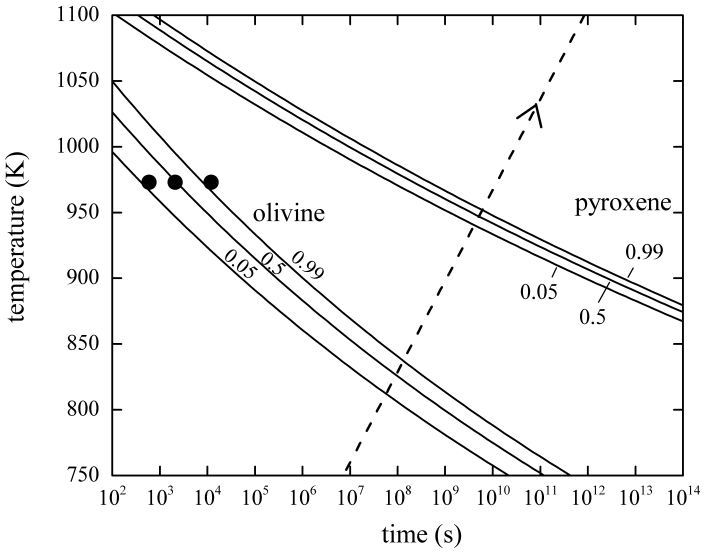

Figure 6.3: TTT (time - temperature - transformation) diagram for olivine and pyroxene crystallization from SiO_2-poor and -rich amorphous silicates, respectively. The solid lines indicate time required for crystallization with degrees of crystallization of 0.05, 0.5 and 0.99 using data obtained in chapter 2 for pyroxene and chapter 4 for olivine. The dots also indicate time required for crystallization of olivine with degrees of crystallization of 0.05, 0.5 and 0.99, that were obtained in chapter 5. The arrow line is schematic dust temperature history when dust moves inwards in protoplanetary disks.

In order to verify this tentative view of crystallization nature of silicate dust in circumstellar environments, more experiments are needed. Additional crystallization experiments of amorphous silicates with widely changed compositions will give important information, such as crystallized mineral species and activation energy, for understanding of compositions of the precursor material and its evolution history under circumstellar conditions. Especially, amorphous silicates with a higher Mg/(Mg+Fe) ratio are crucial because compositions of crystallized silicates are constrained by an Mg/Fe distribu-

tion during crystallization. A structure of amorphous silicates is also important, although it is much difficult to control. Synthesis of amorphous silicates with different methods (e.g., vapor condensation, sol-gel reaction, and melt-quenching) combined with careful analyses of amorphous silicates (e.g., transmission microscopy for short-range structure; IR absorption and X-ray photoelectron spectroscopy and X-ray absorption fine structure for middle-range structure; X-ray and neutron diffraction for long-range structure) will lead to a more precise understanding of the precursor material and the formation condition of circumstellar crystalline silicates.

Bibliography

Gail, H.-P. 2002, in Astromineralogy, ed. Henning, Th. (Lecture Notes in Physics 609; New York: Springer), 55

Molster, F. J., Waters, L. B. F. M., Tielens, A. G. G. M., Koike, C., & Chihara, H. 2002, A&A 382, 241

Appendix A

Thermodynamic Consideration of Mg/Fe Distribution between Olivine and Amorphous Silicate

A phase diagram of the fayalite (Fe_2SiO_4) - forsterite (Mg_2SiO_4) system at one atmosphere pressure was obtained experimentally by Bowen & Schairer (1935). This phase diagram shows that Mg and Fe are preferentially distributed into olivine crystal and liquid, respectively, or the Mg-Fe distribution coefficient is less than unity ($K_D = (\mathrm{Mg/Fe})_{liquid}$ / $(\mathrm{Mg/Fe})_{olivine}$ <1). Figure A.1(a) shows a schematic phase diagram of the same system. The chemical compositions of olivine solid solution, b, and liquid, a, in equilibrium at a high temperature, $T = T_1$, can be determined by a common tangent between the $G - X_{Fo}$ curves of olivine and liquid at G_b and G_a, respectively in Fig. A.1(b) (G denotes Gibbs free energy, and X_{Fo} the mole fraction of the forsterite component, which is equal to Mg#).

When a liquid of composition, c, is supercooled (or supersaturated) at T_1, the compositional range of olivine crystallized from the liquid can be

restricted by considering the decrease of the total free energy caused by an infinitesimally small degree of crystallization (Baker & Cahn, 1971). The possible range (from d to e in Figure A.1(b)) can be determined by the intersections of the tangent to the $G - X_{Fo}$ curve of liquid from G_c at the $G - X_{Fo}$ curve of olivine, G_d and G_e. The exact olivine composition is dependent on the specific crystallization processes, such as the kinetics at the growing solid-liquid interface and the elemental diffusion, mainly in solids, and cannot be determined uniquely by thermodynamics. The effective distribution coefficient, K'_D, in crystallization cannot be predicted theoretically without preforming experiments (e.g., Tsuchiyama et al., 1981), although some theoretical studies have been conducted (e.g., Kitamura & Matsumoto, 2004). However, we can predict $K'_D < 1$ based on the thermodynamic considerations.

At a low temperature below the solidus, $T = T_2$, liquid (or amorphous silicate) cannot be in equilibrium with olivine even metastably in this binary system (Fig. A.1(c)). A tangent from the amorphous silicate, c, ($G'_f - G'_c - G'_g$) is generally located above G of olivine of any compositions. This shows that the composition of olivine crystallized from an amorphous silicate cannot be restricted at low temperatures, and we do not know whether $K'_D < 1$ or > 1 without experimental study.

The system is not binary in either the present experiments or natural processes for cosmic dust. Figure A.2(a) shows a schematic (pseudo-)ternary phase diagram in the X-fayalite-forsterite system, where X is SiO_2 in the experiments (the phase diagram in this system was obtained by Bowen & Schairer (1935)), and SiO_2 and other components such as Al_2O_3, CaO, and Cr_2O_3 (e.g., CI chondritic composition). In this phase diagram, curve A-D-B corresponds to the reaction (or cotectic) line, and the primary field of

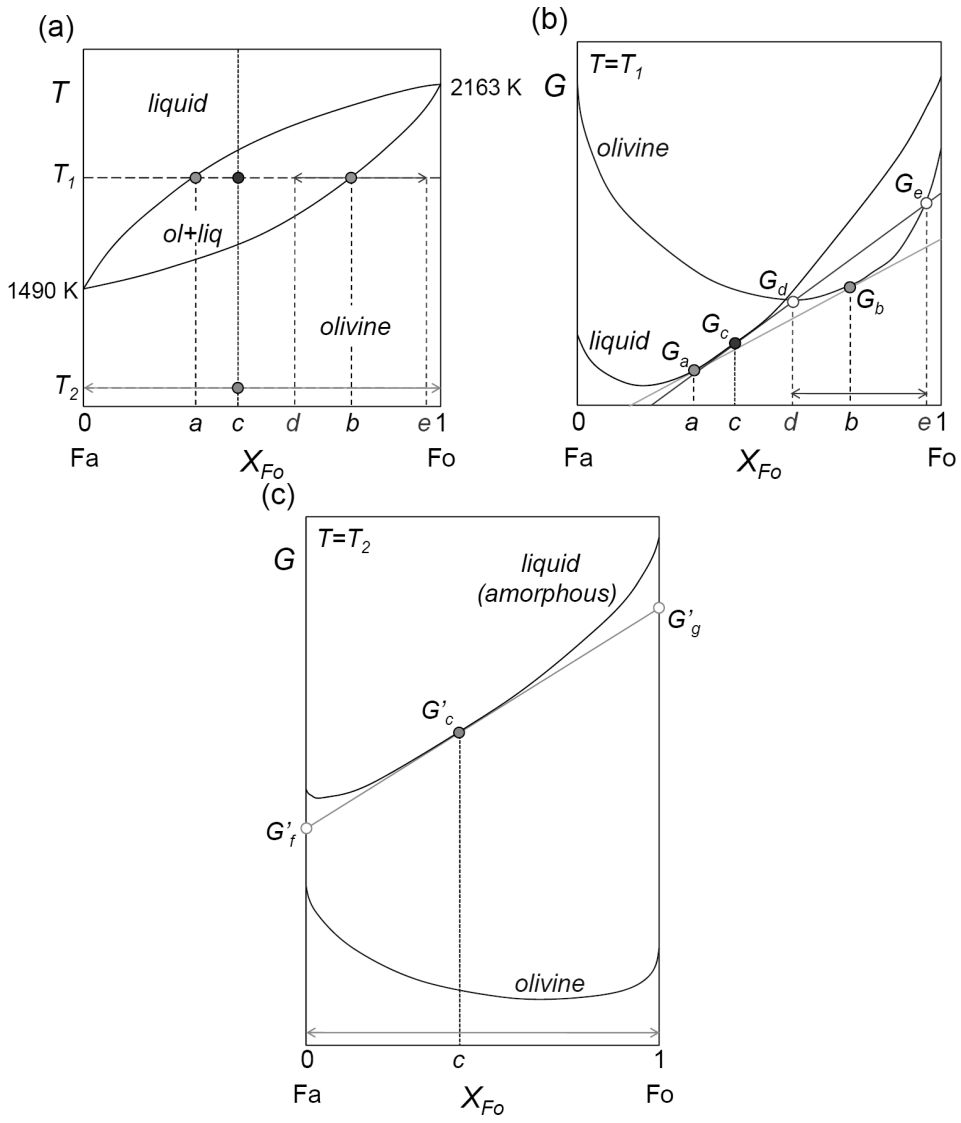

Figure A.1: Schematic phase diagram of the binary system of fayalite (Fa) - forsterite (Fo) and G (Gibbs free energy) - X_{Fo} (mole fraction of the forsterite component). (a)Binary phase diagram. T is temperature. (b) G - X_{Fo} diagram at $T = T_1$. The olivine composition from supersaturated liquid, c, is limited from d to e. (c) G-X_{Fo} diagram at $T = T_2$. The olivine composition from supersaturated liquid, c, is limited from fayalite to forsterite. See the text for a detailed discussion.

olivine is in area Fa-Fo-B-D-A. Curve C-a-D is an olivine isotherm at a high temperature of T_3. Note that olivine and liquid (or amorphous silicate) can be in metastable equilibrium at low temperature, even below the solidus. Curve E-d-F denotes a metastable olivine isotherm at a low temperature of T_4. Olivine compositions in (metastable) equilibrium with the melt (or amorphous silicate), a and d, are shown by the connecting line (a-b at T_3 and d-e at T_4).

Figure A.2(b) shows a G-composition diagram in the (pseudo-)ternary system at $T = T_3$. The G-composition surface corresponds to the liquid. The equilibrium between olivine, b, and liquid, a, is uniquely determined by a common tangent between G_b and G_a (G_a is on the liquid G-composition surface). In this figure, Mg and Fe are distributed into olivine and liquid, respectively, and $K_D < 1$ as indicated by previous experimental data in magmatic systems (Roeder & Emslie, 1970). However, there is no guarantee in general that $K_D < 1$. In the case of crystallization from a supercooled liquid, c, the olivine compositional range, from g to h, can be constrained by drawing a tangential plane from G_a (G_g and G_h are the intersections at the olivine G-X_{Fo} curve) as an analogy of the binary system (G_d and G_e in Figure A.1(b)). In this figure, $K'_D < 1$ too; however, this is not a straightforward conclusion even if $K_D < 1$.

At a low temperature of $T = T_4$, the metastable equilibrium is determined by a common tangent between G'_d and G'_e (Fig. A.2(c)). The metastable Mg-Fe distribution in this figure is drawn to be consistent with the present experimental results at a degree of crystallization of about 0.8 ($K_D \sim 0.4$, Fig. 5.4), although we cannot constrain the distribution, in general, based on a G-composition diagram. In the case of olivine crystallization from a supercooled amorphous silicate, c, as in the case of crystallization from the

starting material in the experiments, line G'_g-G'_h, which is obtained by the intersection of a tangential plane of liquid G-composition surface from G'_e on the G-X_{Fo} plane, is located above the olivine G-X_{Fo} curve. Accordingly, we cannot constrain the Mg-Fe distribution; i.e., we cannot determine whether $K'_D < 1$ or > 1. The present experiments show that $K'_D \sim 0.4$ (also $K_D \sim 0.4$) along the amorphous silicate trend by crystallization at 700°C.

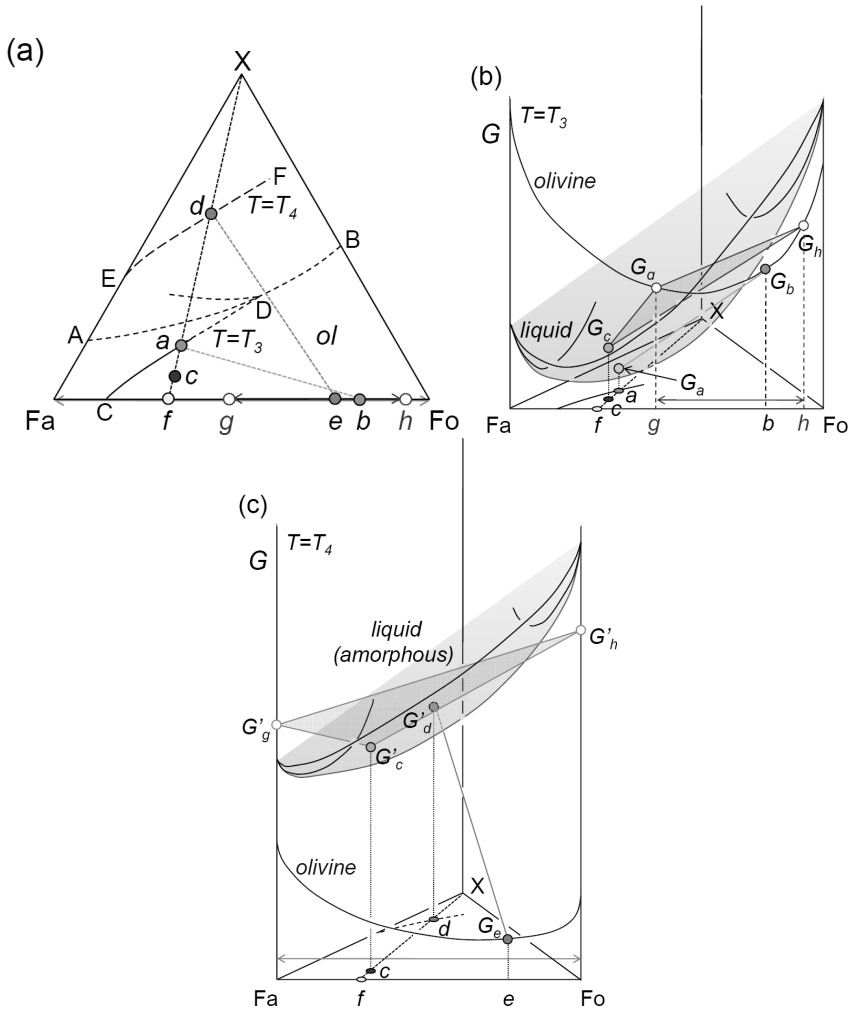

Figure A.2: Schematic phase diagram of a (pseudo-)ternary system of X (SiO_2 or other components) - fayalite (Fa) - forsterite (Fo) and G (Gibbs free energy). (a)(Pseudo-)ternary phase diagram showing the primary field of olivine. Curve A-D-B corresponds to the reaction (or cotectic) line, curve C-a-D is an olivine isotherm at T_3, and curve E-d-F is a metastable olivine isotherm at T_4. (b) G-composition diagram at $T = T_3$. The curved surface of G for liquid is shown as a hatched area. The olivine composition from supersaturated liquid, c, is limited from g to h. (c) G-X_{Fo} diagram at $T = T_4$. The olivine composition from supersaturated liquid, c, is limited from fayalite to forsterite. See the text for a detailed discussion.

Bibliography

Baker, J. C., & Cahn, J. W. 1989, in Solidification (American Society for Metals, Metals Park, Ohio)

Bowen, N. L. & Schairer, J. F. 1935, Am. J. Sci., 29, 151

Kitamura, M. & Matsumoto, N. 2004, J. Cryst. Growth, 260, 243

Roeder, P. L. & Emslie, R. F. 1970, Contrib. Miner. Petrol., 29, 275

Tsuchiyama, A, Kitamura, M., & Sunagawa, I. 1981, J. Cryst. Growth, 55, 510

Appendix B

List of Publications

B.1 Refereed Paper

1. Murata, K., & Katsura, M. 2005 "Electron Spin Resonance Study of Gamma-Ray-Irradiated Prince Rupert's Drops for Confirmation of Stress Effects on Paramagnetic Defect Formation in Borosilicate Glass" Japanese Journal of Applied Physics, 44, 5A, 3172

2. Murata, K., Chihara, H., Tsuchiyama, A., Koike, C., Takakura, T., Noguchi, T., Nakamura, T. 2007 "Crystallization Experiments on Amorphous Silicates with Chondritic Composition: Quantitative Formulation of the Crystallization" The Astrophysical Journal, 668, 285

3. Murata, K., Chihara, H., Tsuchiyama, A., Koike, C., Takakura, T., Noguchi, T., Nakamura, T. 2007 "Crystalline Silicate Formation in Protoplanetary Disks: Heating Experiments of Amorphous Silicate" Planetary People, 16, 2, 119 (in Japanese)

4. Murata, K., Takakura, T., Chihara, H., Koike, C., Tsuchiyama, A. 2009 "Mg/Fe Fractionation in Circumstellar Silicate Dust Involved in

Crystallization" The Astrophysical Journal, 696, 1612

5. Murata, K., Chihara, H., Koike, C., Takakura, T., Imai, Y., Tsuchiyama, A. 2009 "Crystallization Experiments on Amorphous Magnesium Silicate. I. Estimation of the Activation Energy of Enstatite Crystallization" The Astrophysical Journal, 697, 836

B.2 Conference Proceedings

1. Murata, K., Chihara, H., Koike, C., Takakura, T., Tsuchiyama, A. 2005 "Crystallization Experiments of Amorphous Silicate with the CI Chondritic Composition" Grain Formation Workshop 2005 (Vol. XXV), 127

2. Murata, K., Takakura, T., Chihara, H., Koike, C., Tsuchiyama, A. 2007 "Crystallization Experiments of Amorphous Silicates with the CI Chondritic Composition" Astronomical Society of the Pacific Conference Series "Why Galaxies Care About AGB Stars: Their Importance as Actors and Probes", 378, 323

B.3 Thesis

1. Murata, K. "内部応力による放射線誘起欠陥の生成効率への影響－ＥＳＲ及びルミネッセンス年代測定に向けて－" Bachelor Thesis, Department of Physics, Undergraduate School of Science, Osaka University, Japan, Mar. 2004

2. Murata, K. "Crystallization Experiments of Amorphous Silicate with the CI Chondritic Chemical Composition Produced by the Sol-Gel

Method", Master Thesis, Department of Earth and Space Science, Graduate School of Science, Osaka University, Japan, Mar. 2006

Appendix C

List of Presentations

C.1 International Conference

C.1.1 Oral Presentation

1. Murata, K., Takakura, T., Chihara, H., Koike, C., Tsuchiyama, A. "Crystallization Experiment of Amorphous Silicates with the CI Chondritic Composition" 19th General Meeting of the International Mineralogical Association, O23-10, International Conference Center Kobe, Japan, July 26, 2006

C.1.2 Poster Presentation

1. Murata, K., Takakura, T., Chihara, H., Koike, C., Tsuchiyama, A. "Crystallization Experiments of Amorphous Silicates with the CI Chondritic Composition" Why Galaxies Care about AGB Stars: Their Importance as Actors and Probes, P40, University of Vienna, Austria, Aug. 6-11, 2006

2. Murata, K., Chihara, H., Koike, C., Imai, Y., Tsuchiyama, A. "Crystal-

lization Experiments on Amorphous Magnesium Silicates" Asia Oceania Geosciences Society 2008 5th Annual General Meeting, PS03-D4-PM2-P-051, PS03-A039, Busan, June 19, 2008

3. Imai, Y., Koike, C., Chihara, H., Murata, K., Suto, H., Aoki, T., Tsuchiyama, A. "Shape and Lattice Distortion Effects on Infrared Spectra of Olivine Particles" Asia Oceania Geosciences Society 2008 5th Annual General Meeting, PS03-D4-PM2-P-050, PS03-A029, Busan, June 19, 2008

4. Noguchi, R., Murata, K., Tsuchiyama, A., Isobe, H., Chihara, H., Nakamura, T., Noguchi, T. "Hydrothermal Experiments of Synthetic Amorphous Silicates with CI Chondritic Composition in the Systems with and without FeO" 71st Annual Meeting of the Meteoritical Society, Shimane, July 29, 2008

5. Murata, K., Chihara, H., Koike, C., Imai, Y., Tsuchiyama, A. "Experimental Study on Crystallization of Amorphous Magnesium Silicates" Cosmic Dust - Near & Far 2008, VII18, Heidelberg, Sept. 8-12, 2008

C.2 Domestic Conference

C.2.1 Oral Presentation

1. 村田敬介, 谷篤史, 平井誠, 池谷元伺 "A Basic Study on Effects of Internal Stress on Formation Efficiency of Radiation-Induced Center for ESR and Luminescence Dating" 地球惑星科学関連学会 2004 年合同大会, J026-001, 幕張メッセ, May 2004

2. 桂誠, 村田敬介 "Stability of Borosilicate Glass under Gamma-Ray Ir-

radiation" 日本原子力学会 2004 年秋の大会, G40, 京都大学, Sept. 16, 2004

3. 村田敬介, 茅原弘毅, 小池千代枝, 谷篤史, 土`山明, 本田充彦 "Infrared Spectroscopic Study of Crystallization of Chondritic Amorphous Silicates" 地球惑星科学関連学会 2005 年合同大会, P058-009, 幕張メッセ, May 2005

4. 村田敬介, 茅原弘毅, 小池千代枝, 谷篤史, 土`山明, 本田充彦 "Crystallization of Amorphous Silicate with Chondritic Composition" 惑星科学会 2005 年秋季講演会, B13-2, 会津大学, Sept. 20, 2005

5. 村田敬介, 茅原弘毅, 小池千代枝, 土`山明, 本田充彦 "コンドライト組成を持つアモルファスシリケイトの結晶化に伴う赤外吸収スペクトルの変化" 日本天文学会 2005 年秋季年会, Q40a, 札幌コンベンションセンター, Oct. 6, 2005

6. 小池千代枝, 周藤浩士, 直井隆浩, 茅原弘毅, 村田敬介, 土`山明, 奥田治之 "オリヴィン微粒子の中間赤外から遠赤外スペクトルの形状効果および温度効果 III" 日本天文学会 2005 年秋季年会, Q39a, 札幌コンベンションセンター, Oct. 6, 2005

7. 高倉崇, 村田敬介, 茅原弘毅, 小池千代枝, 土`山明 "Crystallization Process of Amorphous Silicate with the Chondritic Composition: Effects of Oxidation-Reduction Condition of Iron" 日本地球惑星科学連合 2006 年大会, P155-016, 幕張メッセ, May 14, 2006

8. 村田敬介, 高倉崇, 茅原弘毅, 小池千代枝, 土`山明 "オリビン 11.2 μm ピークは正しい Mg/Fe 比を示すか?" 日本天文学会 2006 年秋季年会, P44a, 九州国際大学, Sept. 20, 2006

9. 直井隆浩, 周藤浩士, 小池千代枝, 茅原弘毅, 寒川尚人, 村田敬介, 森脇太郎 “エンスタタイト結晶の低温での赤外線分光測定” 日本天文学会 2007 年春季年会, P29a, 東海大学, Mar. 29, 2007

10. 村田敬介, 茅原弘毅, 高倉崇, 小池千代枝, 土`山明 “Effect of Anisotropic Crystallization on the IR Absorption Spectra of Silicates” 日本地球惑星科学連合 2007 年大会, P137-018, 幕張メッセ, May 24, 2007

11. 野口遼, 村田敬介, 土`山明, 中村智樹, 茅原弘毅, 野口高明 “Hydrothermal Alteration Experiments of Amorphous Silicates: Comparison of Experimental Products with Minerals of Carbonaceous Chondrites” 日本惑星科学会 2007 年秋季講演会，325，高知大学，Sept. 27, 2007

12. 高倉崇, 村田敬介, 茅原弘毅, 小池千代枝, 土`山明 “非晶質シリケイトの加熱結晶化に伴う非晶質-結晶質間の Fe-Mg 分配” 日本天文学会 2008 年春季年会, P34a, 国立オリンピック記念青少年総合センター, Mar. 26, 2008

13. 今井悠太, 小池千代枝, 茅原弘毅, 村田敬介, 土`山明 “オリビン微粒子の赤外吸収スペクトルにおける粒子形状及び格子歪みの影響” 日本天文学会 2008 年春季年会, P35a, 国立オリンピック記念青少年総合センター, Mar. 26, 2008

14. 村田敬介, 茅原弘毅, 小池千代枝, 今井悠太, 土`山明, 高倉崇 “Crystallization Experiments on Amorphous Magnesium Silicates” 日本地球惑星科学連合 2008 年大会, P137-019, 幕張メッセ, May 30, 2008

15. 高倉崇, 村田敬介, 茅原弘毅, 小池千代枝, 土`山明 “Elemental Distribution between Crystal and Amorphous Phases in Crystallization Process of Silicate” 日本地球惑星科学連合 2008 年大会, P137-021, 幕張メッセ, May 30, 2008

16. 今井悠太, 小池千代枝, 茅原弘毅, 村田敬介, 土`山明, 野口高明 “Shape Effects on Infrared Spectra of Forsterite Particles” 日本惑星科学会 2008 年秋季講演会，319，九州大学，Nov. 3, 2008

C.2.2 Poster Presentation

1. 村田敬介, 茅原弘毅, 小池千代枝, 谷篤史, 土`山明, 本田充彦 “Crystallization of Amorphous Silicate with Chondritic Composition” 惑星科学会 2005 年秋季講演会, P14-57, 会津大学, Sept. 20, 2005

2. 村田敬介, 高倉崇, 茅原弘毅, 小池千代枝, 土`山明 “Quantitative Parameterization and Formulation of Crystallization Process of Amorphous Silicates” 日本地球惑星科学連合 2006 年大会, P155-020, 幕張メッセ, May 14, 2006

3. 野口遼, 村田敬介, 土`山明, 茅原弘毅, 野口高明, 中村智樹 “Hydrothermal Alteration Experiments of Amorphous Silicates” 日本地球惑星科学連合 2007 年大会, P137-P009, 幕張メッセ, May 23, 2007

4. 村田敬介, 茅原弘毅, 高倉崇, 小池千代枝, 土`山明 “Effect of Anisotropic Crystallization on Infrared Absorption Spectra of Crystalline Silicates” 日本惑星科学会 2007 年秋季講演会，P04，高知大学，Sept. 25-26, 2007

5. 高倉崇, 村田敬介, 茅原弘毅, 小池千代枝, 土`山明 “Crystallization Process of Amorphous Silicate with the Solar Composition: Distribution of Fe/Mg between the Olivine and the Amorphous Silicate” 日本惑星科学会 2007 年秋季講演会，P41，高知大学，Sept. 25-26, 2007

6. 今井悠太, 小池千代枝, 茅原弘毅, 村田敬介, 土`山明 “Production of Sub-Micron Silicate Particles by Ball Mill Crushing and Their IR Spec-

troscopy" 日本惑星科学会 2007 年秋季講演会，P45，高知大学，Sept. 25-26, 2007

7. 野口遼, 村田敬介, 土`山明, 磯部博志, 中村智樹, 野口高明, 茅原弘毅 "Hydrothermal Alteration Experiments of Synthetic Amorphous Silicates with CI Chondritic Composition: Systems with and without FeO" 日本地球惑星科学連合 2008 年大会, P137-P002, 幕張メッセ, May 29, 2008

8. 今井悠太, 土`山明, 小池千代枝, 茅原弘毅, 村田敬介 "Synthesis of Amorphous Silicate Nano-Particles as Analogue of Interstellar Dust" 日本地球惑星科学連合 2008 年大会, P137-P003, 幕張メッセ, May 29, 2008

9. 村田敬介, 茅原弘毅, 小池千代枝, 今井悠太, 土`山明 "Far-Infrared Spectroscopic Behavior of Enstatite Crystallized from Amorphous Silicate" 日本惑星科学会 2008 年秋季講演会，P103，九州大学，Nov. 1, 2008

10. 野口遼, 村田敬介, 土`山明 "Hydrothermal Alteration Experiments of Synthetic Amorphous Silicates: Effect of Chemical Composition of Amorphous Silicates on Its Aqueous Alteration Process" 日本惑星科学会 2008 年秋季講演会，P120，九州大学，Nov. 1, 2008